

## Galvanic replacement reactions of Ga and In with Cu for the synthesis of bimetallic nanoparticles

Présentée le 26 août 2022

Faculté des sciences de base  
Laboratoire de nanochimie pour l'énergie  
Programme doctoral en chimie et génie chimique

pour l'obtention du grade de Docteur ès Sciences

par

**Laia CASTILLA AMORÓS**

Acceptée sur proposition du jury

Prof. S. Gerber, présidente du jury  
Prof. R. Buonsanti, directrice de thèse  
Prof. M. Yarema, rapporteur  
Prof. J. Millstone, rapporteuse  
Prof. K. Sivula, rapporteur

# Acknowledgements

The involvement that a PhD requires goes beyond academical. I would like to acknowledge every being and every experience that contributed to the journey of personal development and self-discovering that occurred during these last four years of my life. Both joy and despair were crucial to become the person that today writes these lines. Thank you.

First of all, I would like to express my deepest and most sincere gratitude to Prof. Raffaella Buonsanti. Thank you for your trust and support throughout these years. Thank you for the opportunity of belonging to this beautiful project that is LNCE, you took me in four and a half years ago and opened the door to a new life. Under your supervision, you pushed me to learn and to grow, to think beyond the apparent possibilities and to become a better scientist. You were always there throughout this rollercoaster, encouraging me to improve with both soft and tough love. Everything I learned from you will stay with me forever, you will always be a source of inspiration. And for all of this, I am eternally grateful. *Grazie di cuore.*

I want to extend my thanks to the jury members: Prof. Maksym Yarema, Prof. Jill Millstone, Prof. Kevin Sivula and Prof. Sandrine Gerber. Thank you for dedicating your time to read my thesis and for the interesting and valuable discussion that followed.

I now want to thank every past and present member of LNCE for filling this journey with beautiful experiences and friendships. Most friendships were circumstantial, but many will last a lifetime. In any case, you all participated in your own special way to this adventure. To start with, I would like to thank the initial group of people that took me in when I first came for my Bachelor Thesis. Thank you for accommodating me and for making me feel welcomed, you all participated in my decision to stay here. Thank you, Dr. Anna Loiudice, the backbone of this lab. Not only is your presence and work essential for all of us but you are one of the most patient and hardworking people I know. Thank you for your willingness to help, for your kindness and your support. I am sure you will keep inspiring PhDs students throughout the years. I cannot but wish you the best of lucks. Next, I want to thank both Dr. Michal Strach and Dr. Chethana Gadiyar. You were the first two people I worked with and I could not have been luckier. Your support and trust made me feel capable of anything and learning from you was a true blessing. I want to specially thank my dearest friends Dr. Valeria Mantella and Dr.

Seyedeh Behnaz Varandili. Two of the sweetest and most beautiful people I am lucky to know. Thank you for all you taught me, both academically and personally, and for all you inspired me. You are the two big sisters I never had and I am extremely grateful to have found you. I am looking forward to see what life keeps teaching us and to see how far we go. I love you deeply. Thank you, really.

Thank you Dr. Pranit Iyengar for your nuggets of wisdom and your inspiring attitude. Thank you, Dr. Yannick Guntern, for your kindness and great attitude towards life, you are the founder of a great hymn. Thank you Dr. Seryio Saris for your kindness and for welcoming us in your lovely city. Thank you, Dr. Jan Vavra, for your friendliness and knowledge. I want to specially thank Dr. James Pankhurst, another friendly face that will stay with me. You have been both a great teacher and a great friend. Thank you for every laugh and every silly moment and every deep conversation we have had. My favourite *Dungeon Buddy*. I want to extend my acknowledgements to Dr. Gianluca de Gregorio, Dr. Jianfeng Huang, Dr. Mariateresa Scarongella and Jérémie Bérard. Thank you all for enriching this experience.

Regarding those who were welcomed by me, my deepest love and appreciation goes to Tzu-Chin Chang Chien, my gorgeous Jasmine, and to Ona Segura Lecina and Petru Albertini. Jasmine, you started as my student and you have become my twin soul, my dear friend. I am extremely proud of you; you are truly inspiring and I am looking forward to see what life teaches us next. I love you. To Ona and Petru, you have illuminated my PhD since you came. Thank you for everything, this path would have been much harder without you. I hope I will not have to miss you for long after I am done, my heart will stay in Sion with you both *amics*. Thanks to my desk and Ga partner, Valery Okatenko, you are one of the kindest and more knowledgeable persons I know. Always willing to help others, I wish you all the best life has to offer. Thanks to my other Ga ex-partner, Anastasia Blokhina, you kind soul, I know how far you can get. I am very grateful to Dr. Dragos Stoian and Dr. Min Wang, both your help and your friendliness, always encouraging me, you made this PhD easier to handle. Thank you also to Cedric Koolen, I always enjoy our conversations and get inspired by how driven of a person you are. It was also a great pleasure to work alongside Dr. Kevin Rossi, Dr. Alexander Chen, Dr. Philippe Green, Ludovic Zaza, Kimoon Lee and Andrea Rossi. Thank you all for your help and for every moment we shared.

What could we all do without your help, Laure Dayer? Thank you for your kindness and for all the excellent work you do. LNCE works thanks to you. My special thanks go to our EPFL collaborators, Dr. Emad Oveisi and Dr. Pascal Schouwink. Thank you for all your help during these last four years, as teachers and scientists, and especially during my last project. You made this ending much smoother. Thank you also to Dr. Mounir Mensi and Dr. Natalia Gasilova, for your knowledge and help. I would like to thank also every member of the EPFL Valais staff, everyone in the *Magasin*, the cleaning and the maintenance staff, the mechanical and electronical workshops, as well as in the direction. You are all important, you make all this possible and you made my stay here much more friendly with your kind help and smiles. Thank you for taking care of this international community and for making us feel at home. I would also like to thank every other friend I made while at EPFL, Mehrdad Asgari, Alina Kampouri, Mish Ebrahim, Anita Justin, Vikram Karve and Seyed Mohamad Moosavi. Thank you all for every conversation and every shared moment. Special thanks to my lovely Marketa Suvova. I am so lucky and grateful to have you in my life. Thanks for your love, support and teachings. Thank you for every walk, every conversation. You are truly an inspiring woman. I love you deeply my friend.

*Mon cher Colas.* Thank you for all your love, for taking care of me, thank you for seeing me as I am and for loving that person. I really am blessed to have you in my life, to have found you in this moment of great learning, as both a teacher and a fellow student. I am looking forward to our future together and to making true everything we dream of and more. I love you.

Finally, my greatest thank you goes to my family. *Muchas gracias.* Thank you for always supporting me, for always believing in me and for giving me the freedom to flow as I felt. Thank you for always being there when I needed you Mireia, *mami y papi*. Thank you to my *iaia*, for being my second mom, and to my *iaio*, whom I miss every day, all this is for you. Thank you to every effort and sacrifice everyone before me did so I could be here. Thank you to all my aunts, uncles and cousins, both in Spain and in Greece. Thank you for all the love you have always given and continue to give me. I am really blessed for the family I have. Special thanks go to my hairier family members, past and present. My siblings Hannah and Pongo and my daughter Kleio, ¡*Guau!*



# Abstract

The need for efficient and selective catalysts, capable of driving important conversions to build a more sustainable society, encourages the development of synthetic approaches towards new nanomaterials. Cu-based bimetallic nanoparticles (NPs) promise to fulfill this gap by selectively producing energy-dense products via CO<sub>2</sub> electroreduction (CO<sub>2</sub>RR). However, as small variations in its composition and configuration can enormously affect the catalyst performance, the vast diversity of bimetallic NPs challenges systematic catalyst evaluation.

Colloidal bimetallic NPs serve as an ideal platform for the exploration of composition-configuration-property relationships, necessary for rational catalyst design. Although an extensive library of noble metal bimetallic NPs exists, much less has been done regarding non-noble Cu-based bimetallic NPs despite their potential as catalysts for CO<sub>2</sub>RR. The aim of this thesis is to advance in the synthesis of Cu-based NPs, with focus on Cu-Ga and Cu-In, which have been predicted or demonstrated to possess interesting catalytic properties.

The thesis starts with an introduction on bimetallic NPs and the different colloidal approaches to synthesize them. Galvanic replacement reactions (GRRs) are discussed more in details, as they are the synthetic approach of choice for the Cu-Ga and Cu-In NPs. Ga and In belong to a family of liquid metals; thus, information on their general properties is also provided.

The first two experimental chapters focus on the reactivity and surface chemistry of Ga NPs. Chapter 3 demonstrates that Ga NPs react with a copper-amine complex to form anisotropic Cu-Ga nanodimers (NDs). Mechanistic studies reveal that a GRR takes place. Yet, the ND morphology differs from the more typical hollow core@shell structures obtained from GRRs. This unusual morphology is attributed to the liquid nature of Ga NPs and to the presence of a native oxide shell. This discovery fostered a follow up study, which is discussed in Chapter 4. The effect of the chemical nature of the capping ligand on the oxide thickness and reactivity of the Ga NPs is investigated. The thickness of the oxide skin is found to greatly depend on the ligands. Specifically, amines and carboxylic acids promote thicker oxide shells while thiols and phosphines hinder its growth. The reaction between Ga NPs with different oxide thickness and the copper precursor leads to a surprising result, while thicker oxides cause the formation of NDs, isolated Cu NPs form with thinner oxides.

Chapter 5 turns towards Cu-In NPs. Following the same synthetic scheme, In NPs with different sizes are exploited as sacrificial seeds for the GRR. Cu-In NPs with an unprecedented variety of morphologies and elemental distributions are obtained: spherical  $\text{Cu}_{11}\text{In}_9$  intermetallic and patchy phase-segregated Cu-In NPs, as well as Cu- $\text{Cu}_{11}\text{In}_9$  and Cu-In NDs. Segregation of the two metals occurs as the GRR progresses, with time or with higher copper precursor concentration. Comparing the obtained results with the Cu-In phase diagram reveals that the bigger seeds stabilize the bulk-like Cu- $\text{Cu}_{11}\text{In}_9$  configuration before their complete segregation into Cu-In NDs. Aiding in the development of more predictive synthetic approaches.

Finally, Chapter 6 concludes by summarizing the significance of the achievements, which advance the knowledge on underexplored bimetallic NPs and on the GRR when applied beyond noble metals. An outlook on future developments is also provided.

Keywords: colloidal nanoparticles, bimetallic nanoparticles, liquid metals, galvanic replacement reactions, copper, gallium, indium.

# Résumé

Le besoin de catalyseurs efficaces et sélectives, qui soient capables de réaliser les conversions nécessaires vers une société plus durable, encourage le développement de stratégies pour la synthèse de nouveaux nanomatériaux. Les nanoparticules (NPs) bimétalliques basées sur le Cu sont prometteuses car elles permettent la production sélective des produits à haute densité énergétique via la réduction électrochimique du  $\text{CO}_2$  ( $\text{CO}_2\text{RR}$ ). Néanmoins, de petites variations dans la composition, la distribution élémentaire et la morphologie du catalyseur peuvent énormément affecter leur performance. De plus, la vaste diversité structurale et de compositions des NPs bimétalliques génère un défi dans leur évaluation systématique.

Les NPs bimétalliques colloïdales peuvent servir des bases idéales pour l'exploration de relations entre la composition, la configuration et les propriétés qui en résultent et qui sont nécessaires pour la conception rationnelle des catalyseurs. Même un grand catalogue des NPs bimétalliques basées sur les métaux nobles a été créé, beaucoup moins a été réalisé concernant la synthèse de NPs bimétalliques pas nobles basées sur le Cu. Le but de cette thèse s'inscrit alors dans le contexte de développer des synthèses de NPs bimétalliques basées sur le Cu, en se centrant sur les systèmes Cu-Ga et Cu-In, car des propriétés catalytiques intéressantes ont été prédites voire démontrées.

Cette thèse introduit dans un premier temps les NPs bimétalliques et les différentes stratégies colloïdales qui peuvent être utilisées pour leur synthèse. Les réactions de remplacement galvanique (RRG) sont développées plus amplement, car elles ont été choisies pour la synthèse des NPs de Cu-Ga et Cu-In. Puisque le Ga et l'In appartient à la famille de matériaux connue comme métaux liquides, une discussion sur leurs propriétés générales et aussi fournie.

Les deux premiers chapitres expérimentaux se concentrent sur la réactivité et la chimie de surface des NPs de Ga. Le troisième chapitre démontre que les NPs de Ga réagissent avec un complexe Cu-amine pour former des nanodimères (NDs) anisotropes de Cu-Ga. Une RRG est révélée par des études mécanistiques. Par contre, la morphologie observée des NDs diffère de celle typique habituellement établie dans le cadre des métaux nobles, soit des structures creuses. Cette morphologie, tout à fait inhabituelle, est attribuée à la nature liquide des NPs de Ga et à la présence d'une coquille d'oxyde inhérente à ce métal. Cette découverte encouragea donc une

étude complémentaire, qui correspond au quatrième chapitre. Cette étude se focalise sur l'influence de la nature chimique du ligand sur l'épaisseur de la coquille d'oxide et sur la réactivité des NPs de Ga. Présentement, une relation entre l'épaisseur de la coquille d'oxide et l'affinité vers l'oxide du groupe d'ancrage des ligands a pu être établie. Plus particulièrement, les amines et les acides carboxyliques promeuvent des coquilles plus épaisses tandis que les thiols et les phosphines entravent la croissance de l'oxide. La réaction entre les NPs de Ga avec différentes épaisseurs d'oxide et le complexe Cu-amine mène à des résultats surprenants, où les oxides plutôt fins encouragent la formation de NPs de Cu isolés alors que des NDs se forment lorsque des NPs de Ga avec des coquilles plus épaisses sont utilisées.

Le cinquième chapitre se tourne vers les NPs de Cu-In. Suivant la même synthèse développée pour le premier système, des NPs d'In de tailles différentes sont investiguées comme substrats sacrificielles pour la RRG. Des NPs de Cu-In avec une variété de morphologies et distributions élémentals sans précédent sont obtenues, dont sphères Cu-In avec de composition intermétallique  $\text{Cu}_{11}\text{In}_9$  et aussi avec de phases séparées, ainsi que de NDs de Cu-In et Cu- $\text{Cu}_{11}\text{In}_9$ . La séparation des deux métaux se produit en parallèle avec la RRG, où temps et/ou concentration du précurseur de Cu ont été identifiés comme facteurs discriminants. Une comparaison entre les résultats obtenus et le diagramme de phases révèle que les NPs d'In plus larges stabilisent la configuration Cu-Cu $_{11}\text{In}_9$  avant leur complète séparation en NDs de Cu-In. Une découverte tout à fait intéressant pour le développement des stratégies plus intuitives vers la synthèse de NPs bimétalliques.

Finalement, le sixième chapitre conclues cette thèse en soulignant l'importance de ces découvertes pour faire avancer la connaissance sur les NPs bimétalliques et sur les RRG lorsqu'elles sont appliquées au-delà des métaux nobles. Enfin, les perspectives sur des développements futures sont aussi discutées.

Mots clés: nanoparticules colloïdales, nanoparticules bimétalliques, métaux liquides, réactions de remplacement galvanique, cuivre, gallium, indium.

# Table of Contents

<b>Acknowledgements .....</b>	<b>i</b>
<b>Abstract .....</b>	<b>iv</b>
<b>Résumé.....</b>	<b>vi</b>
<b>Introduction .....</b>	<b>1</b>
1.1. Motivation .....	1
1.2. General overview on bimetallic NPs for CO <sub>2</sub> RR.....	2
1.3. Synthetic approaches towards bimetallic nanoparticles.....	6
1.3.1. Coreduction .....	6
1.3.2. Thermal decomposition .....	7
1.3.3. Seed-mediated growth .....	9
1.3.4. Galvanic replacement reactions.....	12
1.4. Challenges and opportunities when working with Ga and In.....	18
<b>Experimental section .....</b>	<b>21</b>
2.1. General .....	21
2.2. Chemicals .....	21
2.3. Colloidal synthetic procedures.....	22
2.4. Characterization .....	27
<b>Exploring the chemical reactivity of gallium liquid metal nanoparticles in galvanic replacement .....</b>	<b>35</b>
3.1. Introduction.....	36
3.2. Results and discussion.....	37
3.3. Conclusions.....	45
<b>Modulating the reactivity of liquid Ga nanoparticles by modifying their surface chemistry .....</b>	<b>46</b>
4.1. Introduction.....	47

4.2. Results and discussion.....	48
4.3. Conclusions.....	57
<b>Tailoring morphology and elemental distribution of CuIn nanoparticles via galvanic replacement .....</b>	<b>59</b>
5.1. Introduction.....	60
5.2. Results and discussion.....	61
5.3. Conclusions.....	73
<b>Conclusions and outlook .....</b>	<b>74</b>
<b>Appendix 1.....</b>	<b>78</b>
<b>Appendix 2.....</b>	<b>83</b>
<b>Appendix 3.....</b>	<b>90</b>
<b>References.....</b>	<b>101</b>
<b>Curriculum vitae.....</b>	<b>128</b>

# Chapter 1

## Introduction

### 1.1. Motivation

In the current situation of climate emergency and its resulting risks on human societies, scientific efforts need to be directed towards resolving the anthropological CO<sub>2</sub> emission and accumulation problem. In this context, catalysis plays a big role. For inorganic and materials' chemists the challenge becomes to design catalysts which are active and selective towards the desired reactions. This goal can be achieved by developing the synthesis of well-defined nanomaterials with high surface to volume ratio which allow the establishment of structure-properties relationships to direct catalyst discovery.

Among different reactions, the electrochemical CO<sub>2</sub> reduction reaction (CO<sub>2</sub>RR) holds the promise of achieving a CO<sub>2</sub>-closed cycle and of solving the intermittency problem of other renewable sources of energy such as solar and wind.<sup>1-3</sup> Nevertheless, active and selective catalysts are still needed in order to make this process possible.

In this regard, Cu is the only metal that has the capability to reduce CO<sub>2</sub> beyond CO and to catalyze C-C coupling and, hence, form C<sub>2</sub> and C<sub>2+</sub> products, which are usually more interesting in terms of energy densities and economic potential.<sup>3-6</sup> The use of nanoparticles (NPs) instead of their bulk counterparts is certainly beneficial for catalytic reactions due to their higher surface to volume ratios, which makes them more convenient for their implementation as real-world catalysts. Unfortunately, polycrystalline Cu is far from being selective and different strategies are being studied to improve Cu's selectivity.<sup>4,5,7,8</sup> Besides the structural modification of the size and shape of Cu NPs, the incorporation of a second metal with Cu has emerged in the past years as an encouraging strategy to push the selectivity of Cu towards specific and desired products.<sup>9</sup>

The addition of a second metal to Cu can tune its selectivity by altering the electronic and geometric structure of the metal center, leading to changes in the binding energies of the reaction intermediates, or by a phenomenon referred to as tandem catalysis.<sup>8,10-16</sup> The latter consists in the supply of specific reaction intermediates, particularly CO, by the second metal

to Cu so to promote C-C coupling.<sup>17</sup> Choices for the second metal are many and, indeed, promising results have been shown for combinations of Ag, Pd, or Zn with Cu.<sup>18–20</sup> Nonetheless, much more work is still needed and, as a young field of investigation, the exploration of other metals remains to be done. Especially in the case of more oxophilic metals, whose properties are usually understudied at the nanoscale; as they are typically more difficult to synthesize as metallic NPs. For instance, Cu and Ga alloys are predicted to have optimal binding energies towards the CO intermediate product<sup>21,22</sup> and Cu and In bimetallic structures have been recently attracting attention as selective catalysts.<sup>23–33</sup> However, these NPs cannot be obtained with the tunability of composition, morphology and elemental distribution which is required to understand how these features eventually impact their catalytic performance. Therefore, the aim of this thesis is the development of bimetallic NPs of Cu with Ga and In and the acquisition of mechanistic insight behind their synthesis.

The rest of this introductory Chapter will be dedicated to the relevant background on bimetallic NPs, the available methods for their synthesis and the challenges and opportunities of working with Ga and In.

## 1.2. General overview on bimetallic NPs for CO<sub>2</sub>RR

The presence of two different metals within bimetallic NPs offers new possibilities for tuning the physicochemical properties of these materials. For example, synergistic effects may arise when both metals mutually alter their electronic structures and/or when geometric effects, such as generated strains in the crystalline structure, change the total energy of the NP.<sup>8,10–15</sup> Therefore, not only the choice of this second metal and the final composition of the NP are important, but also how the two metals are arranged within each particle. Multiple configurations (i.e. elemental distribution and morphology) are possible and the most common ones are presented in **Figure 1.1**. First, the two metals can be either alloyed or phase segregated. When alloyed, they can form diluted or concentrated alloys and, in the latter, the metals can be randomly distributed in the crystalline structure of the major component or in an atomically ordered new crystalline phase called intermetallic.<sup>34</sup> Then, when phase segregated, even more configurations are achievable, which includes non-centrosymmetric patchy particles, dimers, Janus and centrosymmetric core@shell and core@frame particles.<sup>35</sup>



These different configurations will potentially induce different electronic, plasmonic and catalytic properties.<sup>18,36–39</sup> Accordingly, learning how to control both composition and configuration is of utmost importance for the eventual optimization of these NPs for the desired application. Indeed, well-defined bimetallic NPs provide the ideal platform to explore composition-configuration-property relationships to move towards a more rational catalyst design.<sup>9</sup>

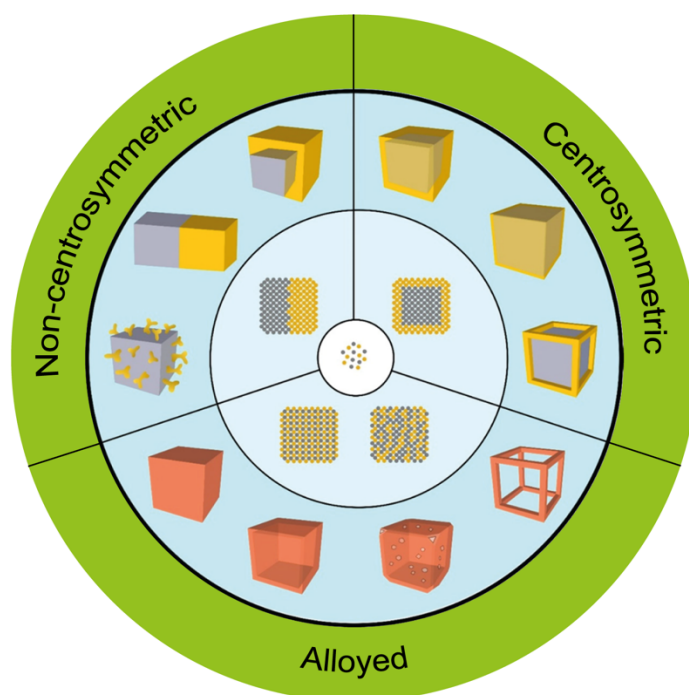


**Figure 1.1.** Schematic illustration showing the evolution from two types of metal atoms (center) to four types of atomic distributions (middle ring), including both non-centrosymmetric and centrosymmetric phase segregated and random alloys and intermetallic NPs, and then a large number of bimetallic NPs with distinct architectures (outer ring). The two different atoms have a yellow and gray color, while an alloy or intermetallic compound has an orange color. Adapted from reference [35].<sup>35</sup>

To remain in the context of CO<sub>2</sub>RR, one study by Kenis and coworkers reports the synthesis of CuPd nanocatalysts as random alloys, intermetallics and phase segregated NPs. By studying their different CO<sub>2</sub>RR catalytic performance, the authors determined that, at least for these CuPd nanocatalysts, phase segregation favored the conversion of CO<sub>2</sub> to C<sub>2</sub> chemicals while more homogeneous alloying was beneficial for methane production.<sup>18</sup> Another two examples from our group include CuAg nanodimers<sup>19</sup> and randomly alloyed CuZn NPs.<sup>20</sup> In the first case, it was demonstrated that having an interface between Cu and Ag was more beneficial for the formation of C<sub>2</sub> chemicals than just a physical mixture of monometallic particles.<sup>19</sup> Regarding the alloyed CuZn NPs, two different compositions were studied. It was established that the NPs

containing more Zn were more selective towards ethanol while the ones with lower Zn content were more selective towards methane.<sup>20</sup> These examples above prove not only the previous point but also that the tuning of a sole parameter can enormously affect the CO<sub>2</sub>RR product selectivity.

Colloidal synthesis is a powerful and versatile approach to form bimetallic NPs, both phase segregated and alloyed, with tunable sizes, shapes, compositions and crystal structures.<sup>34,35,40–43</sup> This approach involves the reduction or decomposition of metallic precursors in the presence of surfactants and sometimes reducing agents, both in aqueous and in organic media. The process can take place in atmospheric conditions or under an inert atmosphere, the latter by connecting the reaction flask to a Schlenk line as depicted in **Figure 1.2a**. According to the classical nucleation theory, the monomers, metastable pre-nucleation structures which can be the metallic precursors themselves or other intermediate species, need to reach high enough concentration levels in solution, the so-called supersaturation, to be able to nucleate and cluster together so to form stable seeds that can continue the growth process (**Figures 1.2b** and **1.2c**). Once formed, colloidal NPs are stable in solution, serving as perfect inks for multiple applications, including catalysis.

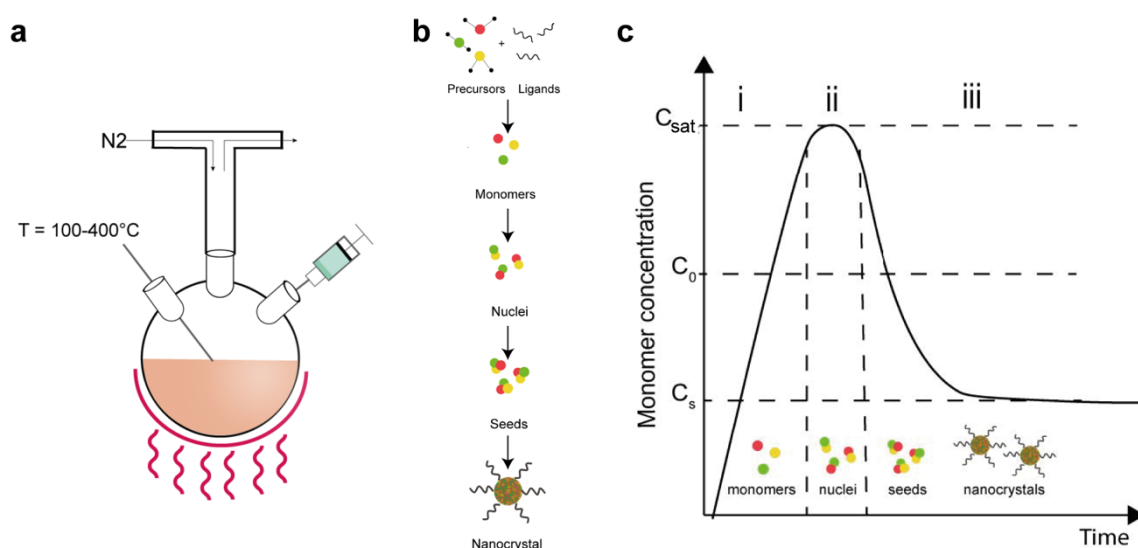


**Figure 1.2.** Schematic illustration showing (a) typical set up used in colloidal chemistry under inert atmosphere which consists of a three-necked flask with a temperature controller connected to a Schlenk line through a condenser, (b) chemical transformations occurring during the reaction and (c) La Mer diagram illustrating these transformations in three stages: (i) formation of monomers, (ii) burst of nucleation into nuclei and (iii) following growth from seeds to NPs.  $C_0$  is the equilibrium concentration,  $C_{sat}$  the supersaturation concentration and  $C_s$  is the solubility level of the bulk solid.

The range of different approaches that one can follow and the possibility to controllably vary several reaction parameters has proven useful to advance the mechanistic knowledge on the factors determining the configuration of multicomponent NPs.<sup>44–47</sup> Nevertheless, this control is far from being straightforward. The intrinsic chemical properties of each individual metal are crucial in determining what compositions and configurations are possible for a set pair in the context of the chosen synthetic method. The synthetic methods, as it will be discussed in the next section, include coreduction, thermal decomposition, seed-mediated growth approach and galvanic replacement reactions. In every case, the crystal structure and the lattice parameters of the individual metals, their electronegativities and the bonding energies between the metallic atoms will greatly affect the outcome of the synthesis.

Firstly, the miscibility between the two metals is one of the main driving forces for the extent of mixing and studies on bulk systems are a great reference to estimate random and/or ordered alloy formation.<sup>48</sup> However, this guiding principle is often invalid as we move to the nanoscale as surface energy contributions to the total energy of the NP become much more important.<sup>46,48–52</sup> Secondly, it is not currently predictable how metals arrange within the particle when they phase segregate and literature has shown that multiple configurations can be obtained via similar synthetic conditions.<sup>46,53,54</sup> For instance, Alivisatos and co-workers were able to synthesize both crescents and core@shell Cu-Ag NPs by controlling the ratio between both metals via the same synthetic scheme.<sup>46</sup> They were able to develop a theoretical model based on thermodynamics that could predict both configurations to be in equilibrium by considering both interface and surface energies. This work is significant, yet it considers a very specific scenario in which a non-reducing solvent is used and there is data available on the surface energies of the metals capped with the ligand of choice. As many syntheses are carried out with reducing solvents and multiple ligands, this model is not directly applicable to other systems. Therefore, although theory could be a great tool for a fast screening of different materials, the formation of colloidal NPs occurs in out-of-equilibrium conditions wherein multiple factors play a role. The convolution of reaction time and temperature, metal precursors' chemistry, the use of either reducing or non-reducing solvents and the type of capping ligands, among other parameters such as particle size and shape, render theoretical models extremely challenging. Hence, systematic synthetic studies with strong insight on the reaction and particle formation mechanism are crucial for the development of the field.

In the case of noble metal bimetallic NPs, many compositions and configurations have already been, and keep being continuously, reported. With a strong focus on shape control, both alloyed and phase segregated regular-, hollow- and branched-shaped particles have been obtained.<sup>35,55–59</sup> Although work is still ongoing, in comparison, important reports on non-noble metal bimetallic NPs are fairly scarce. As mentioned before, the main reason being their oxophilicity and thus their incompatibility with water synthesis, which complicates the direct translation of the lessons learned from noble metals to this different class of nanomaterials.<sup>60</sup> Using water as a reaction solvent limits the use of temperature for the reduction to metallic NPs. Nevertheless, water has permitted the systematic study of the redox properties of different metal precursors as well as the open up of a library of reducing agents of different strength and chemistry.<sup>61</sup> Both factors providing a tuning of the reduction process and contributing to the exploration of noble metal bimetallic NPs of different composition and configuration.

A few reports exist on Cu NPs synthesized in water.<sup>62–69</sup> Yet, although obtaining metallic Ga and In, our metals of interest, in this medium might be possible, it would only be in the presence of highly reducing agents, clearly limiting the tunability of the synthesized NPs. Therefore, the work presented in this thesis is limited to the use of organic solvents as the reaction media. The use of organic solvents provides the opportunity of working under inert conditions and a wider temperature range, up to above 330 °C instead of 100 °C in water, which expands the metal precursors and approaches which can be explored.

### **1.3. Synthetic approaches towards bimetallic nanoparticles**

This section is dedicated to the different synthetic approaches used in colloidal chemistry for the synthesis of bimetallic NPs, whether in water or in organic solvents, with special emphasis on the most relevant methodology for this thesis, which is the galvanic replacement reaction (GRR).

#### **1.3.1. Coreduction**

Coreduction is the simplest approach for the synthesis of alloyed noble metal bimetallic NPs.<sup>35</sup> As its name indicates, this method relies on the simultaneous reduction of two different metal

precursors into metallic atoms in order to nucleate and grow together into the bimetallic NPs. Random alloys are typical reaction products.<sup>16,35,70,71</sup> However, intermetallic structures can also form after a subsequent annealing steps<sup>72,73</sup> or by forcing the synthesis into a kinetic regime.<sup>74,75</sup>

The nucleation and growth of the bimetallic NPs strongly depends on the rate at which the metal precursors are reduced to metal atoms by the reductants. This reduction rate can be modified via the reduction potentials of the metal precursors, the relative concentrations between them, the strength of the reducing agent, the type of capping agent and the reaction temperature.<sup>16,35,70,71,76–79</sup>

As both metal precursors must get reduced at the same time, obtaining bimetallic NPs of metal ion pairs with relatively large differences of reducing potentials is not a straightforward task. Strategies to change the intrinsic redox properties of metals exist and include the manipulation of the ligands as one example.<sup>35</sup> However, co-reduction is certainly more appropriate for metal pairs with similar redox potentials.

Therefore, despite being a widely used technique for the synthesis of bimetallic NPs, coreduction is, *a priori*, not a wise choice for Cu-Ga and Cu-In bimetallic NPs, the metal pairs of interest in this thesis. As discussed later on in this Chapter, both the reduction potentials and crystalline structures of Ga and In are too different from those of Cu. These differences would most likely lead to Cu and Ga or In nucleating separately to form a physical mixture of monometallic NPs.

### 1.3.2. Thermal decomposition

Thermal decomposition is based on the concomitant thermolysis of the two metal precursors into zero-valent metal atoms that nucleate and grow into bimetallic NPs. This approach has been widely used for the synthesis of semiconductors,<sup>80–82</sup> monometallic<sup>41,60,83</sup> and metal-oxide<sup>84–89</sup> NPs. Although thermal decomposition is also possible in water medium, this method is usually carried out in organic solvents, which allow for reaction temperatures above 100 °C. These higher temperatures are usually needed to decompose many metal precursors. Indeed, it will be the technique of choice for the synthesis of Ga and Ga<sub>2</sub>O<sub>3</sub> NPs during this thesis.

Thermal decomposition can be divided into two types depending on the temperature profile, which are heat-up and hot injection.<sup>90,91</sup> Both having advantages and disadvantages depending on the system of choice. In the heat-up method, metal precursors are added to the reaction vessel before increasing the temperature, eventually leading to their decomposition and subsequent nucleation and growth of the NPs.<sup>91,92</sup> This method has been more generally used for metal oxides (e.g. iron and titanium oxide), wherein the monomers are generated and accumulate in-situ following the reaction of the metal precursor itself with one of the ligands.<sup>88,92–94</sup> On the other hand, in the hot injection method, the reaction temperature is increased up above the thermal decomposition temperature before the metal precursor solution is rapidly injected, followed again by a burst of nucleation and the NP growth. This method has been more generally used for semiconductors (e.g. cadmium selenide), wherein highly reactive precursors are normally available.<sup>91,95–100</sup>

In the synthesis of bimetallic NPs by thermal decomposition, ideally both metal precursors should have a similar decomposition temperature. This requirement is important especially when the aim is to form alloys. Yet, similarly to coreduction, the difference in decomposition rates can be compensated by controlling the relative concentrations of both metal precursors.<sup>101</sup> Other parameters such as the chosen surfactants and capping ligands, the nature of the solvent and the reaction time and temperature, can be all modified in order to tune the composition, size and shape of the resulting particles.<sup>35,60,102</sup>

Moreover, one can use metal precursors with relatively different thermal decomposition temperatures to their advantage to generate core@shell NPs in a one-pot approach.<sup>103</sup> By limiting the reaction temperature so to just decompose the less stable metal precursor and not the second one, it is possible to generate monometallic NPs of the first metal while the second precursor remains intact in solution, which corresponds to an in-situ seeded growth (see next section). These monometallic NPs can then foster the decomposition of the second metal precursor with or without an increase in temperature by also facilitating heterogeneous versus homogeneous nucleation.<sup>104</sup> Nevertheless, if the temperature required to promote the decomposition and nucleation of the second metal is too high, the formed monometallic NPs could degrade beforehand. Therefore, this approach is not valid for every metal pair. Another solution, when chemically possible, is to use bimetallic precursors based on a heteronuclear cluster complex in which stable metal<sub>1</sub>-metal<sub>2</sub> bonds are already present.<sup>105,106</sup>

Bimetallic NPs can also be synthesized by combining thermal decomposition with other methodologies, like seeded growth approach and galvanic replacement reactions, as it will be discussed later, as well as simultaneous reduction of the metal precursor. In the latter, in a simultaneous manner by concomitantly reducing the metal precursor with the lower reduction potential and thermally decomposing the more thermally stable metal precursor. This approach has allowed the synthesis of FePt and CoPt<sub>3</sub> NPs, to cite two examples.<sup>107–109</sup>

As mentioned above, thermal decomposition has been used in this thesis for the synthesis of monometallic Ga NPs. The synthesis of bimetallic Cu-Ga bimetallic NPs by thermal decomposition was attempted without success at the beginning of this PhD research project. Indeed, Cu and Ga formed as individual monometallic NPs. This result is most likely due to the differences in decomposition temperatures, as well as the disparity between the crystalline structures of the two metals that challenges the formation of both dimeric and alloyed NPs.

### 1.3.3. Seed-mediated growth

Seed-mediated growth, or seeded growth, is the main route for the synthesis of well-defined bimetallic NPs and, although a direct obtention of alloys is extremely challenging, the annealing of the as-synthesized NPs can lead to their formation.<sup>35,110</sup> Pre-formed NPs of one metal, usually synthesized by reduction or thermal decomposition, are used as seeds for the nucleation of the second metal, which could be again driven by both reduction and thermal decomposition.<sup>111,112</sup> By enabling the newly formed monomers (e.g. metallic atoms) to be directly added onto their surface, these pre-existing NPs lower the activation energy for nucleation and growth. Meaning that, for this process to occur, the required concentration of monomers of the second metal is significantly lower than if no monometallic NPs were already present in solution (**Figure 1.3**).<sup>110</sup> Therefore, this approach allows to circumvent homogeneous nucleation, in favor of heterogeneous nucleation, and directs the formation of bimetallic NPs as long as the concentration of metallic atoms in solution does not surpass the supersaturation levels<sup>110</sup> (**Figure 1.2c**). As both the reduction and decomposition rates of metal precursors into monomers are related to the given energy, lower reaction temperatures can be used to avoid homogeneous nucleation.

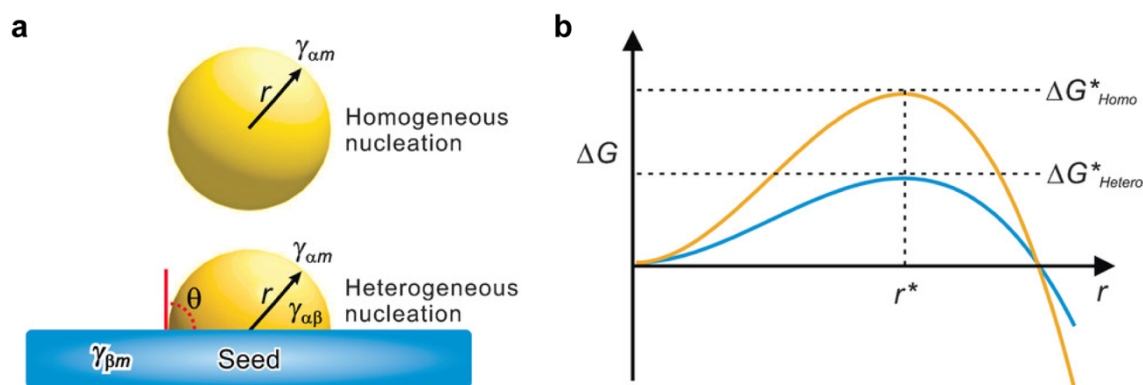


**Figure 1.3.** (a) Homogeneous nucleation (top) in the reaction solution and heterogeneous nucleation (bottom) on the surface of a seed; (b) plot of the Gibbs free energy as a function of size for homogeneous nucleation (yellow line) and heterogeneous nucleation (blue line).<sup>110</sup>

In the bimetallic NPs resulting from seeded-growth, the composition and structure of the metallic NPs used as seeds is normally preserved. The correlation between the crystal structure and the lattice parameters of the seeds and of the second metal (i.e. lattice mismatch), as well as their physicochemical properties, will determine the final configuration of the bimetallic NP, which includes centrosymmetric core@shell, and noncentrosymmetric heterostructured NPs, among others.<sup>113</sup> Three main criteria that should be met in order to achieve centrosymmetric conformal growth (core@shell): (i) the lattice mismatch should be smaller than about 5% and the shell metal should be that one with smaller radius, (ii) the electronegativity of the shell metal should be lower than the core metal, and (iii) the bonding energy between the metal atoms of the shell should be smaller than that between the shell atoms and substrate atoms.<sup>114</sup> A similar crystal structure between the two metals is also important when aiming at non-centrosymmetric NPs, such as dimers. Since most metals have a cubic crystalline structure, this restriction is not usually applicable. Yet the mismatch and resulting strain between a cubic crystalline structure and a growing tetragonal domain could difficult the formation of such interface, favoring the homogeneous nucleation of the latter. To cite one example in non-metallic systems, the development of heterostructures containing a copper indium sulfide (CIS) domain, possessing a tetragonal crystal structure, is extremely challenging.<sup>115</sup>

While the inherent structure and properties of the metals are important, changing the reaction conditions, especially the surface ligands, can modulate the surface energies thus inferring some degree of freedom with regards to the nanoscale arrangement of the two metallic domains.<sup>17,116,117</sup> Moreover, the finally morphology of the bimetallic NP can also be controlled by the ratio of atom deposition and surface diffusion rates on the surface of the seed and



growing crystal. Indeed, the reaction can occur under two different regimes, thermodynamic and kinetic, and distinct products will be obtained depending on the aforementioned reaction conditions (**Figure 1.4a**). A thermodynamic product will be favored when the reaction temperature is relatively high and the deposition rate is relatively low. The diffusion of atoms in the surface towards the formation of most thermodynamically stable interfaces will be then be favored. Conversely, a kinetic product will deviate from the thermodynamic shape because, for instance, the deposition of atoms is too fast and not enough energy is provided to the system to reach the most thermodynamically stable product<sup>35,118–120</sup> (**Figure 1.4b**).

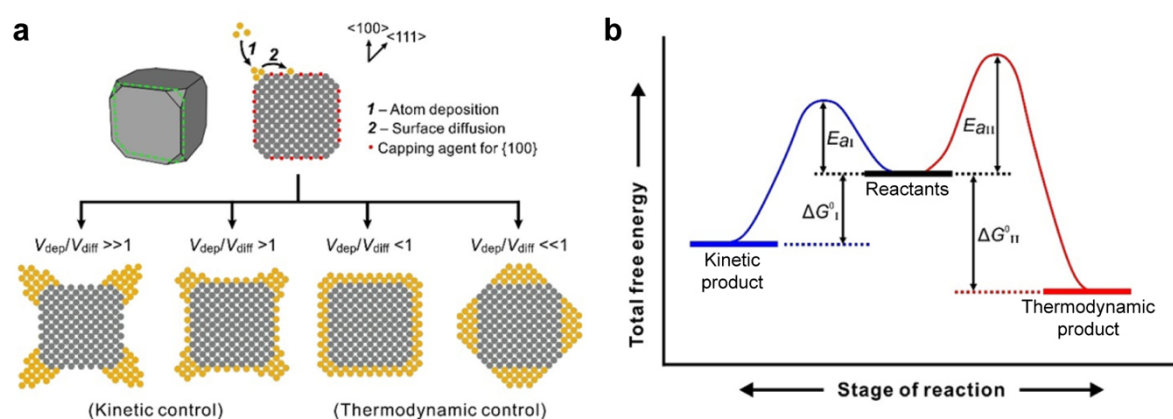


**Figure 1.4.** (a) Scheme showing the shape evolution of a cubic seed with side faces covered by a capping agent under four distinct kinetic conditions. The 2-D atomic models correspond to the cross-section of the 3-D model indicated by a dashed green box; (b) schematic illustration of two different reaction pathways under kinetic and thermodynamic controls, respectively.<sup>35,118</sup>

Generally, the seed-mediated growth is the most versatile technique to synthesize bimetallic NPs, as it enables the formation of a wide range of particle configurations including core@shell,<sup>121,122</sup> alloys,<sup>122</sup> nanoframes,<sup>120</sup> dendritic structures,<sup>123</sup> as well as asymmetric NPs,<sup>124</sup> such as dimers.<sup>53</sup> Unlike one-pot approaches like the ones discussed in the previous sections, seed-mediated growth is more reliable and provides higher reproducibility between batch-to-batch and much more control over the bypassing of homogeneous nucleation.<sup>35</sup>

To cite some examples testifying the versatility of this technique, our group has recently developed a seeded growth approach where Ag seeds were used for the synthesis of Ag-Cu nanodimers. The choice of a mild reducing agent was key to achieve heterogeneous nucleation of purely metallic Cu at 150 °C.<sup>17</sup> Another great example is the formation of PdAg bimetallic NPs of different configurations, core@shell, nonconcentric nanocubes and dimers, that were

all obtained by Xia and coworkers by simply modulating the injection rate of the Ag precursor into the Pd nanocubes seed solution.<sup>53</sup> When using slower injection rates, the deposition of Ag slowly occurs on only one side of the Pd cube. Instead, a faster injection leads to a faster deposition in all six sides of the cube to form core@shell NPs, with a moderate injection promoting the formation of noncentrosymmetric Pd-Ag nanocubes.

In respect of the synthesis of Cu-Ga and Cu-In, pure seeded-growth was initially discarded because of the different crystalline structures of the metals: Cu has a cubic crystal structure while Ga is liquid at room temperature (rhombohedral when solid) and In has a tetragonal crystal structure. Nevertheless, Yarema and coworkers recently designed a synthetic route in which M-Ga intermetallics, including CuGa structures, could be synthesized by an amalgamation seeded growth process not limited by epitaxial constraints.<sup>43</sup> Indeed, this new colloidal approach proved very promising for the synthesis of alloyed bimetallic structures containing low-melting point elements like Ga and In.

### 1.3.4. Galvanic replacement reactions

The galvanic replacement reaction (GRR) is another common technique to obtain bimetallic and even trimetallic nanoparticles.<sup>35,42,125–127</sup> Generally, GRRs can generally form more complex morphologies than those obtained by seed-mediated growth, including hollow nanostructures with tunable composition and porosity. GRRs are spontaneous electrochemical processes wherein one metallic domain (the sacrificial template) is oxidized by the cations of another metal which possess a higher reduction potential. Upon mixing, the sacrificial template is oxidized and dissolves into the solution while the cations of the second metal with the higher reduction potential get reduced on the template, thus producing hollow or hybrid bimetallic nanoparticles (**Figure 1.5**).<sup>125–129</sup> The driving force is therefore the difference between the reduction potentials of the two metals. The change in the Gibbs free energy ( $\Delta G$ ) is given by:

$$\Delta G = -nFE \quad (1)$$

where  $n$  is the number of electrons transferred in the redox half reaction,  $F$  is Faraday's constant and  $E$  is the potential difference between the electrochemical half reactions. As a spontaneous reaction will occur when  $\Delta G$  is negative, a positive  $E$  is required for a GRR. The larger  $E$ , the

potential difference, is, the more thermodynamically favorable the reaction will be.  $E$  can be calculated using the Nernst equation:

$$E = E^{\circ} + \frac{RT}{nF} \ln Q \quad (2)$$

Where  $E^{\circ}$  is the standard potential difference at 25 °C,  $R$  is the ideal gas constant,  $T$  is the temperature at which the reaction occurs and  $Q$  is the reaction quotient, i.e. the ratio between the chemical activities of the reduced form and the oxidized form at a given time.

GRRs have been widely explored for the synthesis of bimetallic NPs comprising noble metals like Au, Ag, Pd and Pt, mostly in aqueous solution<sup>125,130–134</sup> with a few examples existing in organic solvents.<sup>135</sup> The most common system, and the first example of this reaction at the nanoscale, was the synthesis of Au hollow structures from Ag NPs,<sup>132</sup> which is used as an example to further explain the reaction mechanism (**Figure 1.5**).<sup>136</sup>

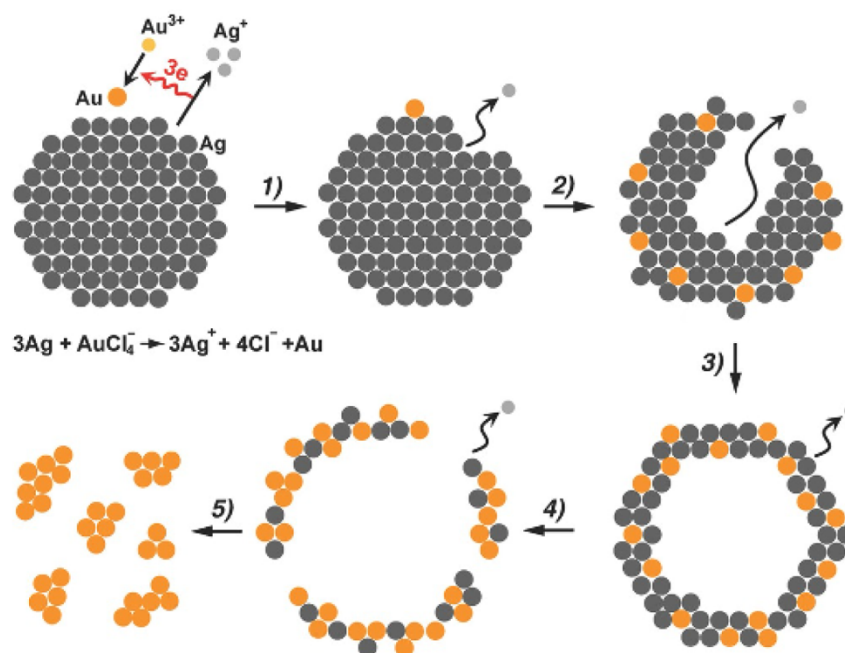
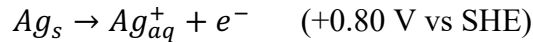


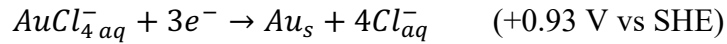
**Figure 1.5.** Schematic illustration of the morphological and structural changes at different stages of the GRR between Ag NPs and HAuCl<sub>4</sub> in an aqueous solution.<sup>125</sup>

The electrochemical reaction that occurs when an aqueous HAuCl<sub>4</sub> solution is added to an aqueous suspension of Ag NPs can be summarized as:

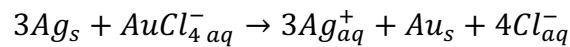
anode half reaction:



cathode half reaction:



combined reaction:



Since  $E > 0$ , then the reaction is thermodynamically favorable. Therefore, once the two solutions become in contact, the GRR is immediately initiated at the Ag sites with higher surface energies, such as defects or steps.<sup>137</sup> The Ag atoms oxidize and dissolve into the solution, which generates pitches on the surface. Concomitantly, the  $AuCl_4^-$  precursor is reduced to Au metallic atoms, which deposit on top of the Ag NP surface. As Au and Ag have the same crystalline structure (*fcc*) and a very little lattice mismatch, the deposition of Au onto Ag happens epitaxially, according to the sacrificial template's shape. A thin and incomplete layer of Au forms on the surface of each Ag NP, thus covering the "surface" Ag atoms and preventing their GRR with the Au precursor. Therefore, the exchange can only continue through the small pitches initially formed, and Ag dissolution will happen from the inside, leading to hollow NPs. In the case of Ag and Au, alloying occurs since AgAu alloys are more stable than phase segregated Ag and Au. The alloying of Ag with Au will then change the  $E^\circ$  and the GRR could very well result in hollow AgAu NPs, nanoshells, that have the same shape as the initial Ag. However, if the concentration of  $AuCl_4^-$  is increased, so will the  $Q$  and hence the  $E$  (equation 2), making the  $\Delta G$  more negative and increasing the driving force for the reaction (equation 1). In that case, the GRR will continue with the alloyed Ag atoms and the structure will go through a dealloying process forming first AgAu nanocages and finally small fragments of pure Au.<sup>125,132,136</sup> Although the crystalline structures and the bonding energies of Ag and Au play an important role in the reaction process described above, these mechanistic details are expected to be applicable to different metal pairs as long as the  $E$  is significant enough.<sup>125</sup>

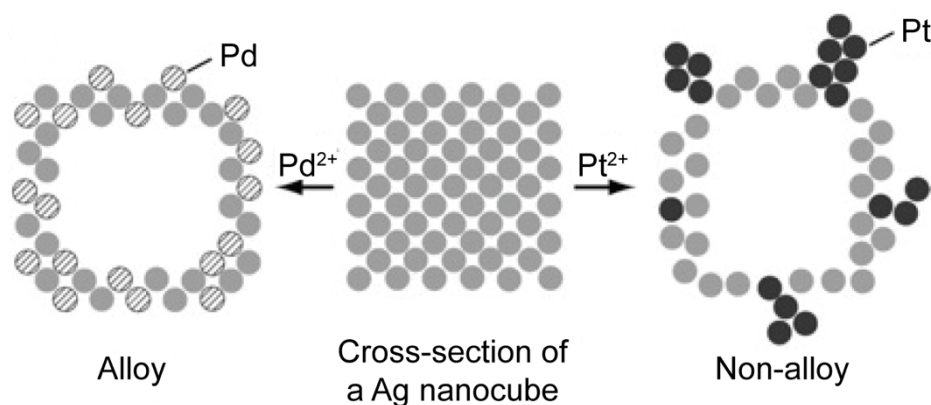


**Figure 1.6.** Schematic illustration of the morphological and structural changes during the GRR between a Ag nanocube and  $\text{Pd}^{2+}$  or  $\text{Pt}^{2+}$  ions.<sup>125</sup>

Whereas hollowing of the sacrificial template seems to be common amongst many materials,<sup>125,138,139</sup> the formation of an alloyed shell is not always possible. An example of this phenomenon is the GRR between Ag NPs and Pt cations. Xia and coworkers compared the GRR of Ag nanocubes with a Pd and a Pt precursor.<sup>140</sup> While smooth nanoboxes of PdAg were obtained, rough polycrystalline nanoboxes covered by Pt islands formed instead when the Pt precursor was used (**Figure 1.6**). These differences were explained based on metal-metal bonding energies favoring segregation of Pt and Ag and intermixing of PdAg and AuAg.<sup>140</sup>

The extent of the GRR mostly depend on the relative concentrations of the metal atom/metal ion pair and/or the reaction time. Thus, modulating concentrations and reaction times enables the formation of multiple configurations of the same bimetallic NPs, which span from solid structures with alloyed porous surfaces to alloyed nanoshells and nanocages and monometallic nanoframes.<sup>35,125,127</sup> Ag NPs are the most popular sacrificial template for the GRR with Pd, Au and Pt, due to Ag's lower reduction potential and the well-established colloidal chemistry syntheses that are available in the literature.<sup>138</sup> However, other metals have also been used. For instance, Neretina and coworkers reported on the formation of bimetallic Pt-containing nanoshells by a GRR between Pt precursor and Ag, Cu, Ni, Co and Pb NPs as the sacrificial templates.<sup>138</sup> Other hollow structures formed via the GRR of Cu, Ni and Co with Pt and Pd have been synthesized and demonstrated to possess intriguing magnetic or catalytic applications.<sup>141–146</sup> It is worth mentioning that GRRs are not restricted to the use of metal NPs as sacrificial templates, as a few examples with semiconducting elements and oxide materials can also be found in the literature.<sup>139,147,148</sup>

The possibility of tuning the extent of the galvanic exchange, the large variety of materials that can act as sacrificial templates, as well as all their possible shapes, render the GRR a very powerful and versatile technique for the synthesis of bimetallic NPs. Moreover, GRRs present the same advantages of the seed-mediated growth, which is to lower the activation barrier for nucleation and to offer reaction control under kinetic or thermodynamic regimes. The main and most significance difference is that the seed itself is now acting as a reducing agent of the depositing metal and as its template while being dissolved into the solution. Since the driving force for the bimetallic structure formation is the  $E$  between the metal pairs, lower temperatures can be used for the synthesis compared to thermal decomposition or seeded growth, which makes the GRR a more versatile approach.

Actually, it is noted that the GRR and the typical seeded growth can also co-exist in the same synthesis. When the reduction potential of the metal seed is lower than that of the metal precursor, the GRR occurs spontaneously, whether or not it was the intended and desired approach.<sup>110</sup> If the  $E$  driving the GRR is not high enough, heterogeneous nucleation might occur first and GRR could occur in the later growth stages. Different strategies can be implemented to favour seed-mediated growth over GRR (or vice versa), which include modulating the reduction potential of the metal precursor by forming molecular complexes<sup>149</sup> or introducing reducing agents.<sup>150</sup> Furthermore, approaches can be intelligently coupled to produce unique configurations.<sup>35,125,127,151–154</sup> For example, Camargo and coworkers produced a collection of AgPd, AgPt and AgAu hollow nanoflowers and nanodendrite structures by coupling GRR with seed-mediated growth via reduction (**Figure 1.7a**).<sup>155–157</sup> In another example, Wang and Jing tuned the composition, inner architecture and surface morphology of AgPd bimetallic nanoshells, with enhanced optical tunability and catalytic activity, via the use, or lack, of mild reducing agents (**Figure 1.7b**).<sup>153</sup> Both examples break the limits of traditional GRRs where the shape of the sacrificial template regulates the morphology of the final hollow structure.

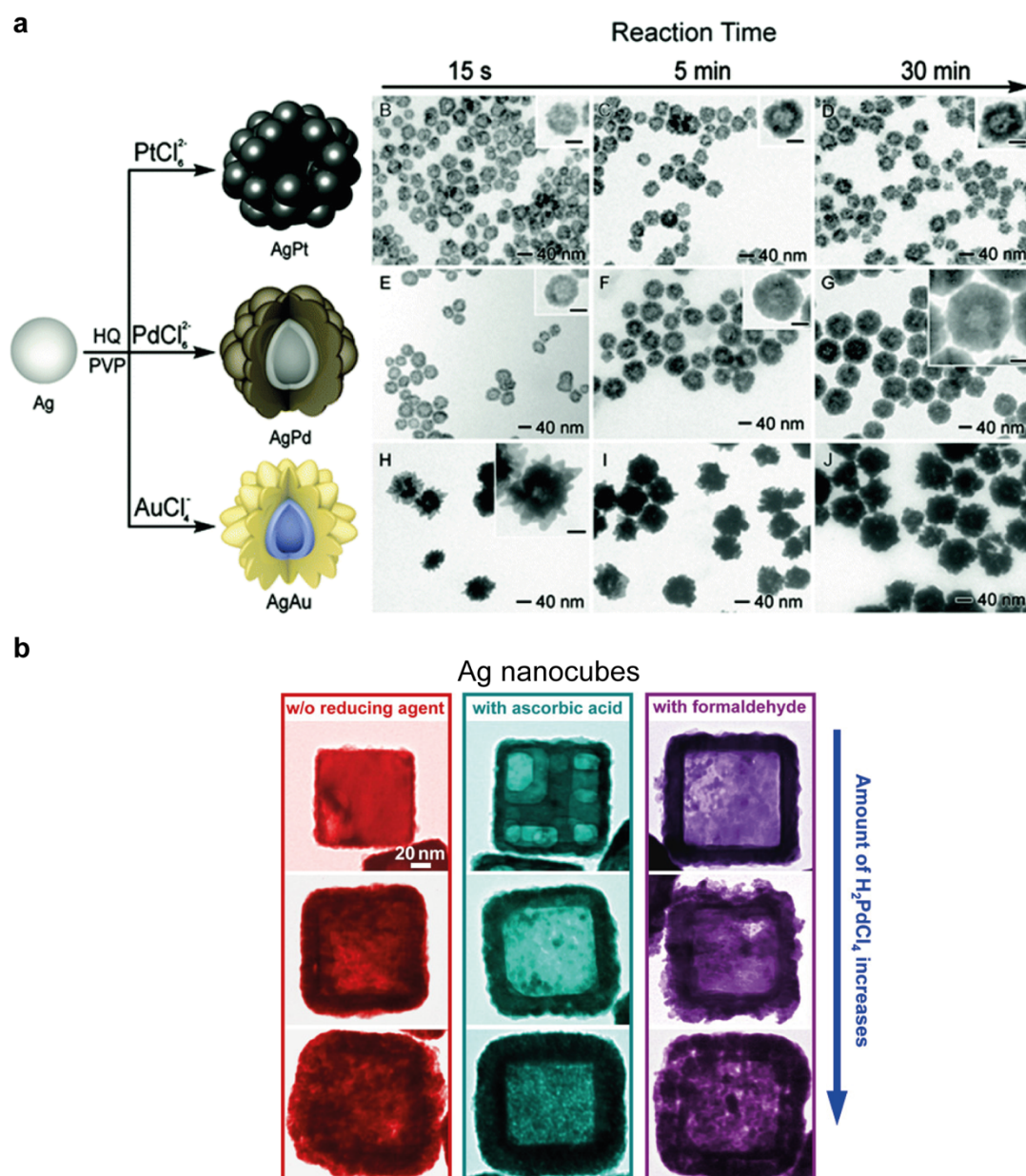


**Figure 1.7.** (a) Schematic representation and corresponding TEM images at different reaction times of the synthesis of bimetallic AgPt, AgPd and AgAu nanoflowers and nanodendrite synthesized by combining GRR and seeded growth via co-reduction with hydroquinone;<sup>127,155–157</sup> (b) TEM images of AgPd nanoshells synthesized from Ag nanocubes possessing different geometries depending on the use or not of a reducing agent and the amount of added Pd precursor.<sup>153</sup>

Bimetallic NPs synthesized via GRRs are very attractive for catalytic applications. Besides the tunability of compositions and configurations, these NPs have much larger reactive surface areas when compared with solid NPs. Indeed, they have been tested as catalysts for a variety of applications including redox reactions and oxygen reduction reactions,<sup>123,127,146,158–164</sup> as well as for CO<sub>2</sub>RR.<sup>165–172</sup> This technique has the potential of creating a library of bimetallic



compositions and configurations of theoretically promising metal pairs, which can be extremely beneficial for the development of catalysts, including those for CO<sub>2</sub>RR. To do so, the extension of the GRRs to non-noble metals is needed.

As for our metal pairs of interest, Cu-Ga and Cu-In, GRRs represent a promising approach for their synthesis, especially considering the large differences in reduction potentials between Cu ( $E^0_{Cu^{2+}/Cu} = +0.34$  V vs SHE) and Ga ( $E^0_{Ga^{3+}/Ga} = -0.53$  V vs SHE) and In ( $E^0_{In^{3+}/In} = -0.34$  V vs SHE).<sup>173</sup> Indeed, a GRR between a bulk galinstan droplet (an eutectic alloy of Ga, In and Sn) and Ag, Au, Pd, Pt and Cu metal precursors was already demonstrated by O'Mullane and coworkers prior to the work done in this thesis.<sup>174</sup> The authors mainly focused on Ag and Au, and described the formation of a black silver or black gold skin forming around the liquid droplet in a progressive manner (**Figure 1.8**). Relevant in the context of this thesis, the reaction with Cu took up to a week instead of the less than 24 h for Ag and Au, which the authors attributed to the lower reduction potential of Cu compared to that of Ag and Au. Despite occurring at the macroscopic level, this work inspired us in pursuing a similar approach at the nanoscale.

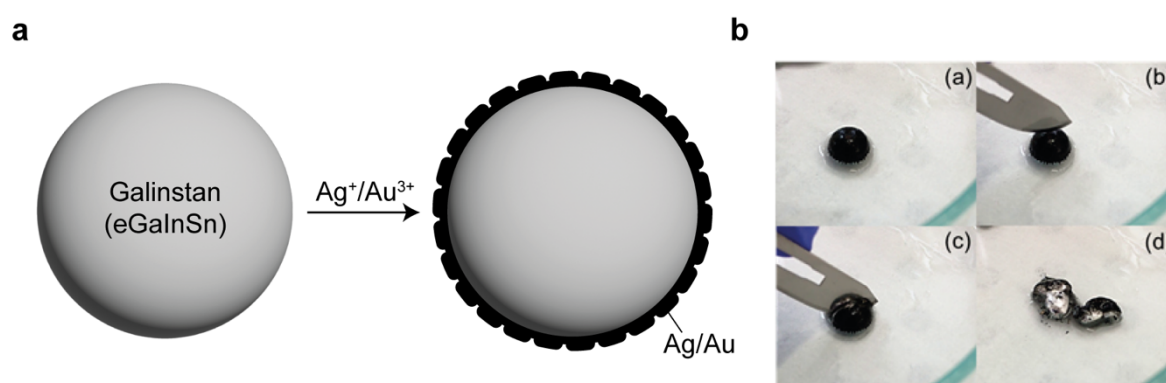


**Figure 1.8.** (a) Schematic representation the GRR between a galinstan droplet and a Ag or Au precursor and (b) successive snapshots of cutting through the black gold skin, exposing unreacted galinstan in the core.<sup>174</sup>

## 1.4. Challenges and opportunities when working with Ga and In

Ga and In possess unique physico-chemical properties, which are underexplored at the nanoscale, which make them fundamentally intriguing systems to study beyond their promising behavior as CO<sub>2</sub>RR catalyst when coupled with copper. Ga and In are oxophilic post-transition



p-block metals, with structures that display low coordination numbers and directional bonding, with a very rich covalent chemistry with other compounds.<sup>175</sup> Unlike most metals, they do not possess a cubic crystalline structure. Instead, Ga and In have rhombohedral and tetragonal structures, respectively.<sup>138</sup> Moreover, Ga is liquid at room temperature and In has a very low melting point of around 156.6 °C, both belonging to the family of liquid metals.<sup>176,177</sup>

Liquid metals (LMs) are elemental or alloyed materials with fascinating properties deriving from their simultaneous metallic and liquid nature.<sup>176–179</sup> Elements and alloys with melting points around or below room temperature are considered explicitly liquid. Nevertheless, due to the typically high melting points of metals (Cu's mp is 1085 °C) and the conditions that are accessible with lab bench equipment, the extended family includes metals whose melting points are below 330 °C, including most notably In, Sn and Bi.

LMs consist of a sea of electrons which are coupled with mobile ionized cores, adding more complexity to their electronic properties compared to solid metals.<sup>176,177</sup> As liquids with water-like viscosities, their metallic bonds purvey them with high density and the highest thermal and electrical conductivities, as well as the highest surface and interfacial tensions among all liquids.<sup>176,177</sup> In particular, Ga has supercooling properties which allows Ga-based materials to remain liquid even below their melting point.<sup>177</sup> As such, these materials are being studied for multiple applications including microfluidics, self-healing contacts in stretchable electronics, biomedical applications, chemical sensors, imaging, materials synthesis, catalysis and batteries.<sup>57,137–146</sup> Besides the previously cited work with Cu-Ga/In bimetallic materials,<sup>1–13</sup> Ga- and In-based LMs are emerging as promising electrocatalysts wherein their continuously dynamically changing surface offers opportunities not possible with solid catalysts, such as resistance to coking or different selectivities accompanying solid-liquid transitions.<sup>185,190,191</sup>

Shrinking the size of the LM particles down to the nanoscale and having inks of well-defined and dispersed LM NPs can benefit many of the above mentioned as well as opening up new venues.<sup>179</sup> Generally, the properties of both Ga and In NPs are unexplored, as well as how their chemistry and properties change at the nanoscale, which represented a challenge and opportunity for the development of this thesis. For instance, under ambient conditions, Ga forms a passivating amorphous oxide shell (**Figure 1.9**). This native shell around the metal core can be easily removed in the bulk via acidic treatment<sup>192</sup> or under an applied voltage.<sup>193</sup> However, as NPs show larger surface to volume ratios and higher surface energies, their

oxidation process is faster<sup>194</sup> and thicker shells can form,<sup>195</sup> thus with surface properties that possibly differ from the bulk, which is not well understood yet anyway. We cannot therefore separate the properties of liquid Ga from those of its native oxide shell when considering their synthesis and properties as monometallic or bimetallic NPs.

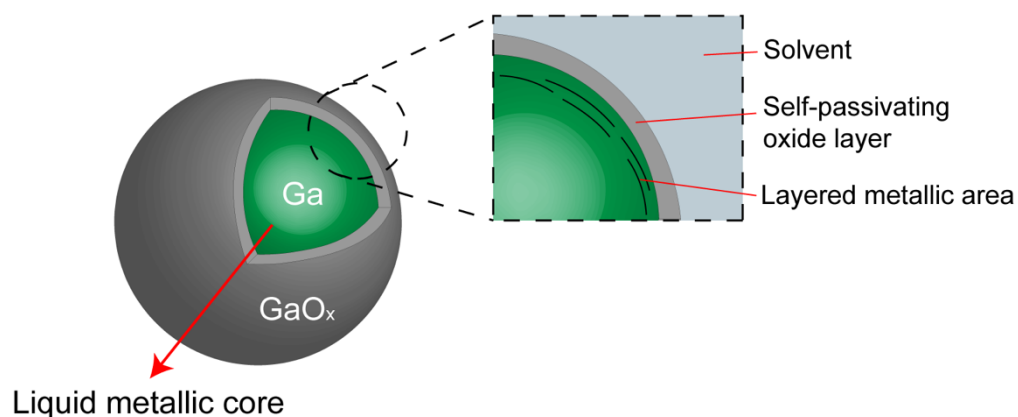


**Figure 1.9.** Schematics depicting the structure of a liquid Ga droplet or NP and description of its interface. Drawing inspired by reference [176].<sup>176</sup>

Altogether, these intriguing phenomena make Ga and In worthy of being further studied at the nanoscale. By combining them with Cu and investigating their reactivity with this metal to form bimetallic NPs, the aim of this thesis was to advance the understanding of their chemistry while developing materials with new catalytic properties and behaviors. For example, one recent work from our group has demonstrated that the native shell of Ga NPs persist even during CO<sub>2</sub>RR conditions and prevents coalescence of these metallic NPs at potential where bulk liquid Ga films should form instead.<sup>190</sup>

## Chapter 2

### Experimental section

#### 2.1. General

All glassware was oven-dried prior to use. All syntheses were carried out under an inert atmosphere using anhydrous solvents and standard glovebox and Schlenk-line techniques. A J-KEM Scientific Model 310 temperature controller together with a heating mantle and a standard lab-bench hot plate were used for reaction temperature control. Post-synthetic purification (“washing”), ligand exchange, handling, and storage of the as-synthesized materials were also carried out under an inert atmosphere.

#### 2.2. Chemicals

Chemicals listed in **Table 1** were used as received without further purification.

Chemical	Symbol	Purity	Manufacturer
Copper(II) acetate	Cu(OAc) <sub>2</sub>	99.999%	Sigma Aldrich
Di-n-octylamine	DOA	98%	ABCR
Dodecanethiol	DDT	98%	Sigma Aldrich
Ethanol (anhydrous)	-	95%	Sigma Aldrich
Gallium(III) acetylacetonate	Ga(acac) <sub>3</sub>	99.99%	ABCR
Indium(III) chloride	InCl <sub>3</sub>	99.999%	Sigma Aldrich
Lithium triethylhydridoborate	superhydride	1 M in tetrahydrofuran	ABCR
n-butyllithium	n-BuLi	2.7 M in hexane	Sigma Aldrich
1-octadecene	ODE	90%	Sigma Aldrich
Oleic acid	OLAC	90%	Sigma Aldrich
Oleylamine	OLAM	70 & 80-90%	Sigma Aldrich
Toluene (anhydrous)	-	99.8%	Sigma Aldrich
Tri-n-octylphosphine	TOP	90%	Alfa Aesar
Tri-n-octylphosphine oxide	TOPO	99%	Sigma Aldrich
Tris(dimethylamido)gallium(III) dimer	Ga <sub>2</sub> (NMe <sub>2</sub> ) <sub>6</sub>	99.9%	ABCR

**Table 1.** Chemicals used during the syntheses described in this thesis.

When specified as degassed in the synthesis description, ODE, OLAC, OLAM, DOA and DDT were degassed and dried under vacuum at 110 °C for 4 h, cooled down to room temperature, and then transferred airless to the glove box.

## 2.3. Colloidal synthetic procedures

### Chapter 3

#### Ga NPs (30 nm):

Ga nanoparticles were synthesized by adapting a procedure from Kovalenko and coworkers.<sup>188</sup> In a typical synthesis of 30 nm Ga nanoparticles, 7 mL of ODE were loaded into a 25 mL three-necked flask, equipped with a reflux condenser, and dried under vacuum at 110°C for 1 h. Then the reaction flask was filled with N<sub>2</sub> and heated to 290 °C, followed by an injection of solution containing 50 mg of Ga<sub>2</sub>(NMe<sub>2</sub>)<sub>6</sub> in 3.75 mL of dried ODE and 2.26 mL of dried DOA. This solution was previously prepared by stirring the Ga precursor and the ODE for at least 40 min and then adding the DOA just a few minutes before the injection. Right after the injection, the temperature dropped to 235 - 240 °C, and in ca. 30 sec the reaction flask was cooled to room temperature. Ga nanoparticles were separated from by-products and from unreacted precursors by adding 15 mL of ethanol, followed by centrifugation at 5000 rpm for 20 min. Ga nanoparticles were redispersed in toluene, and the purification/precipitation step was repeated 2 – 3 times. Ga nanoparticles were finally stored in dried ODE or in anhydrous toluene.

#### Ga<sub>2</sub>O<sub>3</sub> NPs (6 nm):

Ga<sub>2</sub>O<sub>3</sub> nanoparticles were synthesized by adapting a procedure by Radovanovic and coworkers.<sup>196</sup> In a typical synthesis of 6 nm Ga<sub>2</sub>O<sub>3</sub> nanoparticles, 0.5 g of Ga(acac)<sub>3</sub> were mixed with 7.0 g of OLAM into a 100 mL three-necked flask, equipped with a reflux condenser, and the temperature was raised to 80 °C. After the Ga precursor was fully dissolved, the reaction flask was degassed and filled with N<sub>2</sub> to then be heated to 310 °C. The reaction mixture was refluxed under these conditions for 7 h. The obtained white powder was washed 3 times by

adding 15 mL of ethanol, followed by centrifugation at 5000 rpm for 20 min while being redispersed in toluene. The obtained NPs were capped with TOPO and dispersed in dried ODE.

#### **Cu-Ga NDs:**

1 mL of a solution of Ga NPs in ODE (4 mM), 1 mL of a solution of Cu(OAc)<sub>2</sub> in ODE (4 mM), 0.5 mL of OLAC and 0.5 mL of OLAM were added to a 5 mL vial and then stirred at 600 rpm on a hot plate which was set at 150 °C inside a glovebox for 15 h. Cu-Ga NPs were separated from by-products and from unreacted precursors by adding ethanol (3 mL), followed by centrifugation at 5000 rpm for 20 min. The final product was then redispersed in toluene, and the purification/precipitation step was repeated 2 – 3 times before finally being stored in anhydrous toluene.

#### **In NPs (22 nm):**

In NPs were synthesized following a procedure by Kovalenko and coworkers.<sup>41</sup> In a typical synthesis of 22 nm In NPs, 13 mL of dried OLAM were mixed with the 0.028g In precursor, InCl<sub>3</sub>, in a 50 mL three necked flask equipped with a reflux condenser, and dried under vacuum at 110°C for 1 h. Then the reaction flask was filled with N<sub>2</sub> and heated to 160 °C, followed by an injection of 2.25 mL of n-BuLi. After another 10 s, 0.3 mL of superhydride were injected and in ~10 s, the reaction was quenched by the injection of 12 mL of anhydrous toluene and immediate cooling with an ice bath. 0.4 mL of dried OLAC were injected at 50 °C. In NPs were separated from by-products and from unreacted precursors by adding 15 mL of ethanol, followed by centrifugation at 5000 rpm for 20 min. In NPs were redispersed in toluene, and the purification/precipitation step was repeated 2 – 3 times. In NPs were finally stored in dried ODE or in anhydrous toluene.

#### **Cu-In NPs.**

1 mL of In NPs in ODE (4 mM), 1 mL of a solution of Cu(OAc)<sub>2</sub> in ODE (4 mM), 0.5 mL of OLAC and 0.5 mL of OLAM were added to a 5 mL vial. The vial is then stirred on a hot plate which was set at 160 °C inside a glovebox for 15 min. The reaction product was separated from by-products and from unreacted precursors by adding ethanol (3 mL), followed by centrifugation at 5000 rpm for 20 min. Cu-In NPs were redispersed in toluene, and the

purification/precipitation step was repeated 2 – 3 times before finally being stored in anhydrous toluene.

#### **Ag-Ga NDs:**

In a typical synthesis, 1 mL of Ga NP solution in toluene (4 mM) and 1 mL of a solution of AgNO<sub>3</sub> in toluene (4 mM) were added to a 5 mL vial and then stirred at room temperature for 4 h. The reaction product was separated from by-products and from unreacted precursors by adding ethanol (2 mL), followed by centrifugation at 5000 rpm for 20 min. Ag-Ga NDs were redispersed in toluene, and the purification/precipitation step was repeated once before finally being stored in toluene.

#### **Ag-Cu-Ga NPs:**

In a typical synthesis, 1 mL of the Cu-Ga NDs solution in toluene (2 mM) and 1 mL of a solution of AgNO<sub>3</sub> in toluene (2 mM) were added to a 5 mL vial and then stirred at room temperature for 8 h. The reaction product was separated from unreacted precursors by adding ethanol (2 mL), followed by centrifugation at 5000 rpm for 20 min. Ag-Cu-Ga NPs were redispersed in toluene, and the purification/precipitation step was repeated once before finally being stored in toluene.

#### **Preparation of Cu(II)-OLAM complex:**

272.4 mg of Cu(OAc)<sub>2</sub> (1.5 mmol) and with 0.5 mL of OLAM (1.5 mmol) were loaded in a 5 mL vial and then stirred on a hot plate at 150 °C inside the glovebox for 3 h. The reaction mixture is dark blue at the beginning but it becomes brown after 1 h heating. The complex was separated from unreacted precursors after 4 washings with hexane, centrifuging at 5000 rpm for 5 minutes until the supernatant was completely transparent for the second time. The remaining hexane was let to evaporate overnight inside the glovebox.

#### **Preparation of Cu(II)-TOP complex:**

272.4 mg of Cu(OAc)<sub>2</sub> (1.5 mmol) and with 0.65 mL of TOP (1.5 mmol) were loaded in a 5 mL vial and then stirred on a hot plate at 150 °C inside the glovebox for 3 h. The reaction mixture is dark blue at the beginning but it becomes yellowish after 1 h heating. The complex

was separated from unreacted precursors after 4 washings with hexane, centrifuging at 5000 rpm for 5 minutes until the supernatant was completely transparent for the second time. The remaining hexane was let to evaporate overnight inside the glovebox.

## Chapter 4

### Ga NPs with different capping ligands:

Ga NPs were synthesized by modifying previously reported procedures.<sup>42,188</sup> In a typical synthesis, 7 mL of ODE were loaded into a 25 mL three-necked flask, equipped with a reflux condenser, and dried under vacuum at 110 °C for 1 h. Then the reaction flask was filled with N<sub>2</sub> and heated to 290 °C, followed by a rapid injection of a solution containing 50 mg of Ga<sub>2</sub>(NMe<sub>2</sub>)<sub>6</sub> in 3.75 mL of dried ODE with a 20 mL syringe, which had been previously prepared in a glovebox. Right after the injection, the temperature dropped to 235 – 240 °C and after 30 seconds the solution color changed from yellow to dark grey, indicating the formation of NPs. The capping ligand of choice (OLAC, OLAM, TOP or DDT) was then injected into the reaction flask with a 50:1 molar ratio to the precursor. The reaction flask was then rapidly cooled down to room temperature using an ice bath. The Ga NPs were separated from any by-products and from unreacted precursors by adding 15 mL of ethanol, followed by centrifugation at 5000 rpm for 20 min. The Ga NPs were redispersed in toluene, and the purification/precipitation step was repeated one more time with one more addition of 0.1 mL of the chosen ligand. The Ga NPs were finally stored in anhydrous toluene.

### Cu-Ga NDs:

Similarly to the synthesis of the previous chapter, Ga NPs with different capping ligands in toluene were transferred to ODE to form a 4 mM solution (based on atomic concentration from elemental analysis). Soon after, 1 mL of this new solution, 1 mL of a solution of Cu(OAc)<sub>2</sub> in ODE (4 mM), 0.5 mL of OLAC and 0.5 mL of OLAM were added to a 5 mL vial and then stirred at 600 rpm on a hot plate at 150 °C inside a glovebox for 4 h. Cu-Ga NPs were separated from any by-products and from unreacted precursors by adding 3 mL of ethanol, followed by centrifugation at 5000 rpm for 20 min. The final product was then redispersed in toluene, and the purification/precipitation step was repeated once before finally being stored in anhydrous toluene.

**Ligand Exchange Procedure:**

1.5 mL of the OLAC-capped Ga NPs in toluene (5 mM), 0.75 mL of the ligand of choice (OLAM, TOP or DDT) and 1 mL of toluene were added to a 5 mL vial. The mixture was stirred at 500 rpm inside a glovebox overnight. After this time, the excess of ligands was washed away by adding 3 mL of ethanol, followed by centrifugation at 5000 rpm for 20 min. The NPs were then redispersed in toluene, and the purification/precipitation step was repeated one more time before storing them in anhydrous toluene.

**Chapter 5****In NPs of 15, 19 and 22 nm:**

In NPs were synthesized by modifying previously reported procedures.<sup>41,42</sup> In a typical synthesis of In NPs, 13 mL of previously *in situ* dried OLAM were mixed with 0.12 g of In precursor, InCl<sub>3</sub>, in a 50 mL three necked flask equipped with the reflux condenser, and dried under vacuum at 110°C for 1 h. Then the reaction flask was filled with N<sub>2</sub> and heated to 160 °C, followed by a fast injection of 1.13 mL of n-BuLi with a 5 mL syringe. After another 10 s, 0.3 mL of superhydride mixed with 0.7 mL of ODE were rapidly injected with a 5 mL syringe. After some time, the reaction was quenched by the injection of 12 mL of anhydrous toluene and immediate cooling with an ice bath. Depending on the time passed between the second injection (superhydride addition) and the quenching by toluene, different sizes were obtained: ~10 s for 15 nm In NPs, ~20 s for 19 nm In NPs and ~30 s for 22 nm In NPs. Afterwards, 0.4 mL of dried OLAC were injected at 50 °C. In NPs were separated from by-products and from unreacted precursors by adding 15 mL of ethanol, followed by centrifugation at 6000 rpm for 15 minutes. In NPs were redispersed in toluene, and the purification/precipitation step was repeated 2 – 3 times. In NPs were finally stored in dried ODE or in anhydrous toluene, the former as 4 mM solutions.

**Cu-In NPs:**

Modifying the procedure described for Chapter 3, in a typical synthesis of Cu-In NPs, 1 mL of 4 mM solution of In NPs in ODE, 1.5 mL of a 4 mM solution of Cu(OAc)<sub>2</sub> in ODE (0.006 mmol), 0.5 mL of OLAC and 0.5 mL of OLAM were added to a 5 mL vial and then stirred on



a hot plate which was set at 160 °C inside a glovebox for 30 min. A thermocouple positioned inside the reaction medium indicates a temperature of around 128°C. The reaction product was separated from by-products and from unreacted precursors by adding anhydrous ethanol (3 mL), followed by centrifugation at 6000 rpm for 10 minutes. Cu-In NPs were redispersed in anhydrous toluene, and the purification/precipitation step was repeated 2 – 3 times before finally being stored in anhydrous toluene. As it will be further described in Chapter 5 and Appendix 3, the size, morphology and elemental composition and distribution of Cu-In NPs were tuned by adjusting the size of the In NPs templates, the reaction time and the volume of added Cu(OAc)<sub>2</sub> solution.

## 2.4. Characterization

### Electron Microscopy:

Transmission electron microscopy (TEM) images were recorded on a Thermo Fisher Scientific Tecnai-Spirit at 120 kV, equipped with a Gatan camera. High-angle annular dark-field scanning TEM (HAADF-STEM) imaging and energy dispersive X-ray spectroscopy (EDXS) were performed on a Thermo Fisher Scientific Tecnai-Osiris TEM in scanning mode at an accelerating voltage of 200 kV. Atomic HAADF-STEM images were acquired on a double Cs-corrected Thermo Fisher Scientific Titan Themis 60-300 operated at 200 kV. Both Tecnai-Osiris and Titan-Themis microscopes are equipped with a high brightness Schottky X-FEG gun, four silicon drift Super-X EDXS detectors, and Bruker and Velox acquisition software. EDXS data was collected in the form of spectrum images, in which a focused electron probe was scanned in raster across a region of interest in the scanning TEM (STEM) mode. Samples were drop-cast on either a copper or gold TEM grid (Ted Pella, Inc.) prior to imaging.

### Inductively Coupled Plasma – Optical Emission Spectroscopy (ICP-OES):

Previously dried samples were digested with concentrated HNO<sub>3</sub> and then diluted for analysis. The concentrations of the NP solutions were determined on an Agilent 5110 inductively coupled plasma optical emission spectrometry system with a VistaChip II CCD detector.

**Cyclic voltammetry (CV):**

The electrochemical measurements were performed in a custom-made electrochemical cell using a Biologic SP-300 potentiostat. A glassy-carbon disk was used as the working electrode, a platinum wire as the counter electrode and a Ag wire previously soaked in a concentrated HCl solution was used as a quasi-reference electrode. The samples were dissolved in an acetonitrile (MeCN) solution of 0.1 M tetrabutylammonium hexafluorophosphate ([NBu<sub>4</sub>][PF<sub>6</sub>]) as the electrolyte. Cyclic voltammograms were recorded for quiescent solution containing the samples at variable scan rates and were optimal at 10 mV s<sup>-1</sup>. All potentials were then referenced against the ferrocenium/ferrocene couple (Fc<sup>+</sup>/Fc = 0 V). In order to compare with the  $E^0$  of Ga, the potentials were then converted to the Standard Hydrogen Electrode (SHE) scale assuming that  $E^0_{\text{Fc}^+/\text{Fc}} = 0.4 \text{ V vs SHE}$ .<sup>197</sup>

**Attenuated Total Reflectance–Fourier Transform Infrared Spectroscopy (ATR-FTIR):**

FTIR was performed using a PerkinElmer Spectrum 100 instrument by drop-casting 40  $\mu\text{L}$  of the solutions on the ATR window. Air was used as a background measurement and all spectra were recorded with a resolution of 4 cm<sup>-1</sup>.

**Nuclear Magnetic Resonance (NMR):**

All NMR spectra were recorded on a Bruker AVANCE III HD 400 spectrometer fitted with a 5 mm BBFOz probe, operating at 400.13 MHz for <sup>1</sup>H NMR spectra. <sup>1</sup>H NMR chemical shifts were referenced internally to residual solvent resonances (*d*<sub>8</sub>-toluene,  $\delta_{\text{H}} = 7.09 \text{ ppm}$ ), calibrated against an external standard (SiMe<sub>4</sub>, where  $\delta_{\text{H}} = 0 \text{ ppm}$ ).

**X-ray Photoelectron Spectroscopy (XPS):**

Samples were recorded using an Axis Supra (Kratos Analytical) instrument, using the monochromated K $\alpha$  X-ray line of an Al anode. The pass energy was set to 40 eV with a step size of 0.15 eV. The samples were electrically insulated from the sample holder and charges were compensated. Ga NP samples were prepared by drop-casting films onto clean Si substrates inside a N<sub>2</sub>-filled glovebox. XPS fitting was carried out in Kratos ESCApe software. All data were referenced to the principal C1s peak at 284.8 eV after fitting and any deconvolution of the C1s peak. In the Ga2p region, only the Ga2p<sub>3/2</sub> peaks were used for fitting and quantification. In the Ga3d region, both Ga and GaO<sub>x</sub> peaks were fitted with contributions from spin-orbit coupling; the Ga3d<sub>3/2</sub> and Ga3d<sub>5/2</sub> peak separations were fixed at 0.46 eV and the relative intensities were fixed at 0.633. In both regions, the peaks for elemental gallium

were fitted using asymmetric functions. In general, all peaks from a particular region were first fitted with equal linewidths, and then this constraint was relaxed to refine the fit.

### **X Ray Diffraction (XRD):**

The XRD patterns were acquired on a Bruker D8 Advance diffractometer with a Cu K $\alpha$  source equipped with a Lynxeye one-dimensional detector. The diffractometer operated at 40 kV and 40 mA with a Cu K $\alpha$  source with wavelength of  $\lambda = 1.54 \text{ \AA}$ . Samples were prepared by drop-casting nanoparticles on silicon substrates, previously washed with isopropanol and acetone. In Chapter 3 samples were preserved under inert conditions by covering them with a Kapton tape. The tape allowed an air-free measurement but weakened and covered part of the signal from the nanoparticles.

### **Grazing-Incidence X-ray Diffraction (GIXRD):**

Grazing incidence diffraction was performed at  $0.5^\circ$  incidence angle on a Bruker D8 Discover Plus equipped with a Cu rotating anode and a Dectris Eiger2 detector. GID data were refined with Topas using the Rietveld method, heavily constraining displacement parameters and peak shapes due to the limited data quality. Preferred orientation corrections had to be included for certain phases. Samples were prepared by drop-casting the NPs solution on silicon substrates, that had previously been washed with isopropanol and acetone.

### **X-ray Absorption Spectroscopy (XAS):**

XAS measurements were performed at the SuperXAS beamline at the Swiss Light Source synchrotron facility (Paul Scherrer Institute, Switzerland). A Si(111) channel-cut monochromator was used to condition the beam from the corresponding bending magnet. The beam spot was first focused using a vertically collimating mirror and toroidal focusing mirror to approximately  $300 \times 200 \text{ }\mu\text{m}^2$  size. The samples were drop-cast from solution on thin Si wafer substrates inside the glovebox and kept in aluminum bags to avoid exposure to air and light even during the measurements. XAS scans at Ga K-edge (10.3671 keV) and Cu K-edge (8.9789 keV) were conducted in fluorescence geometry using the PIPS detector (up to 2 spectra per second time-resolution). Both edges were scanned during one event and every scan took around 30 min to get a decent signal for the X-ray absorption near edge structure (XANES) spectra. Acquisition of full extended X-ray absorption fine structure (EXAFS) spectra was not possible in this configuration due to the undesired interference from the substrate which led to very intense diffraction peaks. Cu references (Cu foil, Cu<sub>2</sub>O, Cu(OAc), CuO – all diluted in

boron nitride or cellulose) were acquired in transmission mode. For comparison, we used a  $\text{Cu}(\text{OAc})_2$  standard from the Farrel Lytle Database.<sup>198</sup> The reference spectra for  $\text{Ga}_2\text{O}_3$  (in pellet form; diluted in boron nitride) and Ga-metal (thin-film deposited on weighing paper) were collected in transmission and fluorescence geometry, respectively. Data extraction, normalization, and averaging (for increased S/N) were performed using the beamline dedicated software for QEXAFS data analysis, ProXAS.<sup>199</sup> Samples were prepared by drop-casting nanoparticles on low background silicon holders, previously washed with isopropanol and acetone and then preserved under inert conditions by keeping them in sealed aluminum bags (*vide supra*).

#### Calculation of the $\text{Ga}_2\text{O}_3$ shell thickness from XPS measurements (Chapter 4):

The signal intensity of photoelectrons follows an exponential decay from the surface with increasing depth (3), such that the surface atoms make the greatest contribution to the measured signal. Our aim is to find a value for the depth ( $d$ ) of the  $\text{Ga}_2\text{O}_3$  layer that can satisfy the measured Ga /  $\text{Ga}_2\text{O}_3$  ratios in both the Ga2p and Ga3d regions. We must bear in mind that the Ga /  $\text{Ga}_2\text{O}_3$  quantification results are the result of an exponential decay and that the two Ga environments are separated in different phases, i.e. are not homogeneously mixed and do not follow the same signal attenuation with depth.

$$I = I_0 e^{\frac{-d}{\lambda \cos \theta}} \quad (3)$$

$d$  = depth / Å,  $\lambda$  = inelastic mean free path / Å,  $\theta$  = detection angle from the normal / deg.

In our method, we have ignored the fact that the sample is made of spherical NPs, as modelling their geometric effect on the photoelectrons is non-trivial. In relation to this, we have also assumed that all photoelectrons are ejected normal to the surface (i.e.  $\theta = 0^\circ$  and  $\cos \theta = 1$ ). Considering that we are also making use of the *relative contributions* from Ga and  $\text{Ga}_2\text{O}_3$  to the 2p and 3d photoelectron regions, rather than their absolute intensities, we are also able to ignore the intensity values  $I$  and  $I_0$ . Equation 3 therefore simplifies to equation 4, where  $I$  is an arbitrary intensity.

$$I = e^{\frac{-d}{\lambda}} \quad (4)$$

$d$  = depth / Å,  $\lambda$  = inelastic mean free path / Å,  $I$  = arbitrary intensity

In order to evaluate the integral of the exponential decay function, one must have a reasonable approximation for the inelastic mean free path term ( $\lambda$  / Å), which includes a number of important parameters such as material density, atomic mass, atom valency and the photoelectron kinetic energy. In order to do this, we made use of the approximate form of the Bethe equation, developed by Tanuma and coworker, described by Equations 5a–5h.<sup>1</sup> The equations are given here, followed by some discussion of the chosen values for the material-specific variables.

$$\lambda = \frac{\alpha(E) \cdot E}{E_p^2 [\beta \cdot \ln(\gamma \cdot \alpha(E) \cdot E) - (\frac{C}{E}) + (\frac{D}{E^2})]} \quad (5a)$$

$\lambda$  = inelastic mean free path / Å;  $\alpha(E)$  = a relativistic term and is close to 1 for Ga;  $E$  = electron energy, taken as the 2p or 3d kinetic energy / eV;  $E_p$ ,  $\beta$ ,  $\gamma$ ,  $C$  and  $D$  are calculated parameters below.

$$\alpha(E) = \frac{1 + (\frac{E}{2m_e c^2})}{[1 + (\frac{E}{m_e c^2})]^2} \approx \frac{1 + \frac{E}{1,021,999.8}}{(1 + \frac{E}{510,998.9})^2} \quad (5b)$$

$\alpha(E)$  = a relativistic term and is close to 1 for Ga;  $E$  = electron energy, taken as the 2p or 3d kinetic energy / eV;  $m_e$  = mass of the electron;  $c$  = speed of light. We have used the approximate form for simplicity.

$$E_p = 28.816 \left\{ \frac{N_v \cdot \rho}{M} \right\}^{0.5} \quad (5c)$$

$N_v$  = number of valence electrons per atom;  $\rho$  = density of the material / g cm<sup>-3</sup>;  $M$  = atomic weight.

$$\beta = -1.0 + \frac{9.44}{(E_p^2 + E_g^2)^{0.5}} + 0.69\rho^{0.1} \quad (5d)$$

$E_g$  = band gap energy for the material / eV

$$\gamma = 0.191\rho^{-0.5} \quad (5e)$$

$$C = 19.7 - 9.1U \quad (5f)$$

$$D = 534 - 208U \quad (5g)$$

$$U = \frac{N_v \cdot \rho}{M} = \left( \frac{E_p}{28.816} \right)^2 \quad (5h)$$

Considering that the Ga2p photoelectrons possess the lowest kinetic energy, we can consider this region to be the most surface sensitive. Indeed, most of the Ga nanoparticle samples

presented very little amounts of core Ga metal in the Ga2p spectra. For this reason, we decided to focus on the calculation of  $\lambda$  associated with the Ga2p kinetic energy, assuming that  $\lambda$  in this region is primarily determined by Ga<sub>2</sub>O<sub>3</sub>. We therefore used the following values for the material-specific variables in equations 5a–5h:

- $\rho = 6.44 \text{ g cm}^{-3}$  (density of pure Ga<sub>2</sub>O<sub>3</sub>);
- $M = 37.49 \text{ g mol}^{-1}$  (average atomic weight in Ga<sub>2</sub>O<sub>3</sub>);
- $N_v = 12$  (average valency for Ga<sub>2</sub>O<sub>3</sub>, assuming valency of 18 for Ga<sup>3+</sup> and 8 for O<sup>2-</sup>. n.b. This value is very close to that proposed by Powell *et al.*<sup>2</sup> – valency of 13 for Ga<sup>0</sup>);
- $E_g = 4.8 \text{ eV}$  (band gap energy of pure Ga<sub>2</sub>O<sub>3</sub>);
- $E = 370.6 \text{ eV}$  (measured directly from Ga 2p XPS).

The material-specific variables used for the calculation of  $\lambda$  associated with the Ga3d kinetic energy are as follows:

- $\rho = 5.90 \text{ g cm}^{-3}$  (density of pure Ga);
- $M = 69.72 \text{ g mol}^{-1}$  (atomic weight of Ga);
- $N_v = 13$  (using one of the values proposed by Powell *et al.*<sup>2</sup>);
- $E_g = 0 \text{ eV}$ ;
- $E = 1467.6 \text{ eV}$  (measured directly from Ga 3d XPS).

However, it is impossible to describe the changing material density, average atomic weight, valency and band gap energy of the core-shell structure without knowing the thickness of the Ga<sub>2</sub>O<sub>3</sub> shell. We therefore expect much greater error in the calculation of  $\lambda$  and  $d$  using the Ga3d data on their own. Consequently, we relied on the Ga2p XPS data to calculate the associated  $\lambda$  and the thickness of the shell ( $d$ ), and then made use of this  $d$  value to back-calculate the expected Ga / Ga<sub>2</sub>O<sub>3</sub> ratio in the corresponding Ga3d XPS data. Comparing these theoretical ratios with the measured values allowed us to evaluate the validity of the model and give us some idea of the error, which we approximate to be between 3% and 15%. Essentially the calculated  $d$  value should satisfy both 2p and 3d exponential decay functions, such that the integrals are divided to match the observed Ga / Ga<sub>2</sub>O<sub>3</sub> ratios (shown in **Figure 2.1**).

Using the above approach, we calculated the mean inelastic free path for the Ga2p photoelectrons to be 11.3 Å, and the mean inelastic free path for the Ga3d photoelectrons to be

25.0 Å. These values are reasonably close to those predicted from literature data<sup>3</sup>, which would predict values of 10.7 Å and 29.8 Å, respectively.

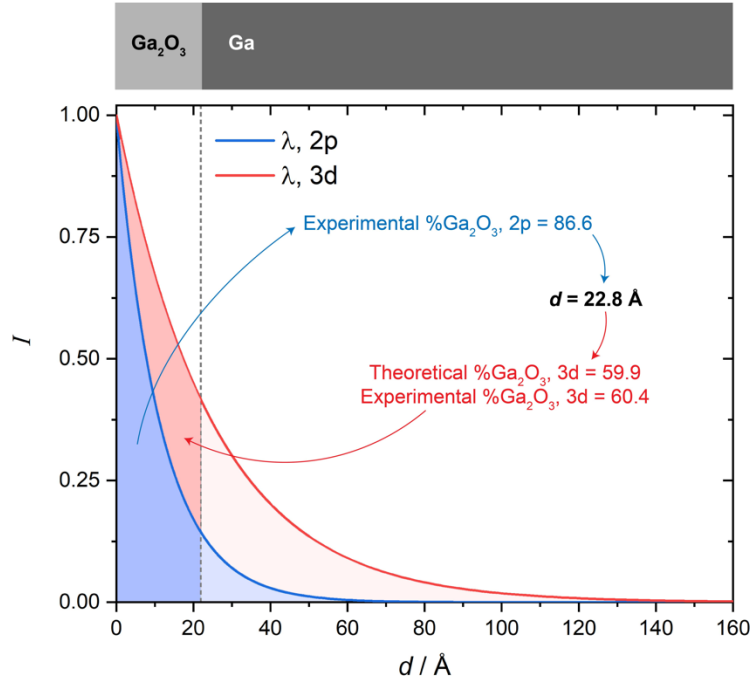


**Figure 2.1.** Graph showing the exponential decay of the signal intensity arising from atoms at a depth  $d$  from the Ga NP surface. The two exponential functions are for the Ga2p and Ga3d regions. An example set of data for aged TOP-capped Ga NPs are shown for illustration, to show how the experimental Ga<sub>2</sub>O<sub>3</sub> / Ga ratio from the Ga2p region is used to calculate  $d$ , and how the validity of this  $d$  value is checked by back-calculating the Ga<sub>2</sub>O<sub>3</sub> / Ga ratio for the Ga3d region, and comparing this theoretical value with the experimental one.

The indefinite integral for the exponential decay function (4) is given by equation 6. The percentage of the Ga2p signal that comes from the Ga<sub>2</sub>O<sub>3</sub> layer is given after evaluating this integral between  $d = 0$  and the unknown  $d$  (7). As the %Ga<sub>2</sub>O<sub>3</sub> is known from integration of the experimental Ga2p XPS data, the equation can be rearranged for  $d$  (8). Note that in order to make use of the %Ga<sub>2</sub>O<sub>3</sub> values, the full area under the Ga2p exponential decay function must first be calculated (from equation 7, using a large  $d$  value as the upper limit) and then multiplied by the %Ga<sub>2</sub>O<sub>3</sub> to give an area that is compatible with the model.

$$\int e^{-\frac{d}{\lambda}} dd = -\lambda e^{-\frac{d}{\lambda}} + C \quad (6)$$

$$\%Ga_2O_3 = \int_0^d e^{-\frac{d}{\lambda}} dd = -\lambda e^{-\frac{d}{\lambda}} + \lambda \quad (7)$$

$$d = -\lambda \cdot \text{Ln} \left( \frac{\% \text{Ga}_2\text{O}_3 - \lambda}{-\lambda} \right) \quad (8)$$

(n.b. The %Ga<sub>2</sub>O<sub>3</sub> and  $\lambda$  values should be associated with the same XPS region.)

Once  $d$  had been calculated from the Ga2p data it was verified by back-calculating the %Ga<sub>2</sub>O<sub>3</sub> for the Ga3d data. Using equation 7, a %Ga<sub>2</sub>O<sub>3</sub> value was obtained, which was compared with the experimental value to approximate the error. We found that this approach provided approximations to the Ga<sub>2</sub>O<sub>3</sub> shell thickness that satisfied both Ga2p and Ga3d datasets to within *ca.* 10%, which is reasonable considering our assumptions of the system.



## Chapter 3

### Exploring the chemical reactivity of gallium liquid metal nanoparticles in galvanic replacement

The content of this chapter is based on the published work: *J. Am. Chem. Soc.* **2020**, 142, 45, 19283–19290. <https://doi.org/10.1021/jacs.0c09458>

**Abstract:** *“Liquid metals possess intriguing properties and micron/nano-sized particles of these materials are gaining popularity for applications in various research fields. Nevertheless, the knowledge of their chemistry is still very limited compared to other classes of materials. In this work, we explore the reactivity of Ga NPs towards a copper molecular precursor to synthesize bimetallic Cu-Ga NPs. Anisotropic Cu-Ga NDs, where the two segregated domains of the constituent metals share an interface, form as the reaction product. Through a series of careful experiments, we demonstrate that a GRR between the Ga seeds and a copper-amine complex takes place. We attribute the final morphology of the bimetallic NPs, which is unusual for a GRR, to the presence of the native oxide shell around the Ga NPs and their liquid nature, via a mechanism that resembles the adhesion of bulk Ga drops to solid conductors. Based on this new knowledge, we also demonstrate that sequential GRRs to include more metal domains are possible. This study illustrates a new approach to the synthesis of Ga-based metal NPs and provides the basis for its extension to many more systems with increased level of complexity.”*

**Authors:** **Laia Castilla-Amorós**, Dragos Stoian, James R. Pankhurst, Seyedeh Behnaz Varandili, Raffaella Buonsanti

**Contribution:** Experiments design, synthesized the NPs, performed all the electron microscopy, XRD, CV and ICP characterization and analyzed the resulting data, wrote the manuscript with contributions from all authors.

### 3.1. Introduction

As discussed in Chapter 1, liquid metals are an interesting class of materials with fascinating properties deriving from their simultaneous metallic and liquid nature.<sup>176–179</sup> Besides their use as self-healing contacts in stretchable electronics, liquid metal micron- and nano-sized particles are being explored for biomedical applications, chemical sensors, imaging, and batteries.<sup>180,182–186</sup> Shrinking the size of the particles down to the nanoscale adds an extra dimension of complexity which generates new physicochemical properties and opens up new applications.<sup>179</sup> Ga-based NPs are the most studied systems so far. Interestingly, Ga NPs have been demonstrated to possess plasmonic properties that are influenced by their size-dependent solid-liquid transition.<sup>188,200</sup> Size-dependent plasmonic properties have also been observed for In-Ga NPs in the UV part of the spectrum.<sup>201</sup> Recently, Ga bimetallic NPs, such as Ga-Pd, Ga-Pt, Ga-Ni, have shown promising catalytic and electrocatalytic performances.<sup>164,185,186,202–205</sup> Theoretical calculations have also predicted that multimetallics including Ga and Cu, among others, are desirable to improve selectivity in the electrochemical CO<sub>2</sub> reduction.<sup>21,22,203</sup>

In order to develop a fundamental understanding of properties at the nanoscale so as to optimize NP performance for targeted applications, synthetic methods that enable size and shape control of NPs are needed. Among these, colloidal chemistry has been demonstrated to achieve superior tunability of metallic NPs with an increasing degree of complexity.<sup>102,111,118,125,131,206–213</sup> However, most of the synthetic development has been carried out on noble metals.<sup>111,118,125,131,206–213</sup> While some of the acquired knowledge within the community can certainly be translated to different systems, new mechanisms might be involved in the formation of non-noble metal NPs. For example, because of their higher oxophilicity, the presence of oxide shells should be taken into account as an important factor during the synthesis. In this work, we explore the reactivity of Ga NPs as seeds to synthesize Cu-Ga bimetallic NPs. We find that Cu-Ga NDs form as the reaction products. We combine TEM, ICP elemental analysis, CV and XAS to investigate the formation mechanism of these anisotropic bimetallic nanostructures. We determine that a galvanic replacement reaction takes place and that the peculiar characteristics of the Ga NPs (i.e. their native oxide shell and liquid nature) determine the final ND morphology. Based on this understanding, trimers including Ag-Cu-Ga were also obtained. By demonstrating the applicability of GRR to the construction of multimetallic NPs

based on liquid metals, this study paves the way towards future developments of this underexplored class of materials.

## 3.2. Results and discussion

In a typical synthesis of the Cu-Ga NPs (**Figure 3.1a**), the Ga seeds are mixed in the reaction vessel with the Cu precursor (copper(II) acetate,  $\text{Cu}(\text{OAc})_2$ ), oleylamine (OLAM) and oleic acid (OLAC) in octadecene (ODE), and then the mixture is stirred for 15 hours under inert atmosphere on a hot plate which was set at 150 °C.

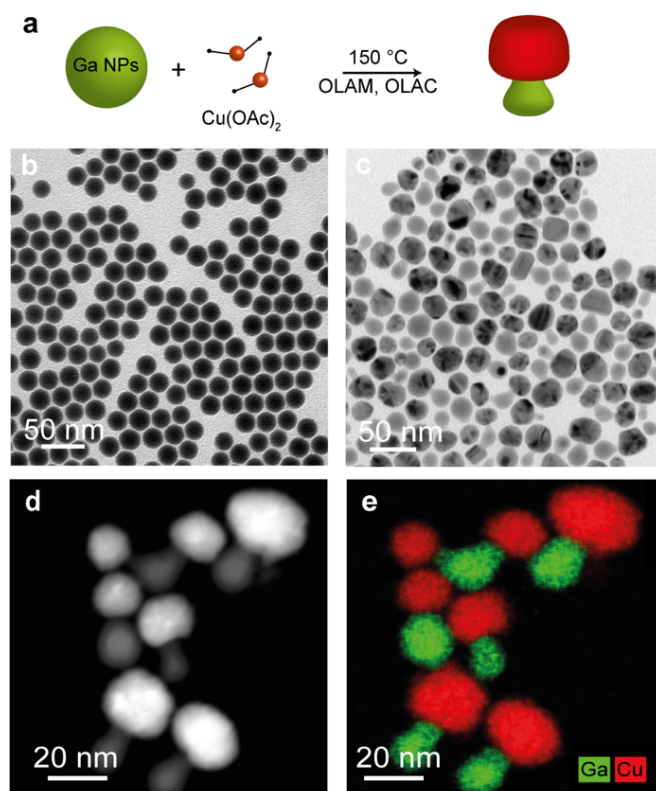


**Figure 3.1.** (a) Sketch of the reaction scheme; (b,c) low-resolution TEM image of the as-synthesized Ga NPs and Cu-Ga NDs, respectively; (d,e) HAADF-STEM image and corresponding EDXS elemental maps of the NDs, respectively.

**Figure 3.1** gives an overview of the electron microscopy characterization of the Ga NPs and of the obtained Cu-Ga bimetallic NPs. **Figure 3.1b** illustrates the spherical shape and size monodispersity of the starting Ga seeds ( $30 \pm 3$  nm, **Figure A1.1**). The product of their reaction with  $\text{Cu}(\text{OAc})_2$  is reported in **Figure 3.1c**. Mushroom-like NDs, where a spherical domain is interfaced to a drop-shaped domain, are observed. The high angle annular dark field-scanning

TEM (HAADF-STEM) imaging with the corresponding energy dispersive X-Ray spectroscopy (EDXS) mapping (**Figures 3.1d,e**) evidences that the spherical domain is Cu while the drop-shaped domain is Ga. Consistently with this picture, a strong diffraction contrast indicating crystallinity is present only in the Cu spheres. X-ray Diffraction (XRD) analysis (**Figure A1.2**) under an air-free atmosphere confirmed the presence of crystalline metallic copper while no Ga was detected, which is consistent with its amorphous nature in the TEM image. Notably, compared with the initial Ga seeds in **Figure 3.1b**, the Ga domain has a decreased size and a deformed shape, and is most narrow near the interface.

To gain further insight into the ND formation mechanism, aliquots were extracted from the reaction mixtures at different times. **Figure 3.2** reports the TEM characterization of these samples. The images show a progressive reduction of the spherical Ga domain over time, accompanied by growth of the Cu domain (**Figures 3.2a-e**). Longer reaction times result in complete dissolution of the metallic Ga such that only the Cu domains are clearly detected along with some lower contrast debris (**Figure 3.2f**). Consistently with these data, elemental analysis of the supernatant confirmed the increasing concentration of Ga and decreasing concentration of Cu as the reaction progressed. A control experiment verified that the reaction conditions alone, in the absence of Cu, do not cause any change in the Ga NPs (**Figure A1.3**).

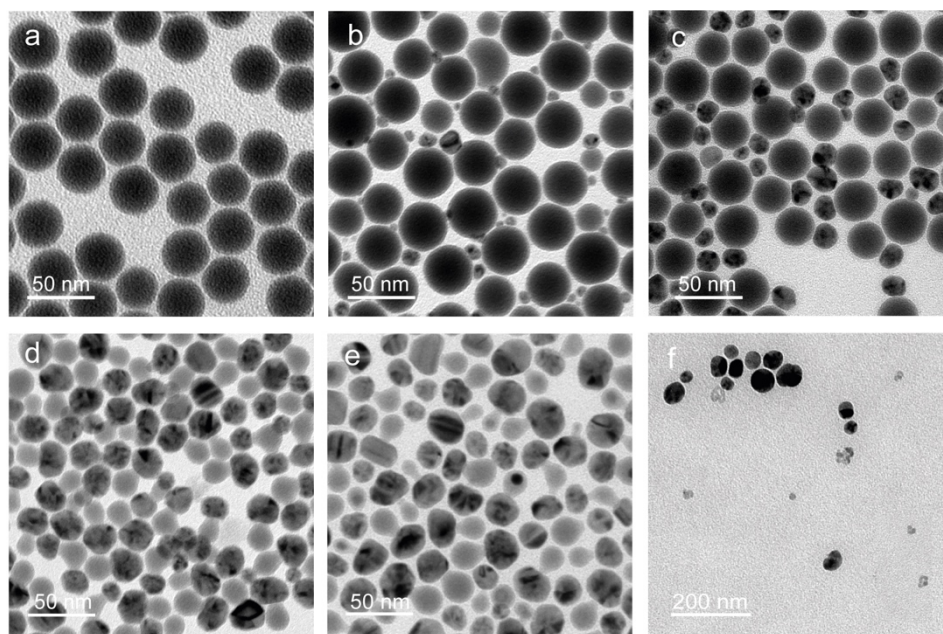


**Figure 3.2.** TEM images of samples collected at different times during the synthesis of the Cu-Ga NDs: (a) 0 min, (b) 2 h, (c) 7 h, (d) 11 h, (e) 15 h and (f) 20 h.

The results above and the standard reduction potentials of Ga and Cu ( $E^0_{Ga^{3+}/Ga} = -0.53$  V vs SHE and  $E^0_{Cu^{2+}/Cu} = +0.34$  V vs SHE)<sup>173</sup> suggest that a GRR might be taking place. GRRs are spontaneous electrochemical processes wherein one metallic domain (the sacrificial template) is oxidized by the cations of another metal that possesses a more positive reduction potential. GRRs have been exploited extensively to synthesize a variety of nanostructured materials; these are mostly based on noble metals but have also been extended to metal oxides more recently.<sup>125,132,134,139,152</sup> Based on these studies and considering that Cu and Ga can form solid solutions,<sup>214</sup> NPs with a hollow interior and an alloyed shell are expected as the GRR product.

In order to explain the formation of the atypical ND configuration, first of all we need to assess the contribution of the organic ligands, as examples in the literature show that they can impact the final morphology of the GRR-derived NPs by acting as surface passivating species or co-reducing agents.<sup>125,127,151,153,154</sup> Another unique feature of the Ga NPs is their liquid nature and the presence of a native self-passivating oxide shell.<sup>176–179,188,192,215</sup> The fate and role of such an oxide skin during the ND formation also deserves investigation.

Starting with the organic ligands, the simultaneous presence of OLAM and OLAC is needed for the ND to form (**Figure A1.4**). OLAM is a well-known reducing agent in the synthesis of NPs in organic solvents,<sup>216</sup> therefore it might contribute to the reduction of Cu(OAc)<sub>2</sub> during GRR. It is worth noting that, in the absence of the Ga seeds or in the presence of gallium oxide NPs (**Figure A1.5**), no Cu NPs form under the same reaction conditions, thus OLAM alone is not sufficient for their nucleation. At the same time, if substituted with a stronger reducing agent, such as trioctylphosphine (TOP), Cu homogeneously self nucleates without any change in the Ga NPs.

One additional consideration is that both OLAM and TOP can coordinate copper ions.<sup>102,216</sup> While the feasibility of GRRs is normally established based on the standard redox potential of the metals, a different coordination environment can dramatically impact the redox potentials of the Cu ions in solution. To gain further insight, we studied the redox properties of the complexes that form when Cu(OAc)<sub>2</sub> is reacted with only OLAM or TOP by performing cyclic voltammetry (CV) experiments (**Figure 3.3**). We will refer to these complexes as Cu(II)-OLAM and Cu(II)-TOP. The CVs of the Cu(OAc)<sub>2</sub> and Cu(II)-OLAM complexes both show two reduction waves; the first is attributed to the Cu<sup>2+</sup>/Cu<sup>+</sup> reduction and the second, which

appears at more negative potential, is attributed to the  $\text{Cu}^+/\text{Cu}^0$  reduction, in agreement with other literature reports.<sup>217–219</sup> Both peaks are anodically shifted in the OLAM complex compared with  $\text{Cu}(\text{OAc})_2$ . In the  $\text{Cu}(\text{II})$ -TOP complex, only one peak is observed at  $-0.61$  V vs SHE that corresponds to the  $\text{Cu}^{2+}/\text{Cu}^0$  reduction. Taking the standard redox potential of Ga ( $E^0_{\text{Ga}^{3+}/\text{Ga}} = -0.53$  V vs SHE) as being representative of the Ga NPs, OLAM contributes towards driving the GRR by complexing Cu and anodically shifting the  $\text{Cu}^{2+}/\text{Cu}^+$  redox potential. We speculate that the first reduction causes changes in the Cu-amine complex that enable the complete reduction to metallic Cu. Instead, TOP inhibits the GRR as it renders the Cu reduction potential more negative than that of Ga.

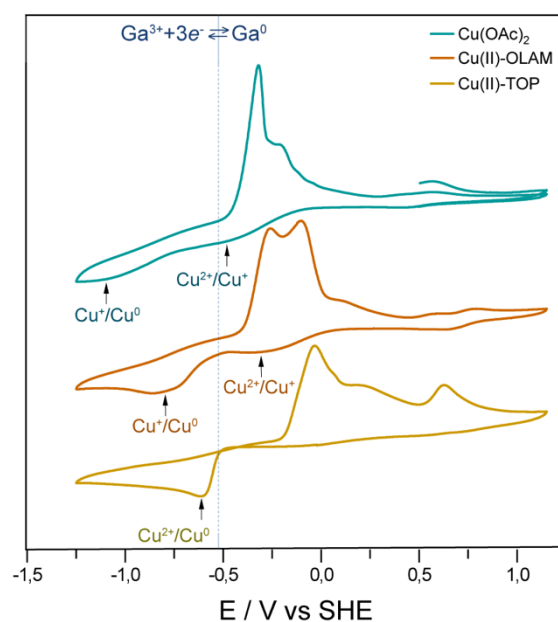


**Figure 3.3.** CVs of  $\text{Cu}(\text{OAc})_2$ ,  $\text{Cu}(\text{II})$ -OLAM and  $\text{Cu}(\text{II})$ -TOP, measured in a MeCN solution of  $0.1$  M  $[\text{NBu}_4][\text{PF}_6]$  as electrolyte. All potentials were referenced against the ferrocenium/ferrocene ( $\text{Fc}^+/\text{Fc} = 0$  V) couple and then converted to the SHE scale. The vertical grey-dotted line corresponds to the  $E^0_{\text{Ga}^{3+}/\text{Ga}}$  vs SHE.

As for OLAC, while it is not essential for the reaction to occur, the TEM images suggest that it plays an important role in the control of the morphology (**Figure A1.4**). FT-IR and NMR measurements confirm its role as a surface ligand (**Figure A1.6**).

Moving towards the investigation of the native oxide shell, **Figure 3.4** provides a summary of its characterization. EDXS analysis evidences the presence of an oxide shell around both the Ga seeds and the dimers (**Figure 3.4a**). Nevertheless, as the samples are exposed to air, albeit only for a few seconds before the holder is inserted into the TEM, the measurement cannot be conclusive alone. Therefore, XAS under inert conditions (details in Chapter 2) was utilized to

elucidate the role of the oxide shell during the galvanic replacement. **Figure 3.4b** displays the Ga K-edge XANES spectra on the aliquots taken at different times during the synthesis of the Cu-Ga NDs. As the reaction proceeds, a clear shift in the absorption edge position towards higher energy together with an increase in the white-line intensity of the acquired spectra is observed. This trend indicates that the initial Ga NPs are mostly in their metallic form, while by the end of the reaction the signal is dominated by the oxide. **Figure 3.4c** reports the results of a linear combination fitting (LCF) analysis (by using Demeter for XAS data processing<sup>220</sup>), that are qualitatively in good agreement with a gradual transition from a metallic to an oxide state. The increasing weight fraction of oxide with time is consistent with the metallic gallium dissolving in solution. As expected, the Cu K-edge XANES spectra show purely metallic Cu in all of the aliquots (**Figure A1.7**). Altogether the XAS data indicate that the gallium oxide shell is always present throughout the formation of the Cu-Ga NDs. A similar conclusion was reached by O'Mullane and collaborators who performed galvanic replacement on bulk Galinstan (GaInSn alloy).<sup>164,174</sup>

Having assessed the role of OLAM as a co-reactant and the presence of the oxide skin throughout the reaction, a mechanistic picture starts to shape up and is sketched in **Figure 3.5**. Migration of gallium atoms occurs through the native oxide shell. By analogy with studies on liquid metal droplets, such migration can happen because of the shell's mechanical fracturing or because of the establishment of a chemical potential gradient.<sup>164,174,177,179,215,221,222</sup> The former is unlikely to be involved in the dimer formation, at least in the initial stages of the reaction, as no external forces are applied, apart from a gentle stirring of the solution. Instead, it is reasonable to assume that the driving force for the gallium migration through the shell is the difference in the reduction potentials of metallic Ga and the copper-amine complex. The fact that gallium atoms must first migrate through the solid oxide shell justifies the very long reaction times needed for the GRR in Cu-Ga compared to those reported for noble metals, which are normally in the range of seconds or minutes.<sup>125,131,134,152,154</sup> As the Ga reaches the surface, its oxidation coupled with the Cu reduction takes place. Because of the oxide shell acting as a separator, alloying does not occur. The formation of a core@shell configuration is unfavorable because of the largely different interatomic distances of copper and amorphous gallium oxide.<sup>188,223</sup> Thus, the Cu nucleates on the seeds because of the lower activation barrier for heterogeneous nucleation, however continued nucleation of copper on the copper nucleus is then energetically more favorable than nucleation on the gallium oxide surface. This behavior is similar to that observed in systems where the metal-metal bonding energy between



atoms of the newly forming domain is higher than the metal-metal bonding energy between the atoms of the new domain and those of the sacrificial template (i.e. Pt on Ag; Cu on Ag, Au, Pt and Pd).<sup>19,140,224</sup>

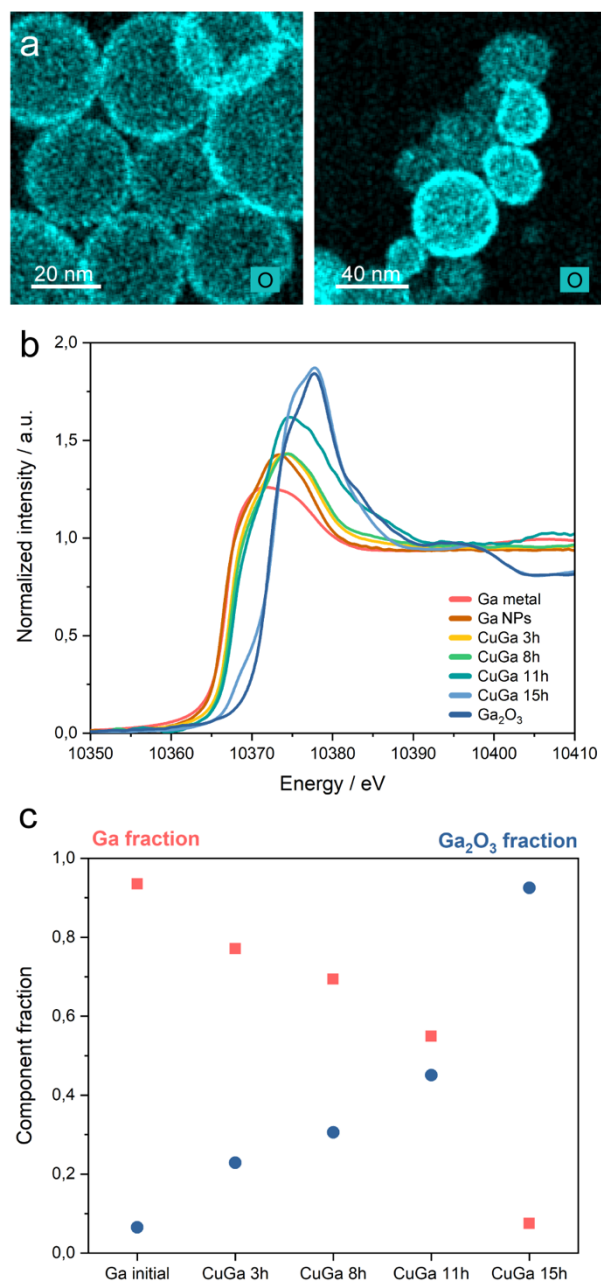


**Figure 3.4.** (a) Oxygen EDXS mapping of the initial Ga NP seeds (left) and of the Cu-Ga NDs (right); (b) Ga K-edge XANES spectra on the aliquots extracted at different reaction times. The references for Ga metal (in red) and Ga<sub>2</sub>O<sub>3</sub> (in blue) are reported; (c) Linear combination fitting (LCF) analysis of the same spectra showing the gradual increasing of the oxidized fraction during the course of the reaction.

As the gallium atoms are consumed in the GRR, one would expect the Ga core to become hollow, as reported for other NPs undergoing GRR.<sup>125,132,134,152</sup> Instead a volume reduction is



observed and a shape deformation follows as the copper domain sizes increases. In the context of reconfigurable and self-healing electronics, significant efforts are ongoing to study the connection between Ga-based liquid-metal contacts and solid metals, with a prototypical interface being GaIn/Cu.<sup>177,192,215,222,225–229</sup> Here, the non-Newtonian rheological properties of the gallium oxide skin have been demonstrated to play a significant role as they can mechanically stabilize the liquid core into non-spherical, metastable shapes.<sup>177,192,215,222,225–229</sup> Furthermore, the oxide interfacial adhesion mechanics when in contact with rigid flat substrates have been shown to cause deformation of the initially spherical liquid metal droplets.<sup>177,192,215,222,225–230</sup> Similar phenomena might be involved in the formation of the mushroom-like Cu-Ga NDs. The increasing deformation of the gallium domain as the copper domain increases in size can be attributed to interfacial adhesion mechanics as well as strain due to the difference in the interatomic distances between the copper and the gallium oxide. The absence of voids in the core and observed reduction in volume of the Ga domain can be explained by the following: the liquid nature of Ga allows the atoms within the oxide skin to redistribute, whilst the oxide skin can adapt to the shrinking volume thanks to its viscoelastic properties.

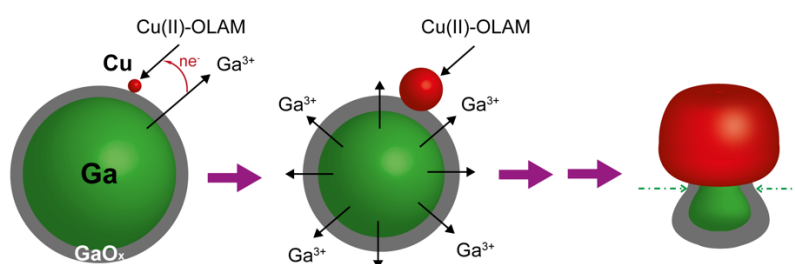


**Figure 3.5.** Schematic representation of the proposed formation mechanism of the Cu-Ga NDs.

To prove the importance of the oxide skin and liquid nature of gallium in regulating its chemical reactivity at the nanoscale, we extended the same reaction scheme to other systems (**Figure 3.6**). First of all, we substituted Cu with Ag, a metal with a more positive reduction potential than Cu ( $E^0_{Ag^+/Ag} = +0.80$  V vs SHE<sup>173</sup> and  $E^0_{Cu^{2+}/Cu} = +0.34$  V vs SHE). Here, the larger potential difference versus Ga makes the modulation of redox properties via the coordination environment of the cation unnecessary, so OLAM was not needed. **Figure 3.6a** evidences that upon reaction with  $AgNO_3$ , the Ga seeds are decorated by multiple Ag domains. The more similar interatomic distances between Ag and gallium oxide might be one reason for the formation of these multimeric NPs instead of dimers.<sup>231</sup> Importantly, this result confirms that

the final morphology of the bimetallic NPs is related to the native oxide and the liquid nature of the Ga seeds and not to the presence of OLAM as a co-reactant.

Secondly, we substituted the Ga NPs with In NPs (**Figure A1.8**) as the sacrificial templates during the reaction with Cu. In is another main-group metal with a low melting point (156.6°C for bulk), however, it is less oxophilic compared to Ga, meaning that the native oxide shell is not present in the as-synthesized NPs.<sup>41,195,232</sup> The standard redox potentials of In and Cu ( $E^0_{\text{In}^{3+}/\text{In}} = -0.34 \text{ V vs SHE}^{173}$  and  $E^0_{\text{Cu}^{2+}/\text{Cu}} = +0.34 \text{ V vs SHE}$ ) are suitable for galvanic replacement. **Figure 3.6b** shows that bimetallic Cu-In NPs do indeed form. However, here the two metals are mixed, as expected based on the Cu-In phased diagram<sup>233</sup>, rather than segregated as in the Cu-Ga NDs. Furthermore, the reaction takes only 15 minutes, which is more reminiscent of a traditional GRR with a metal NP lacking an oxide shell. Overall, these results with In NPs are consistent with the hypothesized role played by the native gallium oxide shell in preventing alloying and in determining the final ND morphology. As a side note, our attempts to remove the amphoteric oxide shell in the Ga NPs or to tune its thickness by acid or base treatments were unsuccessful so far.

Finally, we wanted to explore the possibility of performing sequential GRR reactions on the Ga NPs in order to eventually increase the complexity of Ga-based multimetallic NPs. **Figures 3.6c,d** show that Ag-Cu-Ga trimers could be synthesized using Cu-Ga NDs as templates. Here future in-depth characterization and additional experiments will be pursued to understand the delicate interplay between the redox potentials of the three metals, their surface energies and interface energies in determining this final configuration as at the moment it is unclear on which domain nucleation occurs.

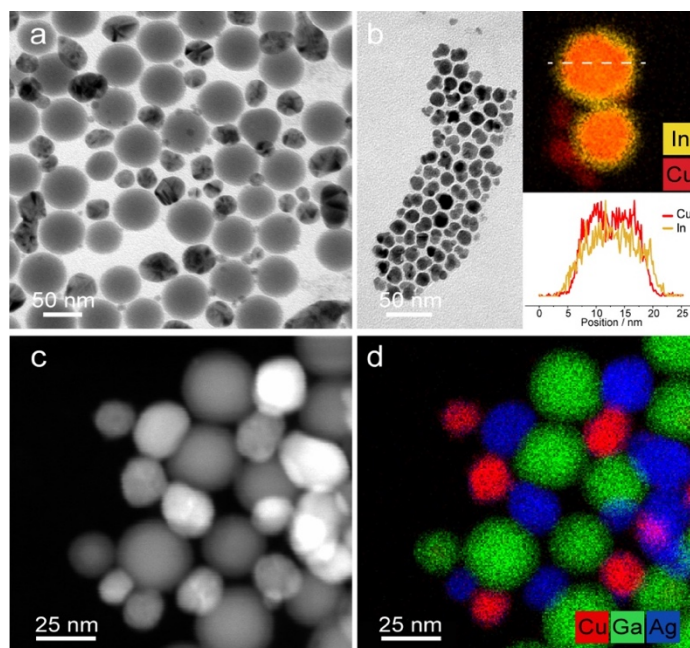


**Figure 3.6.** (a) TEM images of the Ag-Ga NPs obtained by reacting Ga NPs with  $\text{AgNO}_3$ ; (b) TEM image (left) and EDXS elemental analysis with corresponding line scan (right) of the Cu-In NPs obtained by reacting In NPs with  $\text{Cu}(\text{OAc})_2$  for only 15 minutes, otherwise the same conditions for the Cu-Ga NDs were utilized; (c,d) HAADF STEM image and EDXS elemental map of the Ag-Cu-Ga nanotrimers obtained by sequentially reacting Ga NPs with  $\text{Cu}(\text{OAc})_2$  and  $\text{AgNO}_3$ .

### 3.3. Conclusions

In conclusion, in this Chapter we have explored the reactivity of liquid-metal Ga NPs to synthesize bimetallic Cu-Ga NPs via a colloidal chemistry approach. Investigation of the formation pathway has revealed that a GRR takes place, which is consistent with the redox properties of metallic Ga and the Cu-amine complex forming in solution. The combination of different characterization techniques and control experiments has highlighted the key role played by the native oxide shell and liquid nature of the Ga NPs in determining the final nanodimer morphology of the bimetallics. Having learned this, the same approach has been applied to access bimetallic Ag-Ga and ternary Ag-Cu-Ga NPs.

Overall, this first study on colloidal liquid metal NPs as sacrificial templates in GRRs showcases the very intriguing and peculiar reactivity of this class of materials at the nanoscale that is certainly underexplored to date. Furthermore, it opens the way towards achieving much more sophisticated and complex structures of Ga-based nanomaterials, which possess promising properties for top-scientific challenges including  $\text{CO}_2$  electroreduction, sensing, plasmonics, and self-healing electronics.<sup>21,22,203</sup>

## Chapter 4

### Modulating the reactivity of liquid Ga nanoparticles by modifying their surface chemistry

The content of this chapter is based on the published work: *J. Am. Chem. Soc.* **2022**, 144, 4, 1993–2001. <https://doi.org/10.1021/jacs.1c12880>

**Abstract:** “Micron- and nano-sized particles of liquid metals, particularly Ga-based alloys, are attracting increasing attention for applications in several fields. Their native oxide skin regulates many of their properties; yet, very little is known about its chemistry. Here, we investigate the impact of selected capping ligands on the native oxide thickness of Ga NPs and on their chemical reactivity, choosing the GRR as one example. We demonstrate that amines and carboxylic acids promote thicker oxide shells while thiols and phosphines hinder the oxide growth. Upon pondering thermodynamics and kinetics factors, we conclude the affinity of the anchoring group towards the metal core being the major driver. We go on to prove that thicker shells foster the formation of Cu-Ga NDs following the reaction of the Ga NPs with a copper amine complex. In contrast, thinner oxides lead to the homogeneous nucleation of individual Cu NPs. This study reveals the importance of the choice of ligand when studying Ga-based metal NPs for different applications since both their surface chemistry and reactivity are largely affected by this decision.”

**Authors:** Laia Castilla-Amorós, Tzu-Chin Chang Chien, James R. Pankhurst, Raffaella Buonsanti

**Contribution:** Experiments design, partly synthesized the NPs, performed all the electron microscopy and ICP characterization and analyzed the resulting data, participated in the XPS experiments and discussion, wrote the manuscript with contributions from all authors.

## 4.1. Introduction

LMs are a class of materials that is attracting a renewed interest thanks to their fascinating properties arising from their simultaneous metallic and liquid nature.<sup>177–179</sup> Among all possible compositions, most research focuses on metallic Ga and its alloys because of their low melting temperatures and their unique electrical and rheological characteristics.<sup>176</sup> The latter open up new possibilities in various fields, including electronics, microfluidics, biomedicine, batteries, as well as for synthetic and catalytic applications.<sup>180,182–186,188,191,234,235</sup>

So far, most of the work has centered on bulk and micron-sized particles. Nevertheless, new physicochemical properties emerge when the size of Ga-based particles shrinks down to the nanoscale.<sup>179</sup> For example, plasmonic and catalytic properties can be modulated with the size of the particles and are influenced by their size-dependent solid-liquid transition.<sup>188,191,200</sup>

In addition to the chemical composition of the bulk, the native oxide skin of Ga-based particles plays a crucial role in determining their chemical and mechanical behavior.<sup>176,236,237</sup> For instance, the thickness of the surface oxide can modify surface adhesion and wetting properties<sup>192,193,238</sup> as well as tuning the on/off state in soft electronics<sup>214,222,239</sup>. As an additional example, it has been recently discovered that a smooth oxide skin can stabilize LM particles in their undercooled state.<sup>240</sup> As NPs show larger surface to volume ratios and higher surface energies, they tend to oxidize faster than their bulk counterparts<sup>194</sup> or even have thicker shells when going down in size.<sup>195</sup> Therefore it is of outmost interest to study the properties of Ga native oxide skin at the nanoscale for the use of NPs in all the aforementioned applications.

In order to accurately and systematically study the nanoscale and surface properties of NPs, homogeneous samples are needed. Nevertheless, synthetic routes to fabricate Ga NPs with high enough monodispersity are limited to physical deposition<sup>241,242</sup> and thermal decomposition<sup>41,188</sup> techniques. Among those, the latter enables the synthesis of colloidally stable NPs with the highest monodispersity (7–8 %) by decomposing molecular precursors in the presence of surfactants, whose role is to both control the synthesis and stabilize the formed NPs in solution. Interestingly, molecular coatings, of the same nature as the aforementioned surfactants, have been shown to significantly impact the surface properties of Ga-based particles, particularly the thickness and roughness of their oxide skin.<sup>240,243–245</sup> However, these studies still remain isolated examples carried out with polydisperse samples and the relationship between the

chemical nature of the molecules and their role as surface modifiers has not been thoroughly investigated so far.

Herein, we investigate whether capping ligands with different anchoring groups not only stabilize Ga NPs in solution but also have an impact on their surface properties. The oxide skin for most of the Ga-based LM alloys, including galinstan ( $\text{Ga}_{68.5}\text{In}_{21.5}\text{Sn}_{10}$ ), eutectic GaIn and GaPd droplets, is essentially gallium oxide, which is due to its higher absolute Gibbs free energy of formation compared to the oxides of other elements.<sup>179,227,236,246,247</sup> Hence, pure Ga is an ideal choice to study the generality of the surface properties of these materials. Furthermore, ligand effects observed at the bulk and the micron scales are expected to be even greater at the nanoscale, where the surface-to-volume ratio increases, which justifies the choice of using NPs as our model system. We combine TEM, elemental analysis and XPS to study the Ga oxide skin in the presence of carboxylic acid, amine, thiol and phosphine ligands. We then correlate the chemical nature of the capping ligands to the skin thickness, taking into account both thermodynamic and kinetic factors. Going one step further, we also investigate how the oxide thickness of the LM NPs modulates their chemical reactivity, taking the GRR with a molecular copper precursor developed in Chapter 3 as one example.

## 4.2. Results and discussion

Colloidal Ga NPs were synthesized by adapting a previously reported procedure (**Figure A2.1**).<sup>188</sup> Four different ligands were utilized during the synthesis, specifically oleic acid (OLAC), oleylamine (OLAM), tri-n-octylphosphine (TOP) and dodecanethiol (DDT). These ligands were selected because of the different affinities of their anchoring groups towards metal surfaces. In particular, OLAC and OLAM are known to bind to oxide surfaces more strongly than metallic surfaces, therefore they should stabilize the oxide skin of LM NPs.<sup>243,244,248–251</sup> Conversely, DDT and TOP have a higher affinity to metals, thus they are expected to stabilize the metal core and inhibit the oxide formation.<sup>243,244,248–251</sup> Furthermore, these ligands are all readily available and commonly used in NP synthesis.

**Figure 4.1** gives an overview of the characterization of the as-synthesized samples. In the TEM images (**Figure 4.1a**), the lack of diffraction contrast, which would denote crystallinity, indicates that all the NPs are amorphous, i.e., liquid, which is consistent with previous

reports.<sup>42,188</sup> The size distribution analysis evidences that the different ligands have no major effect on the morphology and final size of the Ga NPs, which are all spherical with a mean size of around 30 nm (**Figure A2.2**). Indeed, the ligands were intentionally added to the reaction flask after the NP formation (**Figure A2.1**) to minimize their impact on the nucleation and growth steps, and thus on size and shape. XPS (**Figure 4.1b**) evidences that -COOH, -N, -P and -S are on the NP surface, consistent with OLAC, OLAM, TOP and DDT being the capping agents, respectively.

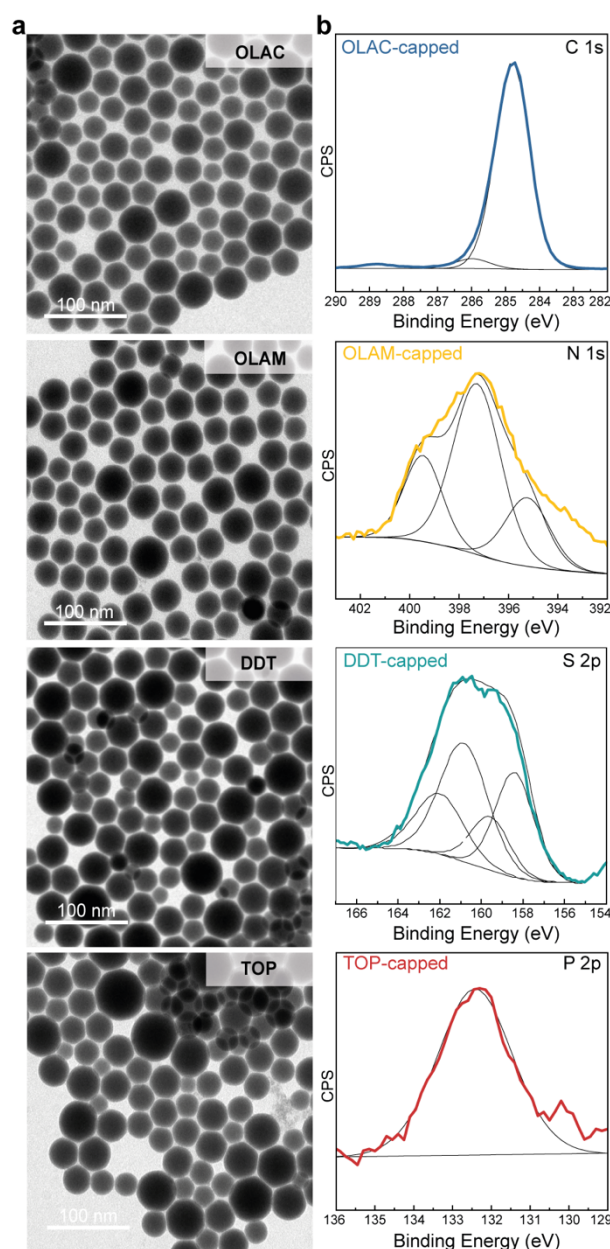


**Figure 4.1.** (a) TEM images of the as-synthesized Ga NPs with different ligands; (b) XPS spectra for -C, -N, -P and -S indicating the presence of the ligands on the surface. The peak at 288.72 eV in the C1s spectrum for the OLAC-capped sample is assigned to carboxylic carbon (COOH).



To gain insight into the effect of the different capping agents on the oxide skin, we used XPS complemented with electron microscopy techniques. The samples were characterized just after their synthesis and particular care was taken to minimize the time the samples were exposed to air during the transfer from the glove box to the instrument. **Figure 4.2** reports a summary of the obtained results. The complete data set is reported in the Appendix 2 (**Figure A2.3**) and a detailed explanation on the oxide thickness interpretation is reported in Chapter 2 (**Figure 2.1**).

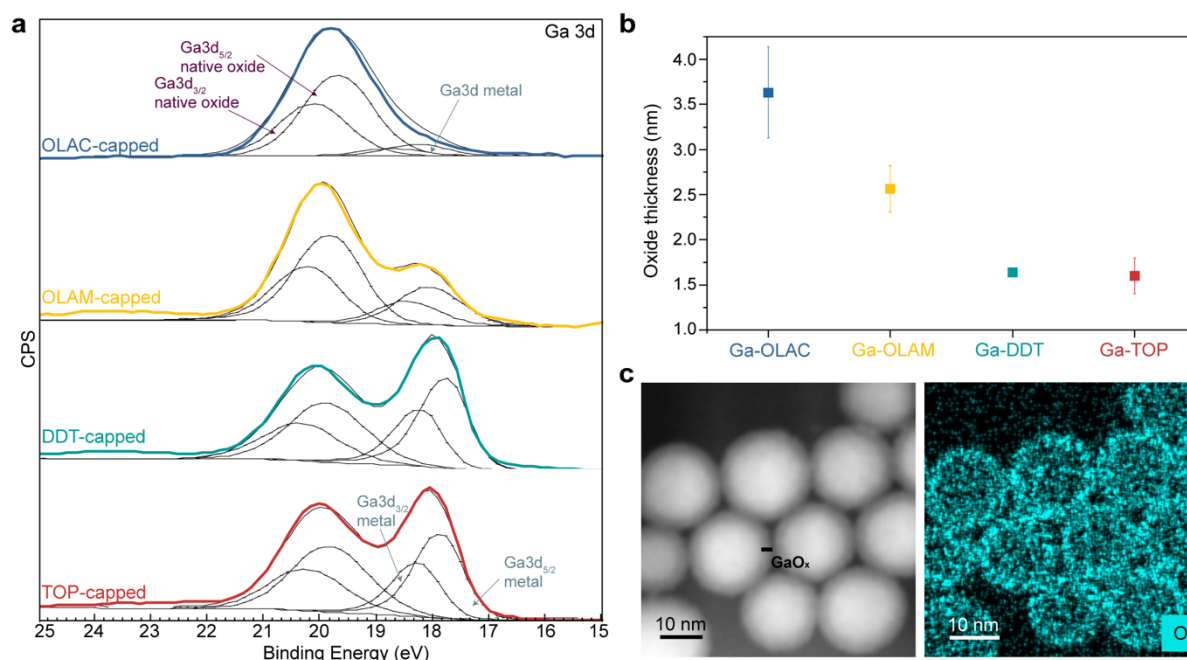


**Figure 4.2.** (a) XPS spectra of the Ga 3d region for the as-synthesized ligand-capped NPs, evidencing the simultaneous presence of Ga metal and Ga oxide with different ratios in each case; (b) oxide thickness, with corresponding error bars, calculated from the XPS data for the different ligands (note that the error bar for DDT is too small to be seen); (c) STEM-HAADF image (left) and corresponding EDXS elemental map (right) of OLAM-capped Ga NPs showing the presence of an oxide shell as a lighter contrast (left) and in blue (right). The measured oxide thickness on the STEM-HAADF image corresponds to 2.6 nm, matching well with the XPS calculation reported in (b).

Similarly to other reports,<sup>243,244,252</sup> the XPS spectra were fitted with two peaks in the Ga 3d region for each sample (**Figure 4.2a**). The peak at around 20 eV corresponds to gallium oxide whereas the peak at around 18 eV can be assigned to metallic Ga. The relative ratio of these two peaks changes across the samples indicating differences in the oxide-to-metal contribution. The thickness of the oxide, which can be approximated from this ratio, decreases from around 3.5 nm to 1.5 nm following the trend OLAC>OLAM>DDT~TOP (**Figure 4.2b**). High-angle annular dark-field scanning TEM (HAADF-STEM) imaging and energy dispersive X-ray spectroscopy (EDXS) corroborate the thickness of around 2.6 nm for the OLAM-capped NPs



(**Figure 4.2c**). This correlation between XPS and HAADF-STEM EDXS was also observed for OLAC-, DDT- and TOP- capped Ga NPs (**Figure A2.4**). Therefore, we can confidently compare the extent of the oxidation between the four samples: OLAC-capped particles have the thickest oxide shell followed by OLAM-, DDT- and TOP-capped Ga NPs, with the latter two being approximately equal.

To understand the observed trend, we investigated the oxide evolution over time. Our aim was to elucidate the interplay between kinetics (i.e., delayed oxidation) and thermodynamics (i.e., thinner final oxide thicknesses under equilibrium conditions). To reach the equilibrium conditions, we left samples deposited as thin films exposed to air for five days. No further changes were observed in samples left for over one month under the same conditions. **Figure 4.3** summarizes the obtained data. The XPS spectra of the samples can still be deconvoluted into the gallium oxide and metallic Ga peaks, although the contribution of the former increases compared to the as-synthesized samples (**Figure 4.3a**). This trend becomes more evident when plotting the oxide thicknesses for the ligand-functionalized Ga NPs (**Figure 4.3b**). When compared to the measurement on day zero, OLAC ended up with the thickest shell, which decreased with OLAM>DDT>TOP, with the latter clearly presenting the thinnest shell (**Figures 4.3b,c**).

In parallel, we synthesized Ga NPs in the total absence of ligands. Interestingly, their oxide shell was even thinner than for TOP-capped Ga NPs at both day 0 and day 5 (**Figure A2.5a** and **Figure A2.6**). These results are in opposition of what had been previously reported in the literature in where adding capping ligands resulted in thinner oxide shells than with bare surfaces.<sup>244</sup> This difference could be arising from various factors: the smaller size of our NPs compared to the cited example, the higher polydispersity of the Ga NPs without ligands (**Figure A2.5b**) and/or the presence of numerous large Ga blobs (with one example in **Figure A2.5c**). Unfortunately, while possibly being an interesting comparison point, the polydispersity of the sample makes it not suitable for a study that aims for an accurate and systematic description of nanoscale surface properties such as this one. Besides, the NPs became colloiddally unstable just after few minutes of their synthesis (**Figure A2.5d**), preventing any further manipulation.

The observation that the NPs do not become fully oxidized and preserve a metallic core even when exposed to air for several days is consistent with the self-passivating nature of the gallium oxide skin. This behavior can be interpreted via the well-established Cabrera-Mott

theory.<sup>194,221,253</sup> According to this theory, oxygen chemisorption quickly initiates the formation of a monolayer of gallium oxide. However, electrons can still pass from the core through the oxide and ionize adsorbed  $O_2$ .<sup>244</sup> The formation of negatively charged oxygen ions on the surface and positively charged metal ions in the core generates an electric field (the Mott potential,  $V_M$ ), which drives the oxide formation. If the diffusion coefficient of the metal ions through the oxide layer is larger than that of the oxygen ions, then voids in the metal core form (Kirkendall effect).<sup>254,255</sup> In the case of Ga, the oxide growth rate follows a logarithmic trend and ends when a critical thickness is reached, generally up to a few weeks.<sup>189,195,243,256</sup> This passivating effect of the oxide layer prevents the metal from further oxidation. In the case of NPs, the higher surface-to-volume ratio is expected to accelerate the oxide growth compared to bulk materials.<sup>253</sup> Indeed, we found that samples stored in solution and under inert atmosphere for five days possessed a very similar oxide thickness to the samples exposed to air (**Figure A2.7**). This observation demonstrates that the oxidation rate is relatively fast even with extremely low concentrations of adventitious oxygen.

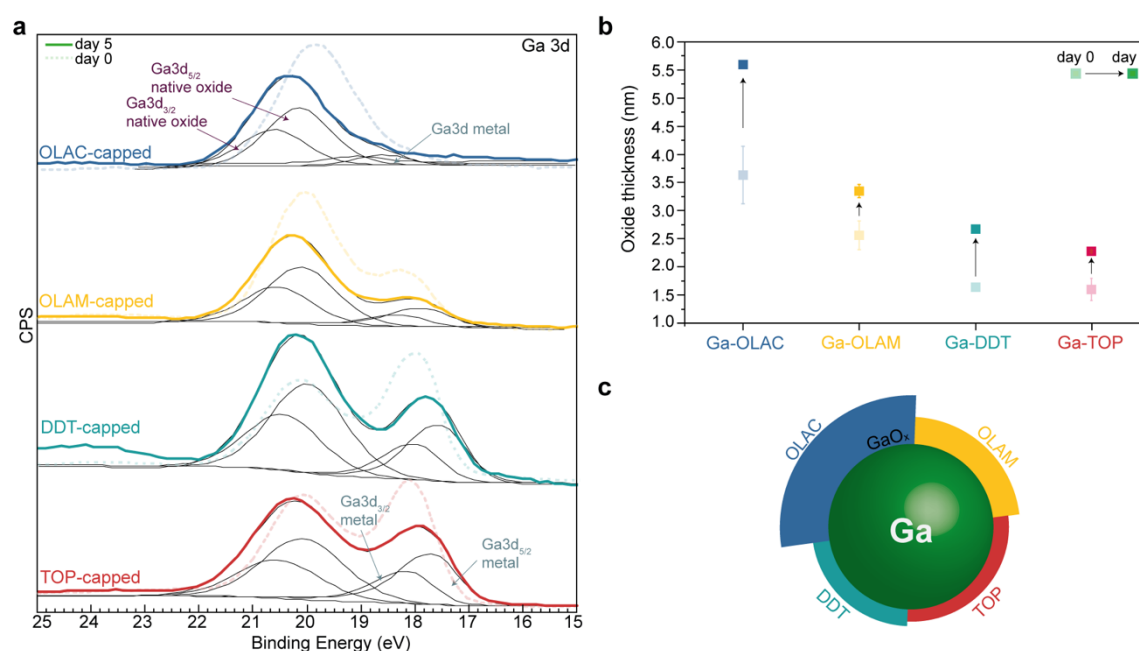


**Figure 4.3.** (a) XPS spectra of the Ga 3d region for the ligand-capped NPs that were aged for 5 days in air; the as-synthesized Ga NP spectra are also shown as a reference (dashed); (b) oxide thicknesses with corresponding error bars for the “aged” ligand-capped Ga NPs. Note that no error could be calculated for the aged OLAC-capped sample because no signal for Ga metal could be found in the Ga 2p spectra (**Figure A2.7a**) and that the errors for TOP and DDT are too small to be seen; (c) sketch representing the oxide thickness for each ligand.

To understand the changing influence of the ligands on the oxide thickness with time, different factors must be considered. We assume that a combination of thermodynamics and kinetics

dominate at day 0 while thermodynamics will be more important at day 5 and after that. From a thermodynamic point of view, the aforementioned ligand's binding preference towards the metal or the metal oxide is certainly an important parameter.<sup>248–251,257</sup> However, the ligand's dipole moment and subsequent effect on the  $V_M$  should also be considered.<sup>243,258–261</sup> From a purely kinetic perspective, the packing density on the surface should be taken into account as it can alter the oxygen accessibility to surface sites.<sup>243–245,262,263</sup>

To comprehend the observed trends, let us discuss each group separately starting with OLAC and OLAM. Hens et al. have previously empirically demonstrated that both amines and carboxylic acids (in the form of carboxylates), bind to Cu NPs through surface oxide sites.<sup>248</sup> Both ligands have the same alkyl chain and only differ in their functional group. Hence, it is reasonable to think that they would pack similarly on the surface of Ga NPs without imparting big differences on the availability of surface sites, i.e., kinetics, for the oxide growth. On the other hand, according to the HSAB theory, carboxylates are harder bases than amines and thus have a higher affinity toward hard acids, like  $Ga^{3+}$ .<sup>250,257</sup> Therefore, OLAC simultaneously favors the outgoing diffusion of  $Ga^{3+}$  ions during the oxide formation and passivates the oxide better, eventually promoting the formation of a thicker shell than OLAM.

The comparison between TOP and DDT is less straightforward since both their alkyl chains and functional groups are different (we note that these ligands are not commercially available or even stable with the same chain length and their synthesis is not trivial). Thiols and phosphines are soft bases with greater affinity towards soft acids, which explains why they are suitable ligands if one wants to hinder the oxidation of Ga NPs. Phosphines are softer bases than thiols and, as a result, have an even stronger affinity for metal sites.

In addition to the HSAB theory, TOP has a larger electric dipole moment ( $>>1.2$  D) than DDT ( $\sim 0.8$  D) and so it is expected to oppose the  $V_M$  to a greater extent, ultimately reducing the final oxide thickness. Overall, thermodynamics point towards a thicker oxide shell for DDT than for TOP, which is indeed what we observe after 5 days (**Figure 4.4**).

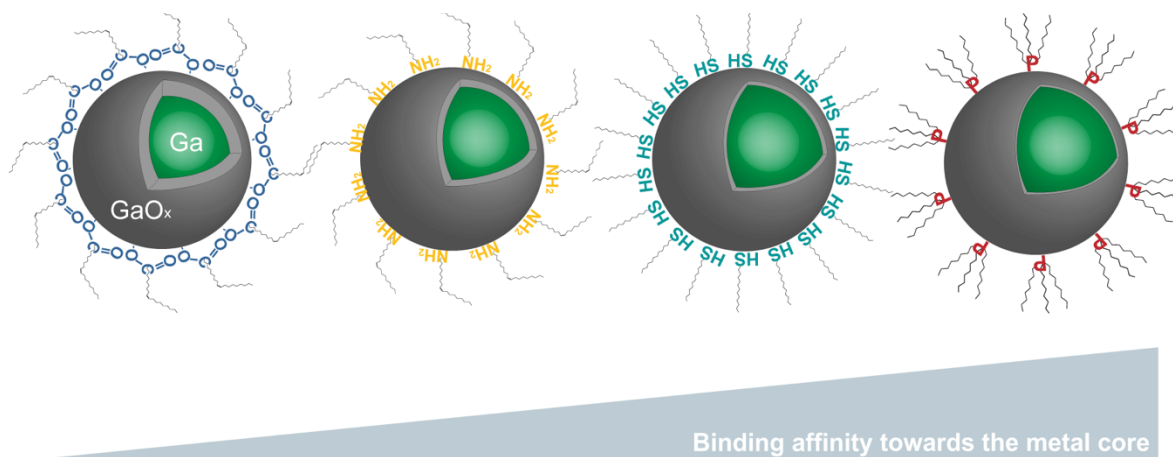


**Figure 4.4.** Schematic representation illustrating how different ligands affect the native gallium oxide shell thickness and the main parameter governing thermodynamic oxide tunability using ligands.

On the other hand, DDT's saturated single carbon chain is prone to create dense self-assembled monolayers (SAMs) on metallic NP surfaces.<sup>243–245,251,264,265</sup> In contrast, the bulkier TOP ligand will form a less compact SAM, which results in less impediment of the oxygen diffusion towards the Ga surface. Nevertheless, DDT-capped and TOP-capped Ga NPs display similar oxide thickness at day 0. Only the combination of the opposing thermodynamics and kinetics effect can justify this result. A similar argument was used by Tabor et al. when comparing the effect of thiols with different substitution and dipole moments on the oxide growth of a mixture of nano- and micron-sized eutectic GaIn particles.<sup>243</sup>

Having assessed the impact that these different ligands have on the oxidation of colloidal Ga NPs, we decided to investigate its effect on their chemical reactivity. The self-passivating oxide shell is known to impact the chemical and mechanical behavior of liquid metals.<sup>2-4,16,18,31,43–48</sup> Indeed, the oxide shell was recently discovered to strongly influence the behavior of Ga NPs in the galvanic replacement reaction (GRR).<sup>42</sup> In particular, OLAC-capped Ga NPs were found to react with a copper amine complex to form Cu-Ga nanodimers.<sup>42</sup> The reaction mechanism was studied by several techniques, including TEM characterization of the reaction process at different times. The unexpected morphology was explained by the presence of the oxide shell preventing the Cu-Ga alloying. Therefore, we explored the same reaction with OLAM-, DDT- and TOP-capped Ga NPs, possessing decreasing oxide thicknesses, and using the OLAC-capped NPs as a reference control.

**Figure 4.5** summarizes the obtained results. Interestingly, we can separate the products into two categories according to their morphologies (**Figure 4.5a** and **Figure 4.5b**). The OLAC-

and OLAM-capped Ga NPs form Cu-Ga nanodimers, similarly to previous results.<sup>42</sup> Indeed, the bright-field TEM images (**Figures 4.5c,d**) indicate that the lower contrast Ga domain possesses a smaller size than the starting NPs, as well as a deformed shape (**Table A2.1**), which narrows towards the interface with the crystalline Cu domain. Conversely, homogeneous nucleation of crystalline Cu NPs, separated from the amorphous Ga domains, is observed with the TOP- and DDT-capped Ga NPs (**Figures 4.5e,f**).

These differences are even more evident in the STEM-HAADF and EDX images (**Figures 4.5g,h** and **4.5i,j**). The white arrow in **Figure 4.5g** points to the presence of a lower contrast interface between the Cu and the Ga domains, which corresponds to the gallium oxide shell. As described in the previously cited work,<sup>42</sup> this interface causes the deformation of the Ga domain. On the other hand, **Figures 4.5i,j** shows that Ga and Cu NPs are physically mixed and do not share an interface.

These results suggest that the oxide thickness determines in what fashion the GRR proceeds. GRRs are electrochemical processes in which a sacrificial metal (in our case Ga<sup>0</sup> in the NP core) is oxidized by a metal cation in solution possessing a more positive redox potential (in our case Cu<sup>2+</sup>) that, in turn, gets reduced and deposits onto the pre-existing template.<sup>42,125,127,132,134,139,152,174</sup> Examples in the literature indicate that capping ligands can influence the progress of GRRs by modifying the surface properties or acting as co-reducing agents.<sup>127,151,153</sup> Therefore, to be conclusive regarding the role of the oxide, we performed a series of control experiments which will be developed in the following lines. First, we carried out a ligand exchange between OLAC-capped Ga NPs and OLAM, DDT and TOP after the oxide shell had already formed. By doing so, we expected to maintain a thick gallium oxide shell that was independent of the capping ligand, hence keeping one of the parameters of study constant (see Chapter 2 and **Figures A2.8-A2.10**). After each GRR, Cu-Ga nanodimers formed independently of the capping ligand (**Figure A2.9**). Secondly, when adding to the copper amine complex solution an excess of DDT and TOP in the absence of Ga NPs, no Cu NPs formed under the same conditions. Lastly, DDT-capped Ga NPs grow an oxide shell after 5 days that is equivalent in thickness to that of fresh OLAM-capped NPs (**Figure 4.3c**). We then repeated the GRR with the copper amine precursor and, as expected, Cu-Ga nanodimers were obtained after both the same and longer reaction times (**Figure A2.11**). Thus, we can establish that the heterogeneous versus homogeneous nucleation of Cu solely depends on the gallium oxide thickness of the Ga NPs which, in turn, depends on the initial ligands capping their surface.

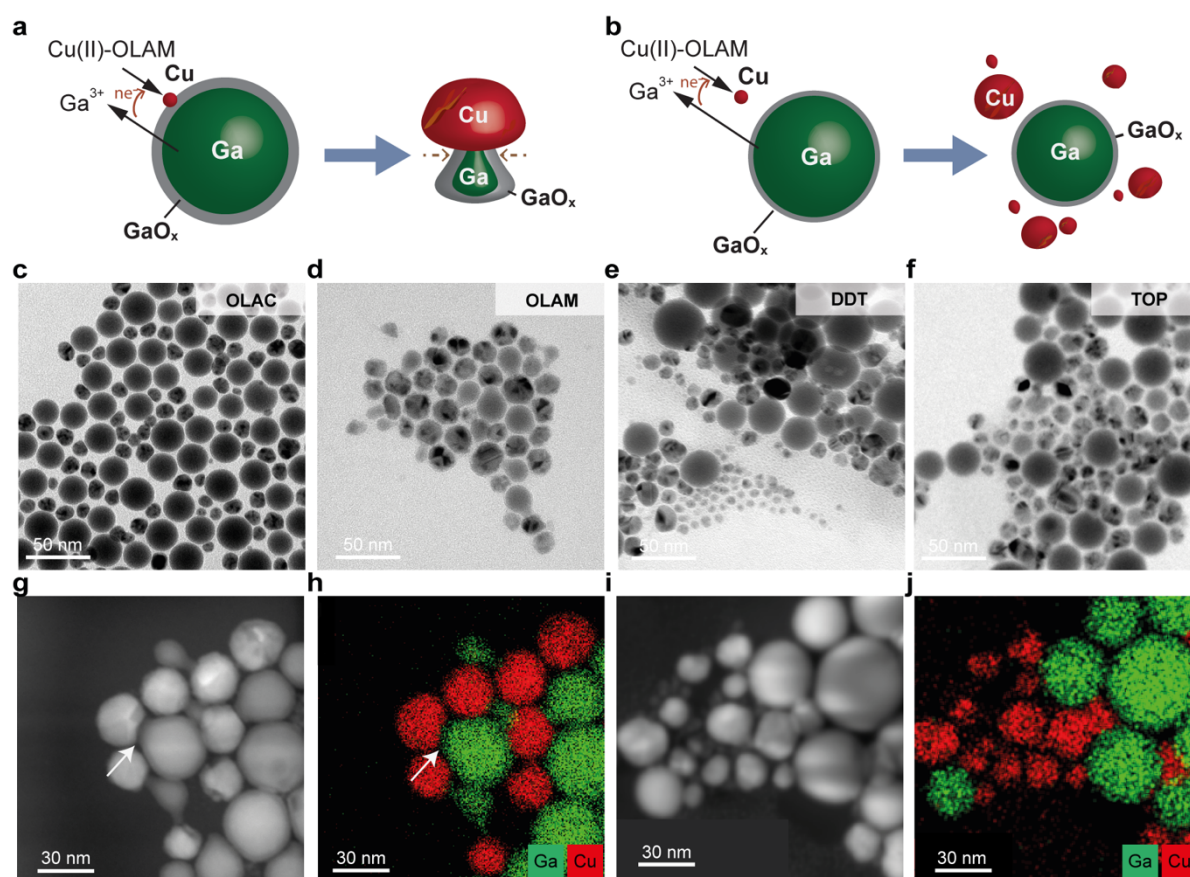


**Figure 4.5.** Sketch of the proposed reaction mechanism for (a) OLAC- and OLAM- and (b) for DDT- and TOP-capped Ga NPs with the Cu precursor; TEM images of the resulting NPs after GRR with (c) OLAC- and (d) OLAM-capped Ga NPs show the formation of Cu-Ga nanodimers, as confirmed by (g) STEM-HAADF and (h) EDX of the OLAM-capped samples; on the other hand, when (e) DDT and (f) TOP are used, the GRR results in separate Cu and Ga NPs as evidenced by their corresponding TEM images and (i) STEM-HAADF and (j) EDX of the DDT-capped samples.

Having confidently concluded that the oxide shell thickness determines the outcome of the GRR, qualitative information on the reaction rate can be derived from the analysis of the size evolution of the Ga and Cu domains along with the relative concentration between the two metals in the final reaction product (**Table A2.1**). These data indicate that OLAM-capped Ga NPs undergo a faster GRR than OLAC-capped ones, which is consistent with a thinner oxide shell facilitating the migration of Ga atoms from the NP core into the solution. In the case of the TOP- and DDT-capped Ga NPs, the size and elemental analyses indicate that a GRR still takes place, though at a lower extent than expected based on a thinner oxide shell. This puzzling result prompts a final question: why does the thinner oxide shell in DDT- and TOP-capped Ga NPs not facilitate the outward diffusion of Ga and promote a separate nucleation of Cu? First of all, we note that the amorphous Ga oxide skin possesses a very complex layered structure that makes it unique compared to other oxides, like alumina.<sup>236,267</sup> We hypothesize that this

feature prevents the transport of copper atoms and, thus, their alloying with gallium. Moreover, thicker oxide shells are expected to have a higher degree of short range structural order.<sup>256,268–271</sup> The latter can reduce the nucleation energy barrier of a new crystalline phase, in this case copper. Conversely, a thinner oxide would show a more liquid-like behavior<sup>192,228</sup> that eventually prevents heterogeneous nucleation of an ordered phase. Since homogeneous nucleation is energetically more expensive, Cu nucleation, and hence Ga outwards diffusion, would occur at a slower rate than if heterogeneous nucleation took place under the same conditions. Here, future in-depth characterization, including high resolution microscopy and pair distribution function analysis, will be pursued to verify these hypotheses and to further comprehend the complex structure and properties of gallium oxide on Ga NPs.

### 4.3. Conclusions

In conclusion, we have demonstrated the modulating effect of capping ligands on the surface oxidation of liquid Ga NPs and the importance of the oxide shell thickness on the reactivity of Ga NPs in the framework of the GRR. A thorough analysis of the surface of these Ga NPs has revealed that DDT and TOP are the most suitable ligands if the aim is to hinder the gallium oxide growth. On the other hand, OLAM and, in particular, OLAC are less efficient in moderating the oxidation of the Ga surface. Nevertheless, none of the ligands were able to completely suppress the oxidation of Ga even when working under inert conditions.

Through a number of systematic experiments, we have evidenced how the oxide thickness governs the nucleation fashion of a Cu precursor during a GRR with Ga. Thicker oxide shells promote the heterogeneous nucleation of Cu to form Cu-Ga nanodimers; contrariwise, thinner shells lead to a separated nucleation of Cu particles.

Overall, we showcase the importance of ligands when studying Ga NPs as well as the unique behavior of these nanomaterials and the need for further exploration of their chemistry. We also highlight that in all Ga-based LM alloys, the oxide skin still consists of gallium oxide, therefore these findings are expected to be of interest to a wider community.

Given the increasing number of original publications and reviews<sup>176,177,179,189,214,227,236,272</sup> on the applications and fundamentals of Ga-based micro- and nano-particles, this work aims to serve as a reference for future studies in several disciplines.



## Chapter 5

### Tailoring morphology and elemental distribution of CuIn nanoparticles via galvanic replacement

The content of this chapter is based on submitted work.

**Abstract:** *“The compositional and structural diversity of bimetallic NPs provides a superior tunability of their physico-chemical properties, making them attractive for a variety of applications, including sensing and catalysis. Nevertheless, the manipulation of the properties-determining features of bimetallic NPs still remains a challenge, especially when moving away from noble metals. In this work, we explore the GRR of In NPs and a copper molecular precursor to obtain Cu-In bimetallic NPs with an unprecedented variety of morphologies and elemental distributions. We obtain spherical  $\text{Cu}_{11}\text{In}_9$  intermetallic and patchy phase-segregated Cu-In NPs, as well as dimer-like Cu- $\text{Cu}_{11}\text{In}_9$  and Cu-In NPs. In particular, we find that segregation of the two metals occurs as the GRR progresses with time or with higher copper precursor concentration. We discover size-dependent reaction kinetics, with the smaller In NPs undergoing a slower transition across the different Cu-In configurations. We compare the obtained results with the bulk Cu-In phase diagram and, interestingly, find that the bigger In NPs stabilize the bulk-like Cu- $\text{Cu}_{11}\text{In}_9$  configuration before their complete segregation into Cu-In NPs. We demonstrate that GRRs are a powerful synthetic approach beyond noble metal-containing bimetallic structures, yet that the current knowledge on this reaction is challenged when oxophilic and poorly miscible metal pairs are used.”*

**Authors:** **Laia Castilla-Amorós**, Pascal Schouwink<sup>+</sup>, Emad Oveisi<sup>+</sup>, Raffaella Buonsanti

+ indicates equal contribution

**Contribution:** Experiments design, synthesized the NPs, performed the TEM, STEM (not atomic resolution) and ICP characterization and analyzed the resulting data, participated in the atomic resolution STEM and GIXRD experiments and discussion, wrote the manuscript with contributions from all authors.

## 5.1. Introduction

Bimetallic NPs possess a wide tunability of their physico-chemical properties which arise from synergistic effects between the two metals altering their electronic structures.<sup>19,35,40,273–284</sup> Such tunability makes them more appealing than monometallic NPs for several applications, including sensing and catalysis.<sup>19,35,40,273–284</sup> The properties of bimetallic NPs are governed by their composition as well as by the spatial distribution of the metals within each NP (i.e. configuration); thus, learning how to control both features is of the uttermost importance to eventually optimize these NPs for the desired application.<sup>34,285–287</sup> First of all, the two metals can be either alloyed or phase segregated. Alloys can have both disordered and atomically ordered structures, called intermetallics.<sup>34</sup> When phase segregated, many configurations are possible, including core@shell NPs and dimer-like NPs.<sup>50</sup>

The miscibility between the two metals is one of the main forces regulating the extent of mixing.<sup>288</sup> Generally, this principle applies to both bulk and nanomaterials. Yet, how immiscible metals distribute within nanoscale objects and how to eventually control their distribution remain poorly understood.<sup>46,48</sup> Furthermore, alloys of immiscible metals can be obtained at the nanoscale, especially when kinetically controlled synthetic approaches are employed.<sup>50</sup> Miscibility can also change at the nanoscale and exhibit size-dependence.<sup>23,24</sup> Overall, to advance the current state of the art in the synthesis of this important class of nanomaterials, increasing efforts should be directed towards understanding how to controllably target bimetallic NPs with tunable composition and configuration.

Colloidal synthesis is a powerful and versatile approach to form bimetallic NPs with tunable sizes, shapes, compositions and crystal structures.<sup>34,35,40–43</sup> The control over several reaction parameters has proven useful to advance the mechanistic knowledge on the factors determining the composition and configuration of multicomponent NPs.<sup>44–47</sup> As for metals, most studies have been performed on noble-metal containing NPs, for which a vast library of bimetallic structures exists.<sup>35</sup> The oxophilicity of other metals complicates their synthesis and makes working with them more unpredictable.<sup>60</sup> For example, the presence of a native oxide surface around Ga or Mn results in phase segregated dimeric structures following galvanic replacement, instead of the hollow alloys which were expected based on existing knowledge from noble metal NPs.<sup>42,289</sup> Yet, non-noble metals are certainly not less intriguing or appealing for applications, which include plasmonics and catalysis, compared to noble metals.<sup>190,289</sup>

In this work, we describe the synthesis of Cu-In NPs with different configurations via a sole synthetic approach. Cu-In bimetallic NPs have recently been attracting attention particularly in the field of catalysis.<sup>23–33</sup> While these examples in the literature suggest the importance of composition and element distribution as properties-determining features,<sup>31–41</sup> a suitable synthesis allowing for monodispersed and tunable NPs that could serve as a study platform to exploit the potential of these bimetallic particles remains to be found. We use In NPs as sacrificial seeds for a GRR with a copper molecular precursor and obtain intermetallic and phase segregated Cu-In NPs by simply tuning the reaction time and/or the precursors' ratio. Careful structural and compositional characterization of different samples reveals size-dependent kinetics in a reaction process involving first alloying, to form Cu<sub>11</sub>In<sub>9</sub> intermetallic NPs, followed by dealloying into Cu-In NDs, for which arguments are provided. We also isolate bulk-like Cu-Cu<sub>11</sub>In<sub>9</sub> NDs when using bigger In NPs templates, which are not accessible in smaller NPs due to size-dependent effects. We demonstrate that non-typical GRRs outcomes, “typical” meaning the formation of hollow particles obtained from noble metals, can be expected for oxophilic and non-conventional metal pairs.

## 5.2. Results and discussion

Monodisperse colloidal In NPs of 15 nm were synthesized by adapting a previously reported procedure (**Figure A3.1**).<sup>41</sup> Modifying an earlier synthesis protocol developed for Cu-Ga NDs,<sup>42</sup> In NPs were reacted with a copper molecular precursor at 160 °C for 30, 60 and 120 minutes. The copper molecular precursor is a copper(II)-oleylamine complex forming in the reaction mixture.<sup>42</sup> GRRs are electrochemical processes in which a sacrificial metal (herein metallic In,  $E_{\text{In}^{3+}/\text{In}^0}^\circ = -0.34$  V) is oxidized by a metal cation in solution possessing a more positive redox potential (herein Cu<sup>2+</sup>,  $E_{\text{Cu}^{2+}/\text{Cu}^0}^\circ = 0.34$  V) that, in turn, gets reduced and deposits onto the pre-existing template.<sup>42,125,127,132,134,139,152,174</sup>

First, the GRR outcome was characterized as a function of time, while keeping the Cu:In ratio constant; Cu-In bimetallic NPs with different morphologies and elemental distribution were isolated (**Figure 5.1a**). TEM characterization provides an overview of the bimetallic NP morphology (**Figures 5.1b-d**). At 30 and 60 minutes, spherical NPs are observed, with no visible changes in morphology and similar size distribution compared to the parental In NPs (**Figures 5.1b,c, Figure A3.1 and Table A3.2**). Instead, at 120 minutes, the NPs turn into

elongated dimer-like structures (**Figure 5.1d**). STEM-EDXS elemental maps show that the element distribution changes over time within the NPs while remaining uniform within each sample (**Figures 5.1e-g**). The spherical NPs obtained at 30 minutes possess a homogeneous distribution of Cu and In (**Figure 5.1e**). At longer reaction times, the two elements segregate. Segregation is already noticeable in the sample obtained at 60 minutes (**Figure 5.1f**); after 120 minutes, Cu and In exist as completely separated domains sharing an interface within the dimer-like NPs (**Figure 5.1g**). Quantitative elemental analysis of these samples by EDXS and ICP-OES evidenced that more Cu is incorporated in the NPs as the reaction time increases, which is consistent with the GRR mechanism. Specifically, the average atomic Cu content measured with both EDXS over a larger region of particles and elemental ICP analysis was 60%, 70% and 90% (at.%) for the NP samples obtained at 30, 60 and 120 minutes of reaction time, respectively. Notably, a striking jump from 1 at.% to 60 at.% Cu content, with no intermediate compositions, was observed with shorter reaction times and lower amounts of Cu precursor (**Figure A3.2** and **Table A3.3**).

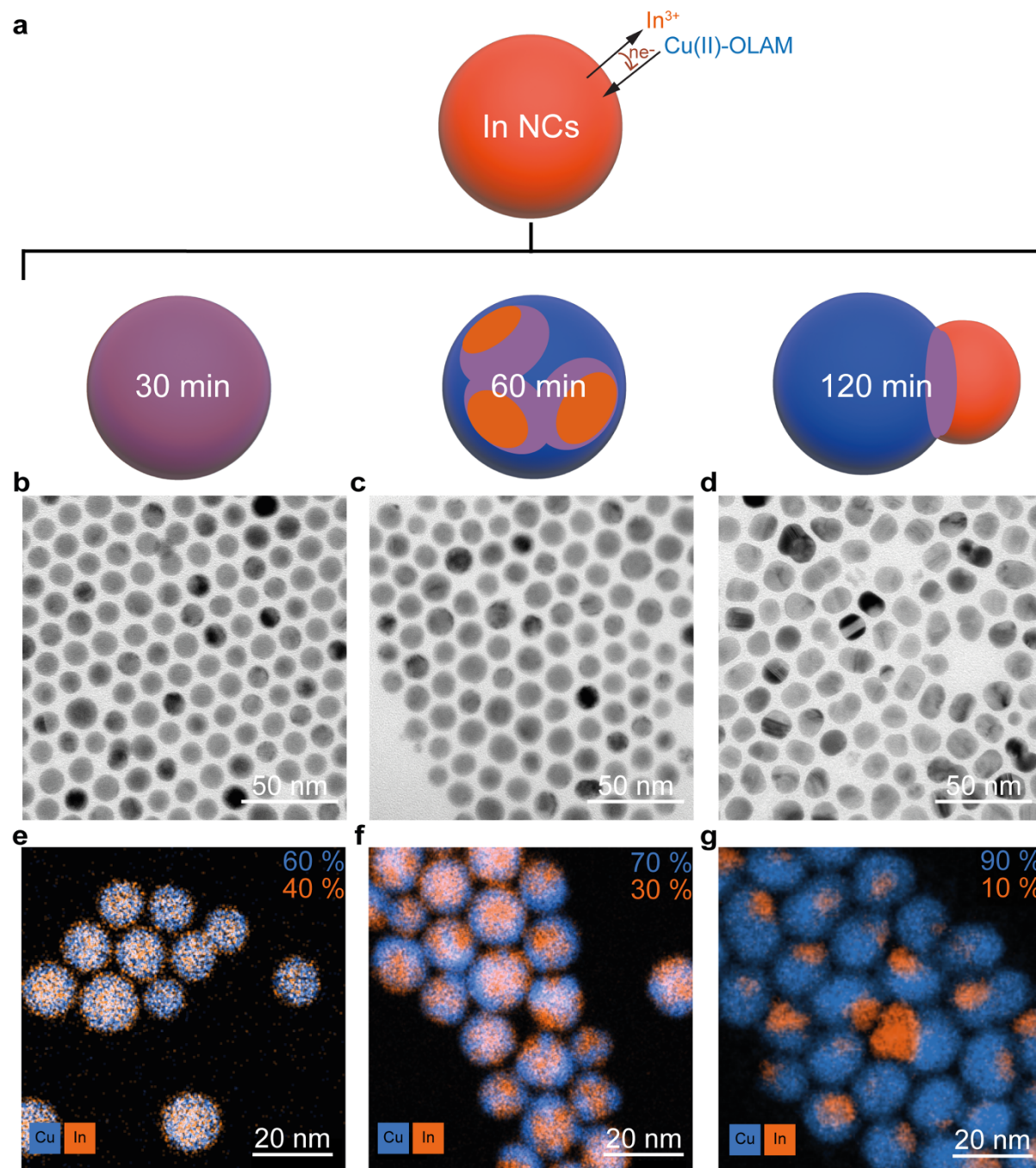


**Figure 5.1.** (a) Schematic representation of the reaction scheme and of the resulting products depending on the reaction time; (c-h) Bright-field TEM images and STEM-EDXS elemental maps of Cu and In (superposed) of the as-synthesized Cu-In NPs obtained at 30 min (c,f), 60 min (d,g) and 120 min (e,h). The Cu and In content measured by EDXS quantification are reported on the top right of EDXS maps (f-g); they indicate an increase in Cu content with reaction time. For all samples, 15 nm In NPs were used as sacrificial GRR seeds and the precursor ratio was set at 0.004 mmol of In and 0.006 mmol of Cu (see Appendix 3 and **Tables A3.1-2** for additional details).

Atomic resolution HAADF-STEM and corresponding STEM-EDXS elemental maps of individual particles (**Figures 5.2a-f** and **Figure A3.4**) combined with GI-XRD (**Figures 5.2g** and **A3.3**) provide additional compositional and structural details. After 30 minutes of reaction,

Cu-In NPs possess a homogeneous crystalline core, with interatomic distances corresponding to  $\text{Cu}_{11}\text{In}_9$  intermetallic phase, which are identified by analyzing the resulting FFT of the atomic resolution HAADF-STEM image, surrounded by an amorphous indium oxide shell (**Figures 5.2a,b**). The corresponding GI-XRD pattern is consistent with  $\text{Cu}_{11}\text{In}_9$  being the major crystalline component in the sample (**Figures 5.2g and A3.3**). The elemental quantification of 60 at.% Cu and 40 at.% In is also close to the  $\text{Cu}_{11}\text{In}_9$  elemental ratio (55 at.% Cu, 45 at.% In). After 60 minutes, the patchy spatial segregation of In and Cu elements is accompanied by the progressive transformation of  $\text{Cu}_{11}\text{In}_9$  into other nanocrystalline phases, which generates more heterogeneity within the particle (**Figure 5.2c**). The corresponding GI-XRD pattern of these NPs could be refined for In, Cu (both as Cu and  $\text{Cu}_2\text{O}$ ) and  $\text{Cu}_{11}\text{In}_9$  intermetallic (**Figures 5.2g and A3.3**). Finally, in the dimer-like Cu-In NPs obtained after 120 minutes of reaction, only the Cu domains could be aligned along a major zone axis and confirmed to be metallic Cu from the FFT analysis of the corresponding HAADF-STEM image (**Figure 5.2e**). Concomitantly, the GI-XRD pattern indicates Cu and  $\text{Cu}_2\text{O}$  as the major crystalline components, which is in agreement with the elemental analysis indicating 90 at.% of Cu. Metallic In and the  $\text{Cu}_{11}\text{In}_9$  intermetallic are also identified as two minor phases in the GI-XRD pattern. As the FFT indicates purely metallic Cu and TEM measurements are performed in vacuum, the  $\text{Cu}_2\text{O}$  detected in the XRD patterns most likely derives from oxidation during sample manipulation and data acquisition. The coupling of the XRD result with the EDXS mapping suggest that the dimer-like NPs obtained after 120 minutes of reaction consist of one domain of Cu/ $\text{Cu}_2\text{O}$ , one domain of In and probably a  $\text{Cu}_{11}\text{In}_9$  shared interface.

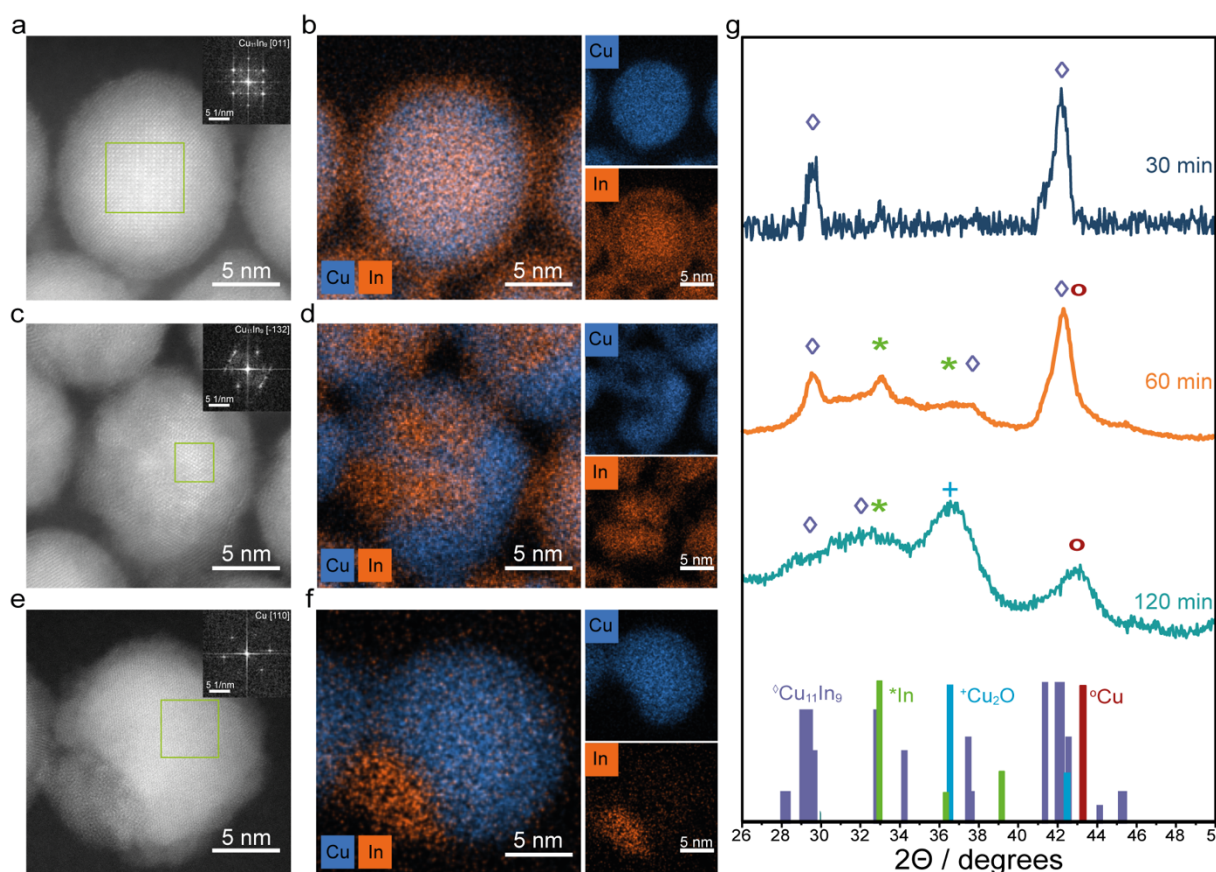


**Figure 5.2.** Atomic resolution HAADF-STEM images, including FFT of the selected areas in green, with their corresponding STEM-EDX elemental mapping of individual as-synthesized Cu-In NPs after (a,b) 30, (c,d) 60 and (e,f) 120 minutes reaction time. Oxygen STEM-EDX elemental mapping of these images can be found in **Figure A3.4**; (g) GIXRD patterns of the Cu-In NPs obtained at different reaction times as indicated by the labels. At the bottom, standard patterns of In (PDF 00-005-0642),  $\text{Cu}_{11}\text{In}_9$  (PDF 00-041-0883), Cu (PDF 00-004-0836) and  $\text{Cu}_2\text{O}$  (PDF 01-078-2076).

Altogether, a first mechanistic picture of the GRR between In NPs and the Cu precursor starts to shape up. In the initial stages of the reaction, Cu incorporates into the In NPs and forms the intermetallic  $\text{Cu}_{11}\text{In}_9$  structure without any intermediate alloy structures. This behavior is consistent with the bulk phase diagram (**Figure A3.5**).<sup>290</sup> As the GRR proceeds, more In is replaced by Cu. When the Cu content increases over 60 at. %, dealloying and phase segregation into Cu, In and  $\text{Cu}_{11}\text{In}_9$  takes place towards the final dimer-like Cu-In NPs. Interestingly, the Cu-In bulk phase diagram indicates that, at temperatures below 160°C, which is the reaction temperature, Cu and  $\text{Cu}_{11}\text{In}_9$  intermetallic should coexist, without segregation of In, for compositions containing more than 60 % Cu (**Figure A3.5**).<sup>290</sup> Differences between the bulk phase diagram and the behavior observed at the nanoscale are not uncommon. For example, alloying and dealloying phenomena leading to the coexistence of Cu, CuIn and In have been observed in thin films.<sup>291–293</sup> Stabilization of phases different than those reported for bulk



materials can occur in thin films and in NPs as a result of thermodynamics (i.e. increased significance of the surface free energy term as the thickness or size decreases) or kinetics (i.e. reaction proceeding under out-of-equilibrium conditions).<sup>294,295</sup> Dealloying of bimetallic NPs, those including metals of different oxophilicities, have indeed been reported under non-equilibrium conditions and during GRRs.<sup>125,131,296–301</sup> To understand the role of size in the phase segregation and deviation from the bulk phase diagram in the Cu-In NPs, we performed GRRs between larger In NPs of 19 and 22 nm and the Cu precursor, under the same reaction conditions.

19 and 22 nm In NPs were synthesized by modifying the reaction time of the same procedure followed for the 15 nm In NPs (**Figure A3.6**). Hereafter, Cu-In NPs will be labelled as Cu-In15, Cu-In19 and Cu-In22 depending on the size of the In NP seeds, being 15 nm, 19 nm and 22 nm, respectively. Cu-In19/22 NPs with different composition, elemental distribution and morphology were synthesized by tuning the amount of copper precursor added and/or the reaction time, as done for the Cu-In15 NPs discussed so far. The complete set of experiments is reported in **Figure A3.7** with details in **Table A3.4**. **Figure 5.3** reports data on the most relevant and representative samples.



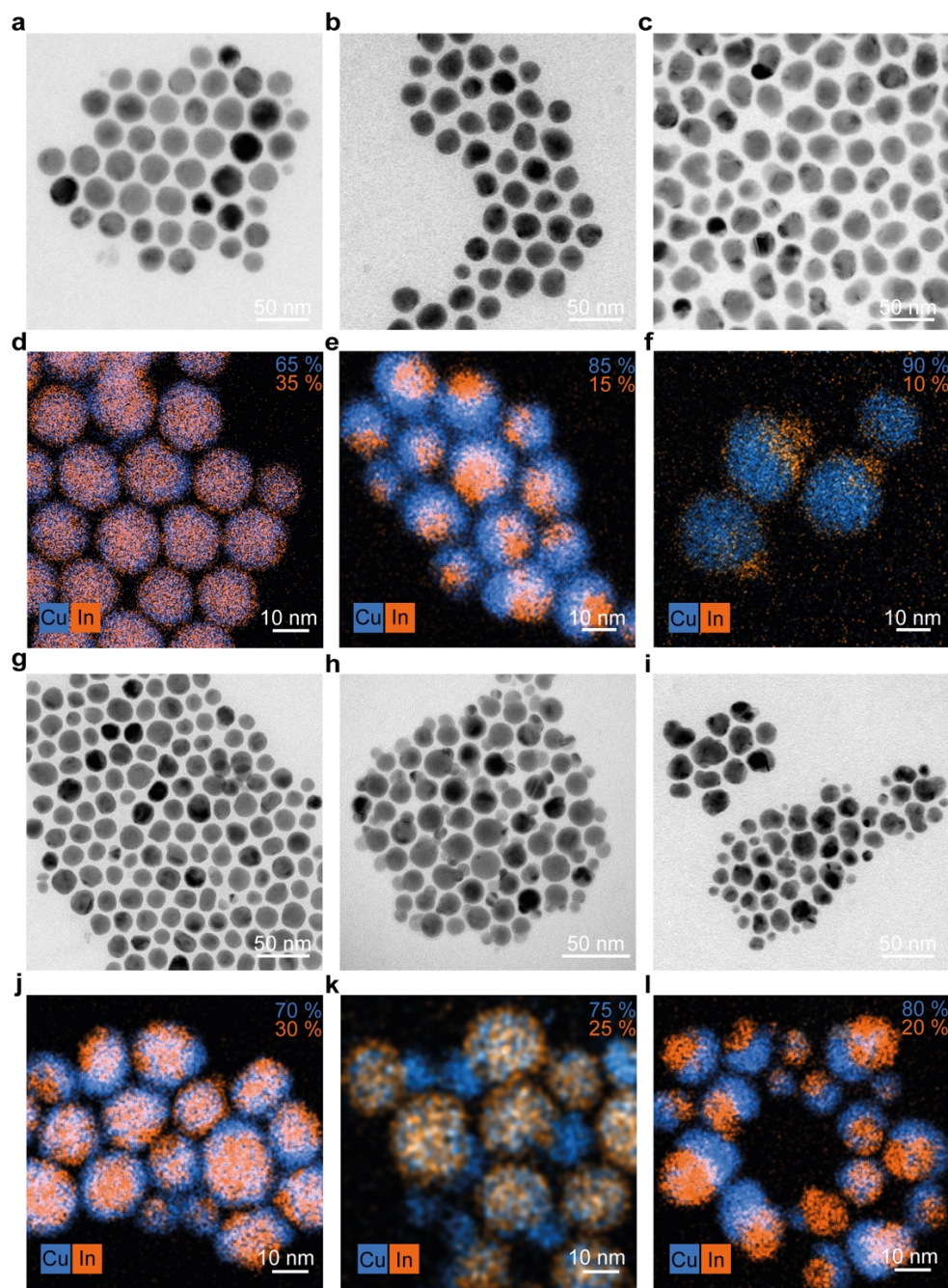


**Figure 5.3.** (a-c) Bright-field TEM images and (d-f) STEM-EDXS elemental maps of Cu-In19 NPs with increasing Cu content; these samples were synthesized by fixing the reaction time at 30 minutes and increasing the added Cu molecular precursor (0.0015, 0.003 and 0.006 mmol, respectively) for the same amount of In (0.004 mmol) (**Table A3.4**). 19 nm In NPs were used as sacrificial GRR seeds. (g-i) Bright-field TEM images and (j-l) STEM-EDXS elemental maps of Cu-In22 NPs with increasing Cu content; these samples were synthesized by fixing the reaction time at 30 minutes and increasing the added Cu molecular precursor (0.0015mmol for g,j and 0.006mmol for h,k) or increasing the reaction time (0.006 mmol of Cu and 60 min for i,l) for the same amount of In (0.004 mmol) (**Table A3.4**). 22 nm In NPs were used as sacrificial GRR seeds. For all samples, the Cu and In content measured by EDXS quantification over the regions shown in images are shown on the top right of the EDXS maps.

In the case of the Cu-In19 NPs, the three previously discussed GRR stages, which are homogeneously mixed (**Figures 5.3a,d**), patchy phase segregated (**Figures 5.3b,e**) and dimer-like (**Figures 5.3c,f**) NPs were obtained by tuning the added amount of Cu precursor for a reaction time of 30 minutes. Notably, the formation of dimer-like Cu-In15 NPs required 120 min with the highest amount of Cu precursor, indicating faster reaction kinetics with these bigger In NPs.

A different picture arises for the Cu-In22 NPs (**Figures 5.3g-l**). Firstly, the Cu-In22 NPs become slightly elongated already after 30 min with the lowest amount of Cu precursor (**Figure 5.3g**). STEM-EDXS elemental maps indicate the presence of a pure Cu domain around an area with uniformly mixed Cu and In (**Figure 5.3j**). The addition of more Cu generates well-defined dimer-like NPs (**Figure 5.3h**). These dimers consist of one domain of Cu interfaced with a larger domain where Cu and In are homogeneously mixed (**Figure 5.3k**). Only increasing the reaction time eventually forms the dimer-like NPs where Cu and In are separated into two distinct domains, equivalent to those observed for Cu-In15/19 NPs (**Figures 5.3i,l**).

The newly obtained Cu-In22 dimer-like intermediates were characterized in more details (**Figure 5.4** and **Figure A3.8**). The XRD pattern perfectly matched the  $\text{Cu}_{11}\text{In}_9$  intermetallic phase (**Figure 5.4a**), with the Cu domain being probably too small and overlapped with the intermetallic signal to be deconvoluted. The corresponding atomic resolution HAADF-STEM image, including the FFT of the selected area in green, (**Figure 5.4b**) and STEM-EDX elemental mapping (**Figure 5.4c**) performed at a single particle level are consistent with the bigger domain being the intermetallic phase and the smaller domain being copper.

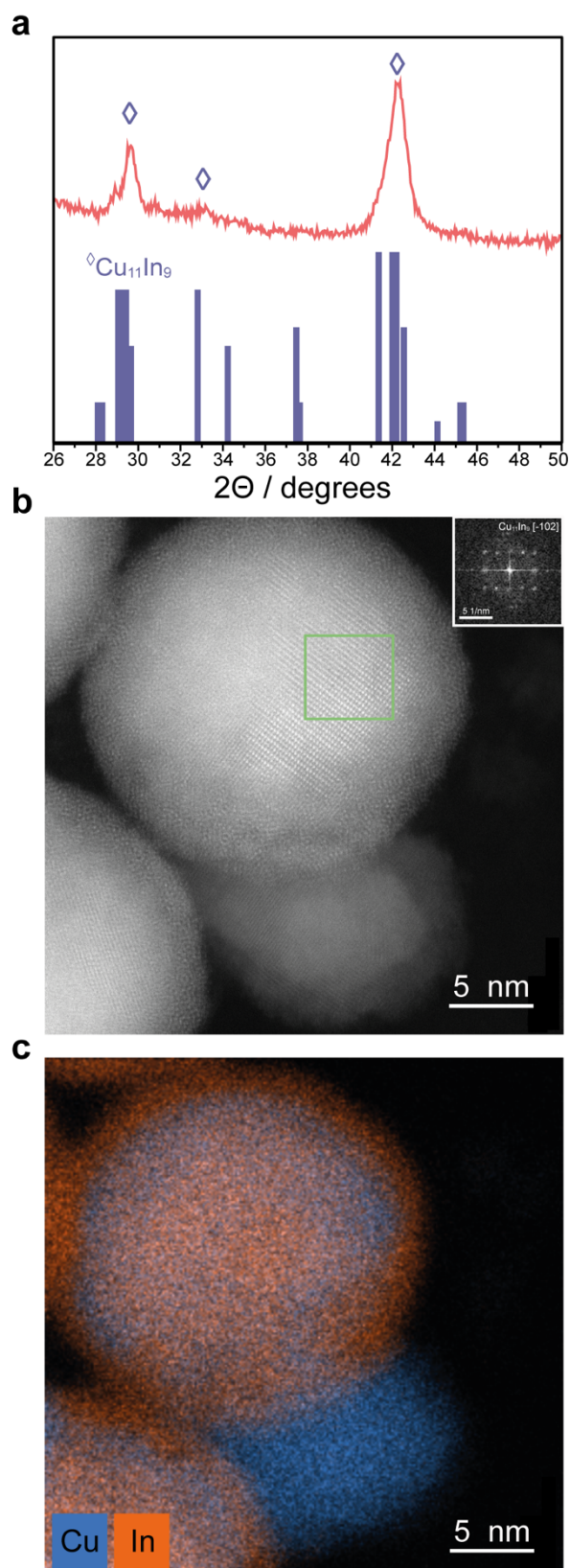


**Figure 5.4.** (a) GI-XRD pattern of the Cu-In22 dimer-like NPs, at the bottom standard pattern of  $\text{Cu}_{11}\text{In}_9$  (PDF 00-041-0883); (b) atomic resolution HAADF-STEM of an individual ND, including the FFT of the selected area in green corresponding to the  $\text{Cu}_{11}\text{In}_9$  intermetallic; (c) STEM-EDX elemental mapping of the same particle.

Altogether, the expansion of the GRR to bigger In NP seeds enables the construction of a full mechanistic picture of the Cu-In NP formation, which is summarized in **Figure 5.5**. Starting with metallic In NPs, Cu incorporates into the particle to form  $\text{Cu}_{11}\text{In}_9$  intermetallic NPs. In agreement with the bulk thermodynamics of the system, no intermediate alloys are isolated within detection limits. Additional incorporation of Cu results into their transition to phase segregated Cu-In dimer-like NPs. The intermediate structures are patchy phase segregated spherical NPs including Cu, In and  $\text{Cu}_{11}\text{In}_9$  domains for smaller sized In NPs, while Cu- $\text{Cu}_{11}\text{In}_9$  dimer-like NPs are identified for bigger In NPs. This Cu- $\text{Cu}_{11}\text{In}_9$  biphasic configuration is more coherent with the Cu-In bulk thermodynamics as discussed in previous paragraphs.

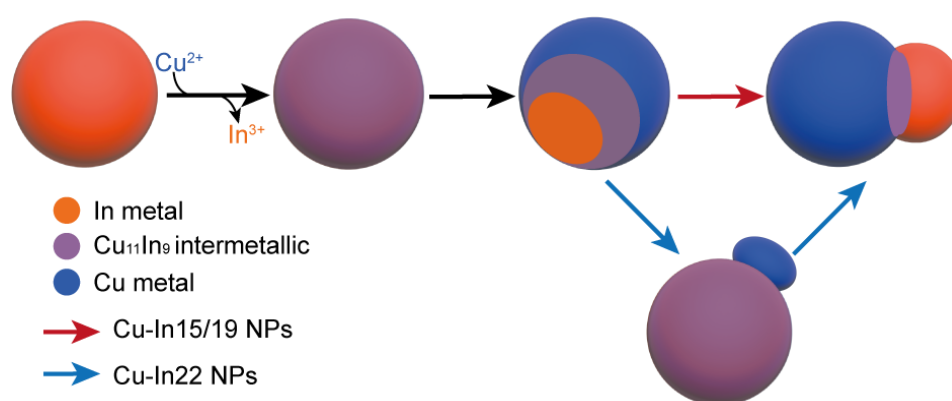


**Figure 5.5.** Schematic illustration of the reaction between In NPs and the copper precursor to form different Cu-In NPs as the reaction time is extended or the amount of copper precursor is increased. Independently of the In size, intermetallic spheres and Cu-( $\text{Cu}_{11}\text{In}_9$ )-In NDs are obtained. Different pathways are shown for the Cu-In<sub>15/19</sub> NPs (red arrow) and the Cu-In<sub>22</sub> NPs with their intermediate step (blue arrow).

The results indicate that size effects impact the GRR outcome and, more generally, the behavior of the Cu-In system at the nanoscale. Firstly, the GRR proceeds faster for bigger NPs than for smaller NPs. Secondly, the larger NPs do enable to capture structures which more closely resemble the composition expected by the bulk phase diagram.

To the best of our knowledge, no previous studies have investigated the sole size-dependence of the GRR, as size effects have often been convoluted with surface facet effects.<sup>302</sup>

The driving force for GRR is the difference in the redox potentials of In and Cu. Considering the size range of the In NPs, it is reasonable to assume that their initial redox properties are equivalent.<sup>303</sup> The shorter diffusion length of smaller particles should promote faster alloying/dealloying, which is not the case for the system discussed in this work.

A very few studies in the literature have specifically tackled the size-dependence of alloying and dealloying in NPs.<sup>300,304</sup> Gezelter and co-workers found that Au-Ag alloying is faster in smaller particles.<sup>304</sup> However, as Au and Ag are miscible metals over a wide compositional range, the same principles are not applicable to Cu-In.

Keeping in mind the immiscibility over a wide compositional range and the different crystalline structures of the two metals and the intermetallic phase (In is tetragonal with  $a = b = 3.252 \text{ \AA}$ ,  $c = 4.946 \text{ \AA}$ ,  $\beta = 90^\circ$ ; Cu is fcc with  $a = b = c = 3.615 \text{ \AA}$ ,  $\beta = 90^\circ$  and  $\text{Cu}_{11}\text{In}_9$  is monoclinic with  $a = 12.821 \text{ \AA}$ ,  $b = 4.355 \text{ \AA}$ ,  $c = 7.357 \text{ \AA}$ ,  $\beta = 125.523^\circ$ ), the initial replacement of In by Cu atoms will most likely induce strain into the In NPs. The smaller the NPs are, the more strained their structure will be due to the increased number of surface and interface atoms,<sup>305</sup> which will also hinder the transition towards the intermetallic stable phase. This phenomenon can reasonably explain the slower reaction kinetics of the smaller In NPs in the GRR with Cu to form the  $\text{Cu}_{11}\text{In}_9$  intermetallic.

As the GRR proceeds, the larger particles also undergo a faster dealloying process. This observation is consistent with the results from Strasser and co-workers on Pt-Co and Pt-Cu, although the authors do not provide a fundamental reason for their result.<sup>300</sup> As mentioned earlier, the bigger NPs do enable to capture a different intermediate, which is the  $\text{Cu-Cu}_{11}\text{In}_9$  biphasic configuration. One possible explanation to the observation of this structure only for the bigger In NPs can be found in the strain exerted on the chemical bonds in the vicinity of the  $\text{Cu/Cu}_{11}\text{In}_9$  interface. The atomic structures of the very simple fcc-Cu and the rather complex  $\text{Cu}_{11}\text{In}_9$  intermetallic do not allow for an obvious epitaxial relationship in the conventional picture of lattice mismatch.<sup>306</sup> Indeed, only fragments of the fcc-Cu structure match the monoclinic  $\text{Cu}_{11}\text{In}_9$  intermetallic, with average Cu-Cu distances approx. 6% larger in the latter (**Figure A3.9**). Smaller particle sizes might increase further this bond distance mismatch, thus making it prohibitive for a  $\text{Cu/Cu}_{11}\text{In}_9$  interface to exist. This effect might explain why the  $\text{Cu-Cu}_{11}\text{In}_9$  dimeric structures are observed only for the bigger In NPs. It is worth to note that the situation may be much more complex, with an interface including locally intertwined domains or amorphous volume fractions. These questions cannot be answered based on the current imaging as the interface is not stable and reconstruct under the electron beam while tilting the sample. Nevertheless, the existence of the  $\text{Cu-Cu}_{11}\text{In}_9$  dimeric structure represents an additional local minimum in the free energy diagram of the bigger NPs and might be responsible for reducing the kinetic barrier needed for dealloying, thus facilitating the



formation of the final dimer-like Cu-In NPs sharing a  $\text{Cu}_{11}\text{In}_9$  interphase. The phase segregation of indium is not contemplated by the bulk phase diagram. However, these NPs form under out-of-equilibrium conditions, where an electrochemical potential drives the substitution of In in the  $\text{Cu}_{11}\text{In}_9$  with Cu, which might explain such deviation from the ideal behavior expected under purely thermodynamic conditions.

Following the idea of representing colloidal synthesis as trajectories on the potential energy surface leading to various reaction products,<sup>307</sup> the energy landscape of the Cu-In NP synthesis can be drawn as a function of the Cu concentration (**Figure 5.6**). While the full energy landscape can be complicated, e.g. by additional minima and activation barriers associated with ligand desorption and reorganization, and keeping in mind that the relative potential energy of the different configuration are qualitative, the simplified schematics still serves its purpose. It is noted that higher reaction temperatures do increase the reaction kinetics (**Figure A3.10**), however the In NPs convert from solid to liquid at temperature above 160 °C,<sup>308</sup> thus the results are not comparable with those described above. The reaction does not proceed at lower temperatures (**Figure A3.11**), with one possible reason being that the energy provided to the system is insufficient for the formation of the intermetallic phase which requires a significant structural rearrangement from tetragonal In to monoclinic  $\text{Cu}_{11}\text{In}_9$  while Cu is incorporated.

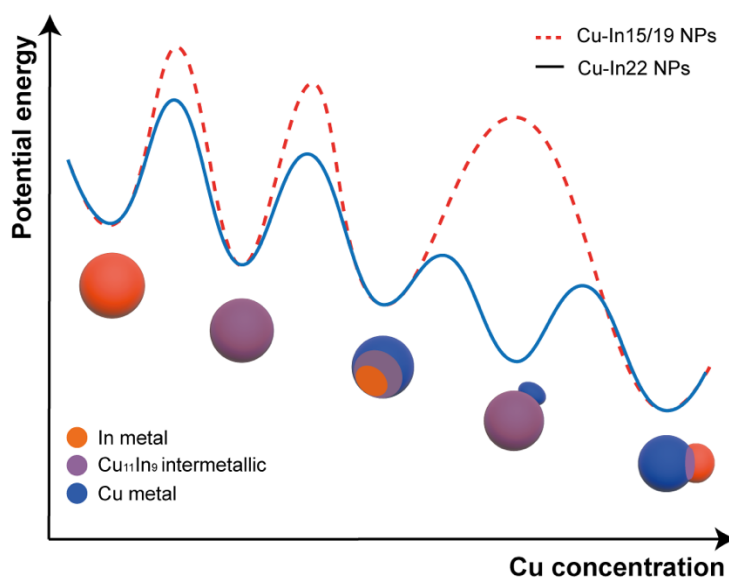


**Figure 5.6.** Potential energy landscape for the formation of Cu-In NPs starting from In NPs via GRR for different Cu concentrations. The slower alloying and dealloying kinetics of the 15 nm and 19 nm In NPs compared to the 22 nm In NPs are attributed to the higher energy barriers imposed by the structural strain induced by the Cu incorporation into the In structure. Because of their capacity to easily strain release, the bigger In NP seeds stabilize

the more bulk-like Cu-Cu<sub>11</sub>In<sub>9</sub> ND structure, which facilitates their conversion into the most thermodynamically stable dimer-like Cu-In NPs.

### 5.3. Conclusions

In conclusion, we have explored the reactivity of colloidal In NPs in a GRR with a copper molecular precursor to synthesize Cu-In NPs with unprecedented monodispersity and tunability. Intermetallic, phase segregated and dimer-like NPs were obtained. All three bimetallic configurations were synthesized by tuning the reaction time and/or the amount of added copper precursor, which both effect the extent of the galvanic exchange between copper ions and indium metal. We note that Cu<sub>11</sub>In<sub>9</sub> NPs have been reported before but with poor homogeneity.<sup>309,310</sup> The other In-Cu configurations are instead obtained for the first time.

While proving that the GRR is a powerful approach to access diverse bimetallic structures, we demonstrate that the common knowledge on GRR obtained via studies on noble metals, according to which alloyed nanoshells are expected to form, does not directly apply to oxophilic and poorly miscible metals. Importantly, we show how size-dependent kinetics and thermodynamics are crucial in understanding the outcome of GRR. We expect to inspire the bimetallic community into the extending the GRRs to less explored and more oxophilic metal pairs.

## Chapter 6

### Conclusions and outlook

In the current quest for selective and efficient catalysts to drive those chemical transformations which are important to move towards a more sustainable society, well-defined colloidal bimetallic NPs serve as an ideal platform for the exploration of composition-configuration-property relationships that are necessary for catalyst design.<sup>9</sup> The ratio between the two metals and their distribution within each NP along with the NP morphology can largely affect their behavior as catalysts. Thus, synthetic approaches that enable a fine tuning of the final NP must be established.<sup>9</sup>

A vast library of noble metal bimetallic structures already exist.<sup>35,110,125</sup> However, these metals are not always those of interest for many catalytic conversions. For example, the most promising catalysts for the electrochemical CO<sub>2</sub> reduction reaction (CO<sub>2</sub>RR) are those based on Cu. Compared to noble metal bimetallic NPs, bimetallic systems including Cu are fairly underexplored, especially when the second metal is an even more oxophilic metal. Reports are much more scarce or even inexistent when considering coupling Cu with elements of the liquid metal family, specifically Ga and In, despite their intriguing properties and a few theoretical and experimental works suggesting promising results in CO<sub>2</sub>RR.<sup>21–33</sup>

The main aim of this thesis was to advance the fundamental knowledge in the synthesis of Cu-Ga and Cu-In bimetallic NPs. The synthetic methodology of choice was the galvanic replacement reaction (GRR) since the differences in reduction potentials of the chosen pairs are large enough for the reaction to occur. Moreover, the possibility of controlling the extent of this reaction by reactant concentration or time proved to be very useful in the understanding of the mechanism of each replacement which allowed us to achieve an unprecedented variety of structures for these two bimetallic NPs.

Chapter 1 has provided information on the most commonly used synthesis approaches for colloidal bimetallic NPs, and motivated the choice of the GRR compared to those, along with discussing some of the unique properties of Ga and In. Following the description of the experimental methods in Chapter 2, Chapter 3 and Chapter 4 focused on the GRR of liquid Ga NPs with a copper molecular precursor to synthesize Cu-Ga NPs.



Chapter 3 showed that Cu-Ga NDs are the resulting product of a GRR reaction between Ga NPs and a Cu molecular precursors. This result was surprising when compared to the most typical hollow alloyed NPs obtained for noble metals. Extensive characterization showed that a gallium oxide shell was present around the Ga NPs throughout the reaction. This oxide shell is permeable to the Ga atoms migrating outwards into the solution but prevents the Cu atoms to mix with the liquid core, thus forcing them to nucleate on top in a noncentrosymmetric fashion. Combined with the oxide's viscoelasticity and the liquid nature of Ga, the oxide shell explained the peculiar mushroom-like NDs. The GRR was demonstrated applicable beyond Cu to obtain Ag-Ga NDs and trimetallic Ag-Cu-Ga NPs. Overall, Chapter 3 showcased the very intriguing and peculiar reactivity of Ga NPs in an exciting initial approach to this field of research, while reporting on the formation of bimetallic NPs which did not exist before.

The results discussed in Chapter 3 raised a follow up question: if the oxide shell acts as a barrier against Cu and Ga mixing, is it possible to overcome this limitation by eliminating or reducing its thickness to a minimum? Therefore, Chapter 4 focused on studying the modulating effect that capping ligands have on the oxidation process of Ga NPs and its consequences on the GRR mechanism. Surface ligands containing different anchoring groups were investigated, specifically oleic acid (OLAC), oleylamine (OLAM), trioctylphosphine (TOP) and dodecanethiol. The affinity of the functional group towards the oxide surface was discovered to tune the thickness of the native gallium oxide. TOP and DDT were found to be more efficient at hindering its growth. Nevertheless, unlike the initial assumption, reducing the oxide thickness did not lead to the formation of CuGa alloys but, instead, to Cu NPs nucleating separately. Chapter 4 evidenced the importance of the surface chemistry of colloidal Ga NPs, which is completely unexplored, not only when using them as seeds for bimetallic synthesis but also in every other potential application.

Finally, the applicability of the developed synthetic mechanism to other, yet similar in principle, metal seed was investigated. Chapter 5 focused on the GRR of In NPs of different sizes with the same Cu molecular precursor used for the reaction with the Ga NPs. Bimetallic Cu-In NPs with different compositions and configurations were obtained with unprecedented tunability. Control on the extent of the GRR enabled the synthesis of monodisperse samples, which included intermetallic  $\text{Cu}_{11}\text{In}_9$  NPs, phase segregated Cu-In NPs consisting of Cu, In and intermetallic domains, and Cu-In NDs. Careful structural characterization revealed that the initial alloying into ordered crystalline structures is followed by a progressive dealloying.

Moreover, the use of bigger In NPs as sacrificial templates evidenced size-dependent reaction kinetics and, most importantly, the trapping of the bulk-like Cu-Cu<sub>11</sub>In<sub>9</sub> structures. Finally, a free energy diagram reporting the different configurations of the obtained bimetallic NPs versus the Cu concentration was proposed to facilitate the comparison with the In-Cu bulk phase diagram. The variety of Cu-In NPs reported in this Chapter was unprecedented in the literature.

In conclusion, besides achieving a deeper understanding on the chemistry and properties of liquid Ga NPs and In NPs, this thesis demonstrated that the GRR is a powerful and versatile tool for the synthesis of diverse and complex bimetallic structures. This approach enables the necessary tunability, especially in the case of Cu-In bimetallic NPs, to generate ideal platforms for the exploration of CO<sub>2</sub>RR catalysts. Yet, the obtained results also proved that the common knowledge on GRR mechanism, as described in Chapter 1, does not directly apply to more oxophilic and less miscible metal pairs.

Ongoing and near future projects include the testing of the synthesized bimetallic NPs as catalysts for CO<sub>2</sub>RR and the extension of the GRR to other bimetallic systems.

Regarding the CO<sub>2</sub>RR testing, initial electrocatalytic measurements on the Cu-Ga NDs have identified an anomalous behavior of the Ga domain which directed us to firstly understand the electrocatalytic performance and demeanor of individual liquid Ga NPs. Now that this knowledge is acquired,<sup>190</sup> the testing of their catalytic behavior can proceed by studying NDs with different domain relative size (i.e. composition) and CuGa alloyed compounds, which have been meanwhile synthesized in the group. As for the Cu-In NP system, pairing their testing with parallel studies on the electrocatalytic behavior of these materials via synchrotron techniques, such as *operando* XAS, could prove of great interest for the understanding and optimization of their catalytic performance, similarly to what already done by our group for different materials.<sup>20,311,312</sup>

Finally, efforts should be directed towards the extension of the library of Ga- and In- based bimetallic NPs. As clear disparities between Ga- and In- seeds were observed, questions arise regarding the effect that the oxidative metal ion has on the final morphology of the bimetallic NP, as different configurations are currently being observed for metals other than Cu and Ag. In particular, the fundamental chemistry questions to address are whether trends are observed

between metals and in what parameters are they based: (i) their reduction potential, (ii) their crystalline structure, (iii) the relationship between the metal-metal and metal-Ga/In bonding energies, (iv) the size of the metal atoms, (v) their miscibility with the seed and (vi) the affinity towards the oxide shell. As the final configuration might be dependent on more than one of the previous factors, these studies are challenging, yet intriguing and important to move the field forward. In addition, these future studies will consider the possible temperature-dependent reactivity of In. Unveiling the main reasons driving these different configurations could open new possibilities of rationally tuning the resulting bimetallic NPs in a versatile fashion, as done for noble metal bimetallic NPs.

Moreover, future in-situ studies at the synchrotron might provide more information on the mechanisms proposed, including a more quantitative investigation on the hypothesized strains caused between the different domains, if this is found to be general across different combinations of metals.

## Appendix 1

### Supporting information to Chapter 3

#### Exploring the chemical reactivity of gallium liquid metal nanoparticles in galvanic replacement

##### Characterization of the Cu(II)-OLAM and Cu(II)-TOP complexes:

The formulation of these complexes could not be deduced from mass spectrometry, which is unsurprising given the non-volatile nature of the supporting ligands. Only random aggregates of Cu ions were detected that we suspect arise from decomposition of the complexes. No signals from the complexes were detected by Nuclear Magnetic Resonance (NMR) spectroscopy due to the paramagnetic Cu(II) ions that are present. Whilst we could not determine the exact formulae or coordination geometries of the complexes, we assume that the ligands simply coordinate to Cu(OAc)<sub>2</sub>, yielding Cu(OAc)<sub>2</sub>(OLAM)<sub>x</sub> and Cu(OAc)<sub>2</sub>(TOP)<sub>x</sub>.

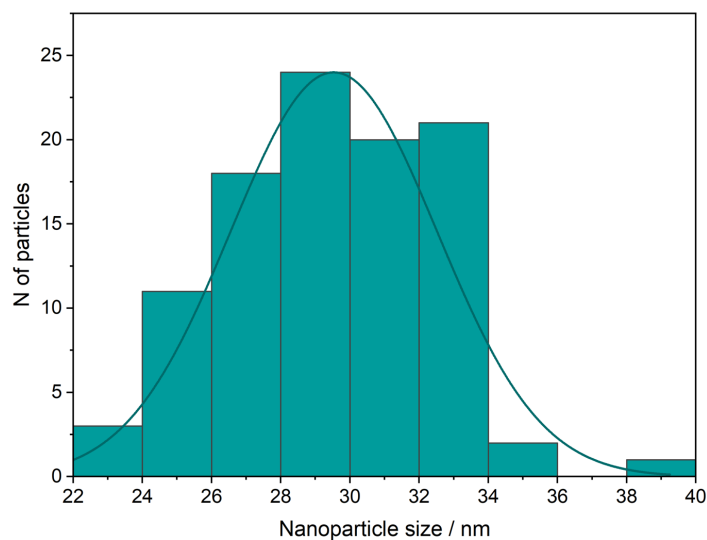


**Figure A1.1.** Statistical analysis of the starting Ga NPs ( $30 \pm 3$  nm).

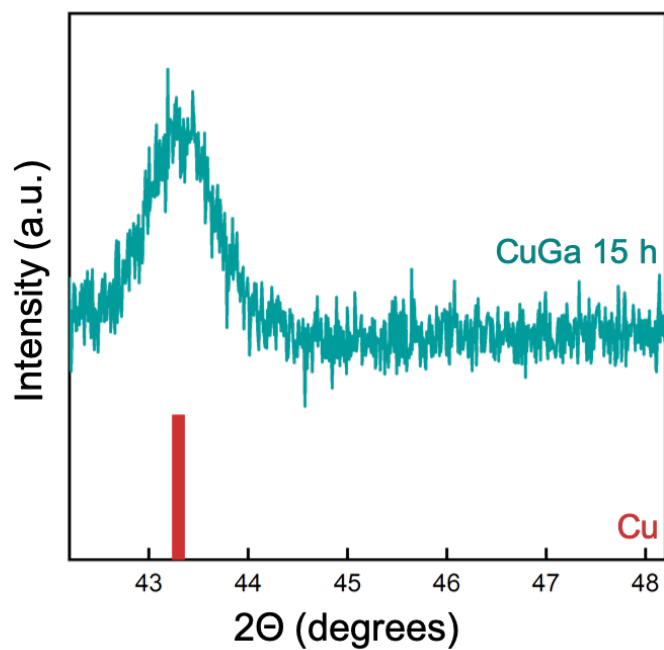


**Figure A1.2.** XRD pattern under air-free conditions of as-synthesised Cu-Ga NDs.

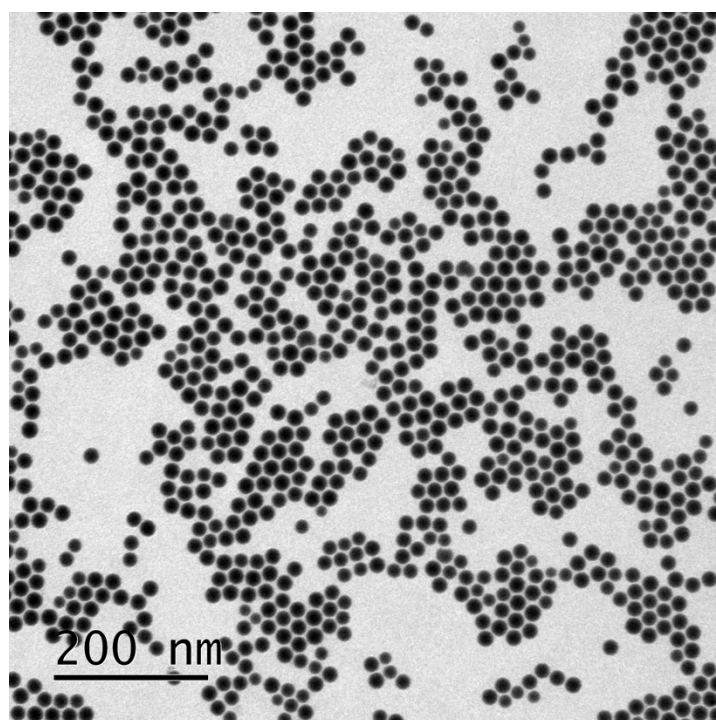


**Figure A1.3.** Low-resolution TEM image of the Ga NPs after undergoing the same synthetic conditions as for the Cu-Ga nanodimers but without the addition of the Cu precursor.

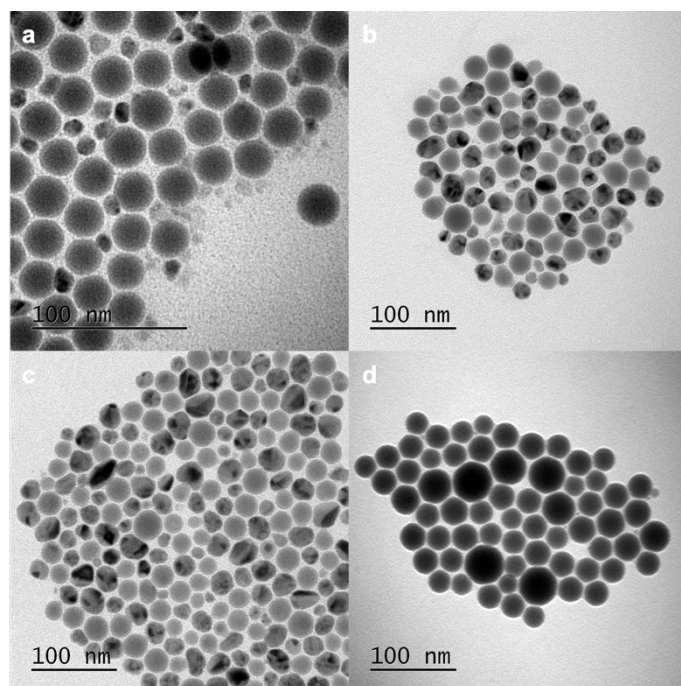


**Figure A1.4.** TEM images of the resulting NPs after reacting the Ga seeds with the  $\text{Cu}(\text{OAc})_2$  in the standard reaction conditions (15 hours and  $150^\circ\text{C}$ ) in the presence of: (a) 1 mL of OLAM, (b) 0.75 mL of OLAM and 0.25 mL of OLAC, (c) 0.25 mL of OLAC and 0.75 mL of OLAM and (d) 1 mL of OLAC.

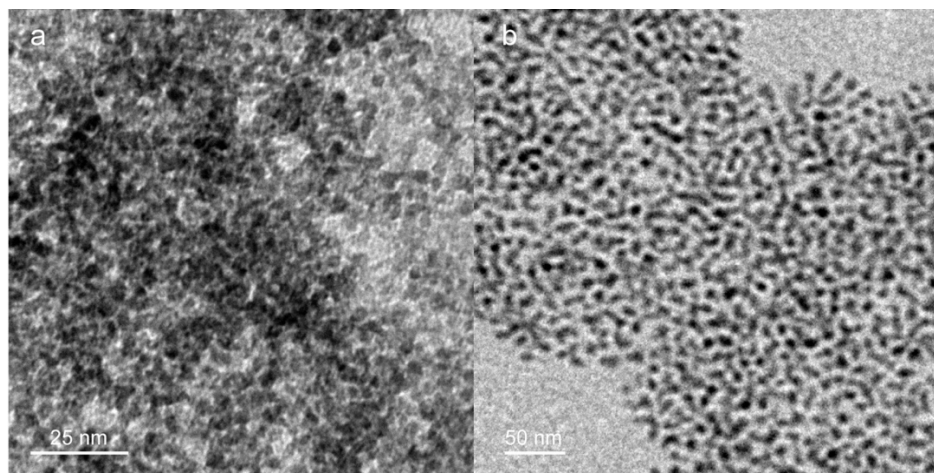


**Figure A1.5.** TEM of the (a) as-synthesised  $\text{Ga}_2\text{O}_3$  NPs and (b) the same particles after being subjected to the Cu-Ga nanodimers synthetic conditions.

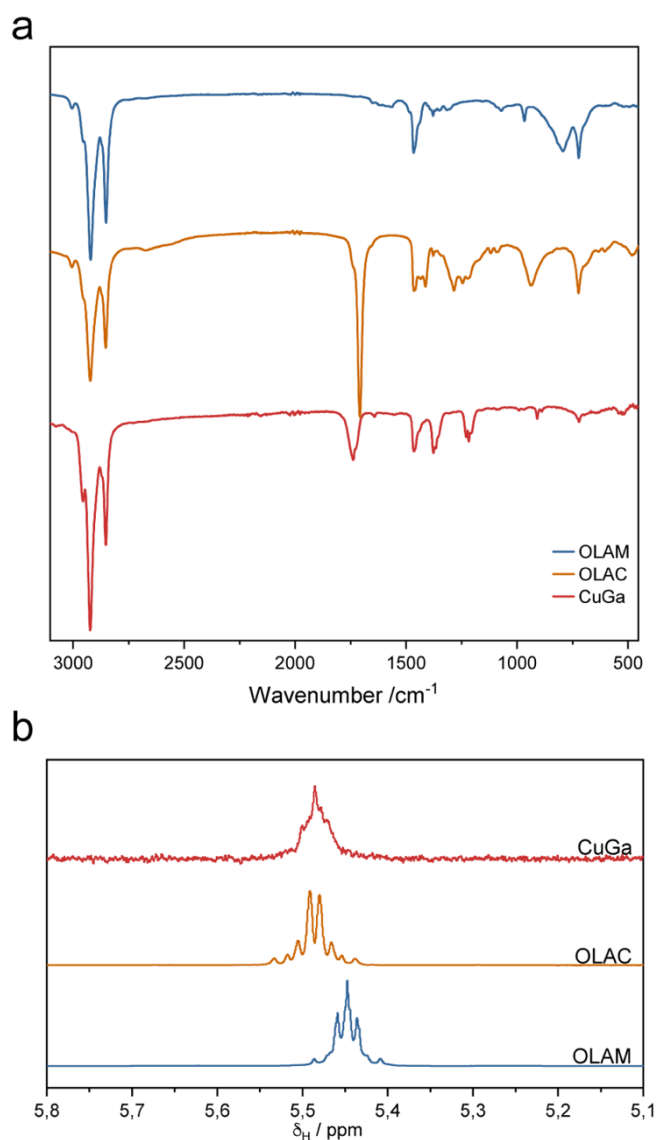


**Figure A1.6.** (a) FTIR spectra of OLAM (in blue), OLAC (in orange) and Cu-Ga NPs (in red). (b)  $^1\text{H}$  NMR spectra of the Cu-Ga NPs, OLAC and OLAM (same colours as in A) in  $d_8$ -toluene, showing only the alkene CH region for clarity.

The presence of the  $\text{C}=\text{O}$  stretching around  $1700\text{ cm}^{-1}$  and of the typical carboxylate peaks between  $1400$  and  $1500\text{ cm}^{-1}$  in the FTIR spectrum in **Figure A1.6a** together with the clear NMR alkene region in **Figure A1.6b** are consistent with OLAC being present as surface ligand.

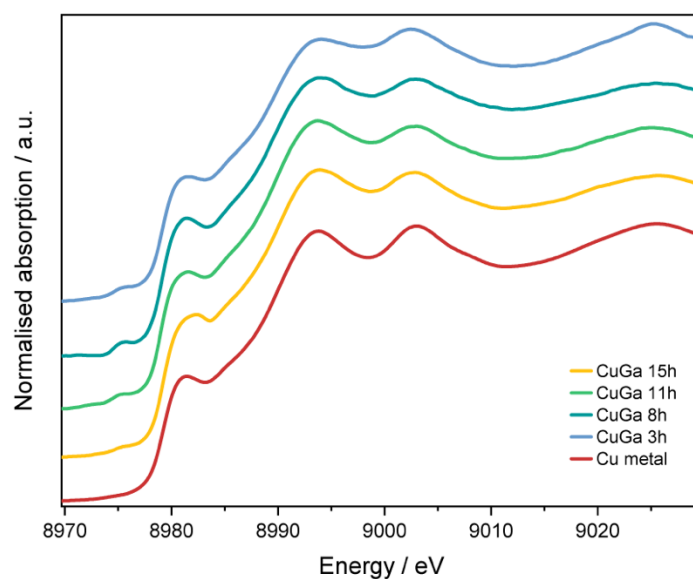


**Figure A1.7.** Cu K-edge XANES spectra of the aliquots taken at 3h, 8h, 11h, and 15h during the synthesis of the CuGa NDs together with the reference spectra of metallic Cu.

Subtle difference in the XANES spectra can be assigned to variations in the geometry/coordination around the absorbing atom and generated by the continuous growth of the Cu domain. It is well-known that the features of XANES spectra (i.e. their position, their relative intensity) of particles smaller than a few nanometers are highly sensitive to their size and also to the species adsorbed on their surface.<sup>313</sup>

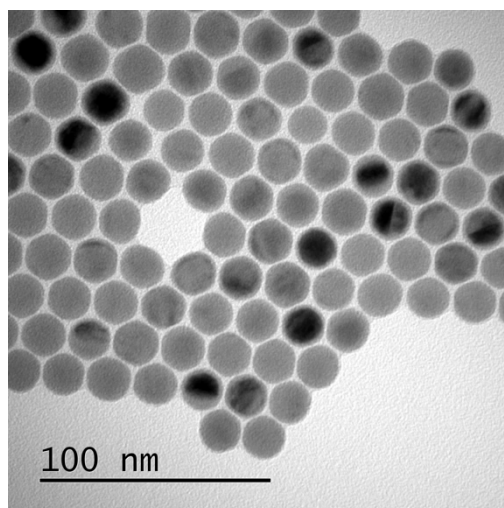


**Figure A1.8.** TEM image of the as-synthesised In NPs.



## Appendix 2

### Supporting information to Chapter 4

#### Modulating the reactivity of liquid Ga nanoparticles by modifying their surface chemistry

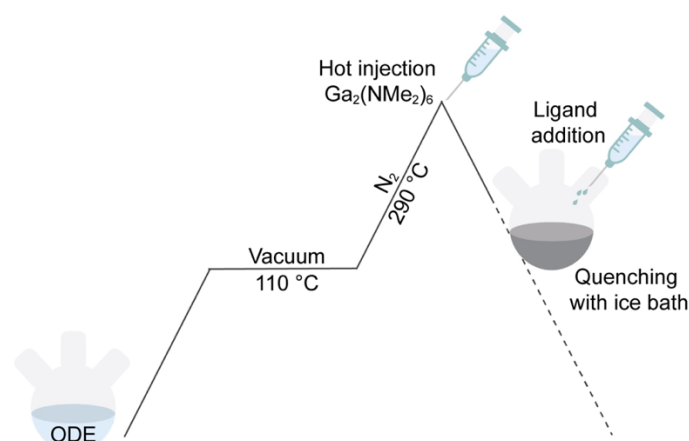


**Figure A2.1.** Reaction scheme of the synthesis of Ga NPs capped with different ligands.

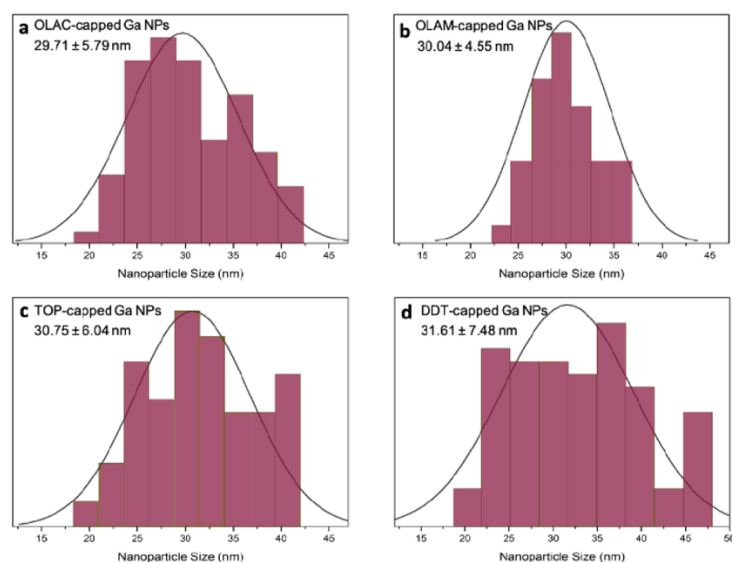


**Figure A2.2.** Size distribution of as-synthesized Ga NPs with different capping ligands (a) OLAC, (b) OLAM, (c) TOP, and (d) DDT. Size statistics were performed using ImageJ software and counting at least 150 NPs per sample.

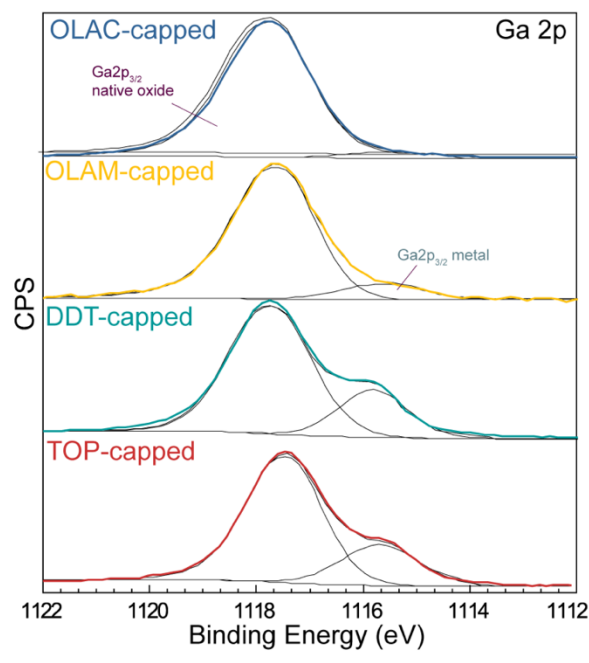


**Figure A2.3.** XPS spectra for Ga 2p of each ligand-capped NP on day 0 showing both the presence of native gallium oxide and Ga metal with different ratios in each case.

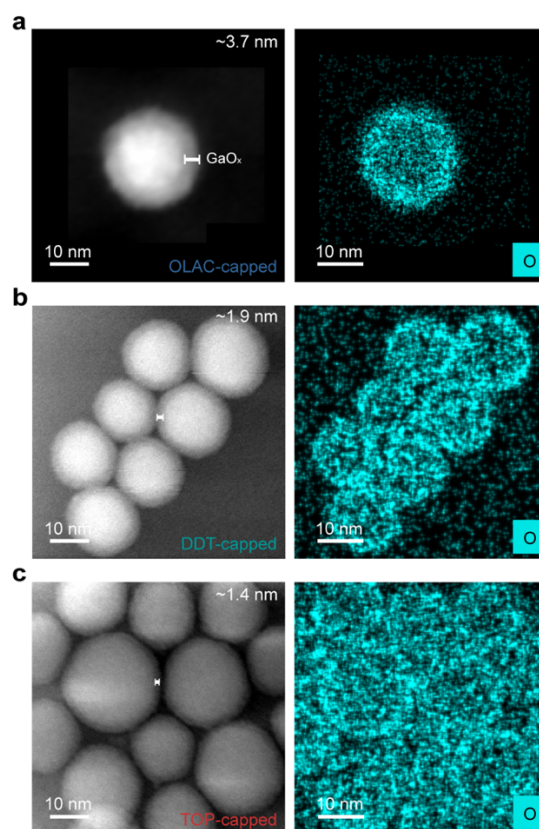


**Figure A2.4.** HAADF-STEM (left) and EDXS (right) of Ga NPs capped with (a) OLAC, (b) DDT and (c) TOP showing the oxide shell as a lighter contrast (left) and in light blue (right). The number on the top right of each HAADF-STEM corresponds to an approximative measure of the oxide thickness of each sample with matches well with the XPS calculation reported in **Figure 4.2c**.

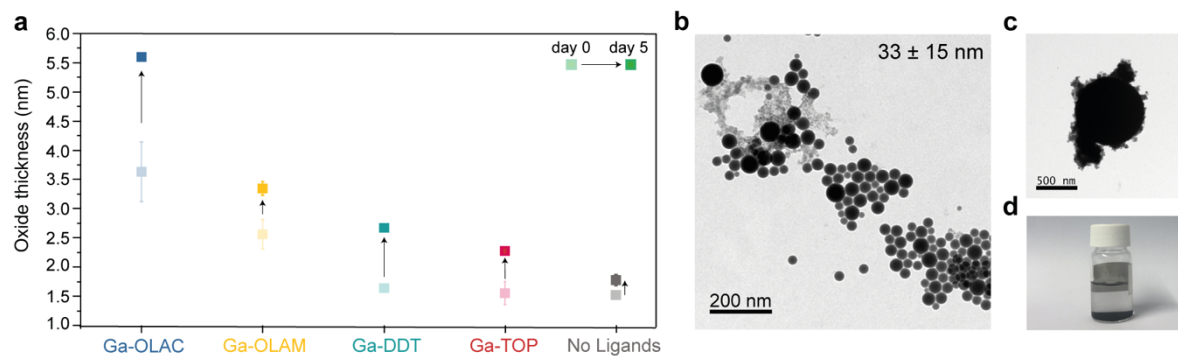


**Figure A2.5.** (a) Same graph as in Figure 3b with the addition of the Ga NPs without ligands; TEM images of the Ga NPs synthesized without ligands (b) showing their average size and their standard deviation on the top left of the image and (c) one of the numerous Ga blobs that could be found all over the TEM grid; (d) picture of the precipitated Ga NPs (taken after 15 minutes of their synthesis).

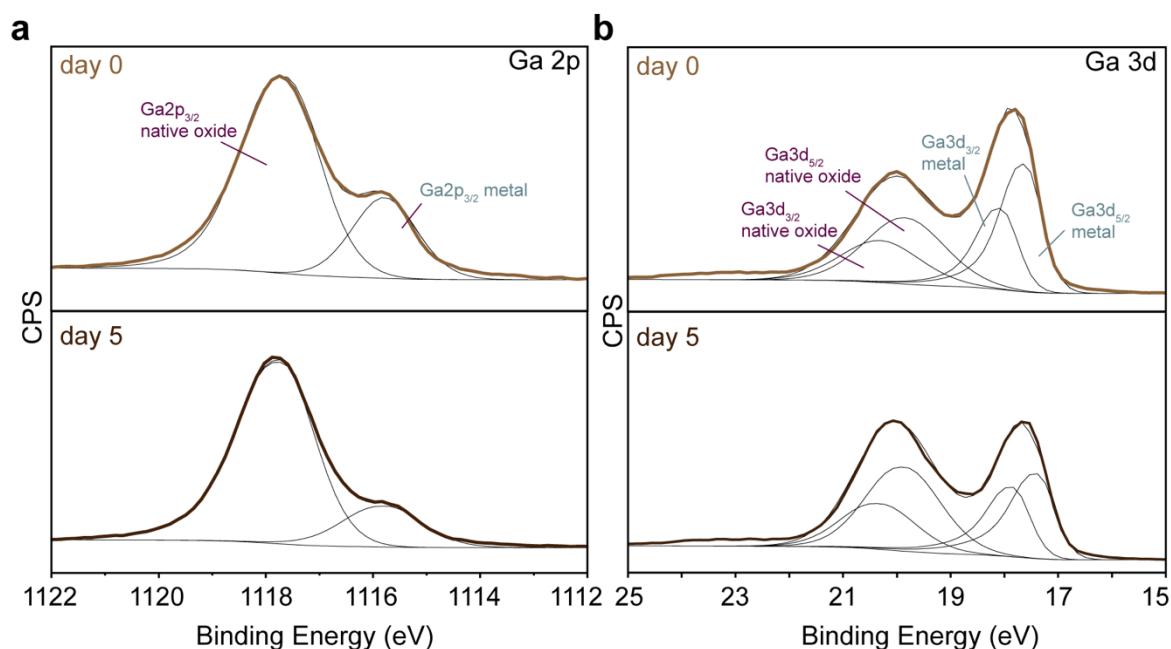


**Figure A2.6.** XPS spectra in the (a) Ga 2p region for the non-capped Ga NP at day 0 (up) and at day 5 (down) and (b) Ga 3d region for the non-capped Ga NP at day 0 (up) and at day 5 (down).

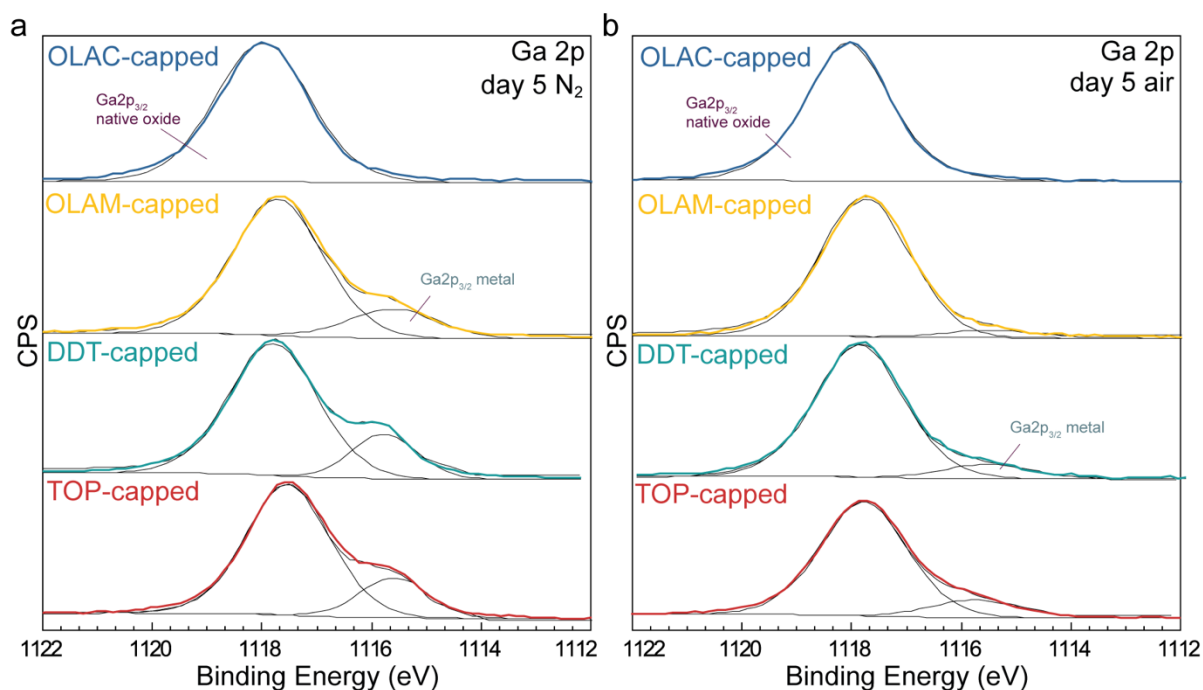


**Figure A2.7.** XPS spectra in the Ga 2p region of each ligand-capped Ga NP 5 days after the synthesis of samples (a) left inside the glovebox under N<sub>2</sub> atmosphere and (b) left in air to simulate a complete passivation showing both the presence of native Ga oxide and Ga metal with different ratios in each case.

### GRR with OLAM-, TOP- and DDT-capped Ga NPs obtained via ligand exchange from OLAC-capped Ga NPs:

OLAC-capped particles that had been stored in the glove box for several days were confirmed to possess a thick oxide shell by XPS (**Figure A2.8**) before undergoing the ligand exchange procedure described below. This same technique was then used to verify the effectiveness of the ligand exchange.

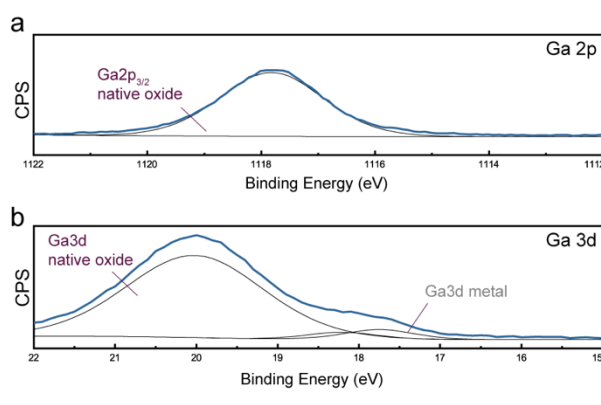


**Figure A2.8.** XPS spectra in the (a) Ga 2p and (b) Ga 3d regions for Ga NPs capped with OLAC 30 days after their synthesis, kept under inert atmosphere, showing an extended passivation of the Ga NP surface.

**Figure A2.9a** shows the XPS spectra of the signature peaks for OLAM, TOP and DDT after the ligand exchange, hence confirming the success of this procedure in each of our control experiments (see additional discussion below and **Figure A2.10**). We then repeated the same GRR experiments as before, now using samples with different ligands but all possessing a thick oxide shell. **Figure A2.9b** shows the resulting particles after the GRR. We can clearly observe how Cu-Ga nanodimers now form in every case independently of the capping ligand. Moreover, a control experiment in which an excess of TOP and DDT was added to a mixture of copper precursor, OLAM, OLAC and ODE in the absence of Ga NPs proved that the ligands themselves do not cause the reduction of Cu.

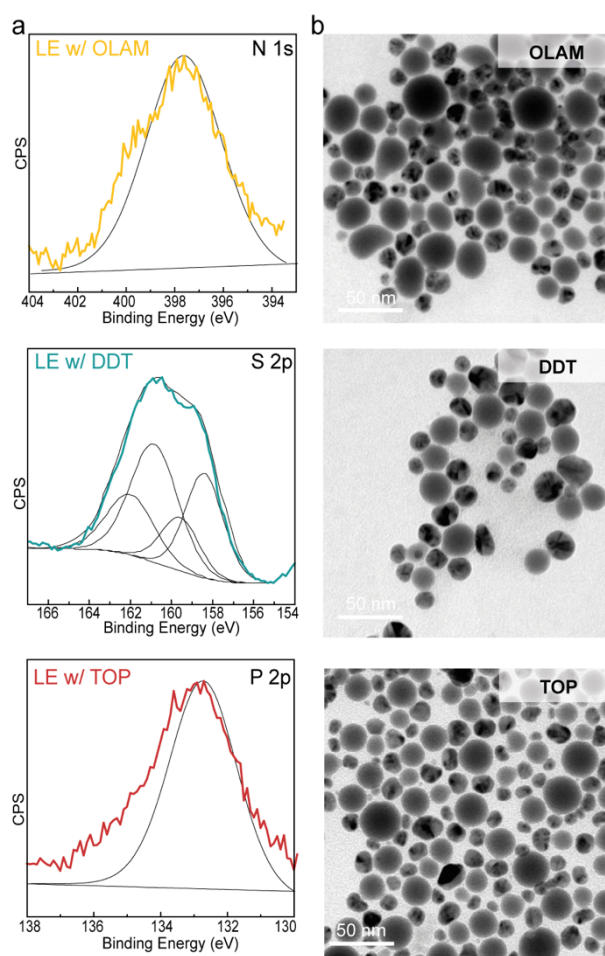


**Figure A2.9.** (a) XPS spectra showing the signature ligand peaks for the OLAC-capped NPs after ligand exchange with OLAM (yellow, N 1s), DDT (turquoise, S 2p) and TOP (red, P 2p),; (b) TEM images of the resulting NPs after GRR showing the formation of Cu-Ga nanodimers for each case.

Besides the signature ligand peaks mentioned above, we analyzed the C1s spectra of the Ga NPs before and after ligand exchange. The broad peak located at 288.72 eV is assigned to the carboxylic carbon (COOH) and only appeared for the OLAC-capped Ga NPs (**Figure A2.10a**). We therefore used this peak as further verification of the success of the ligand exchange. After ligand exchange, samples with TOP, OLAM, and DDT did not exhibit the aforementioned peak, indicating that OLAC was successfully stripped from the NPs surface (**Figure A2.10b**).

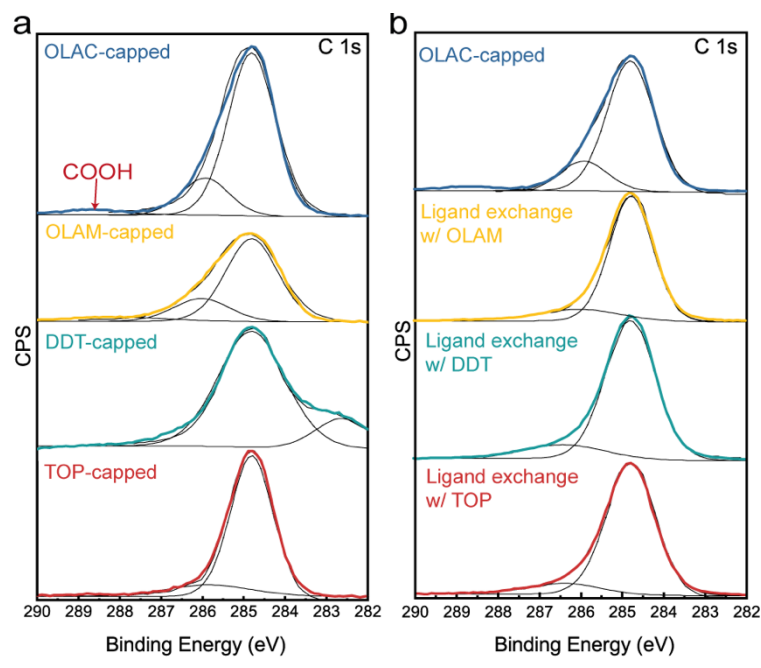


**Figure A2.10.** XPS C1s spectra of (a) as-synthesized Ga NPs capped with various ligands, and (b) Ga NPs after ligand exchange with various ligands.

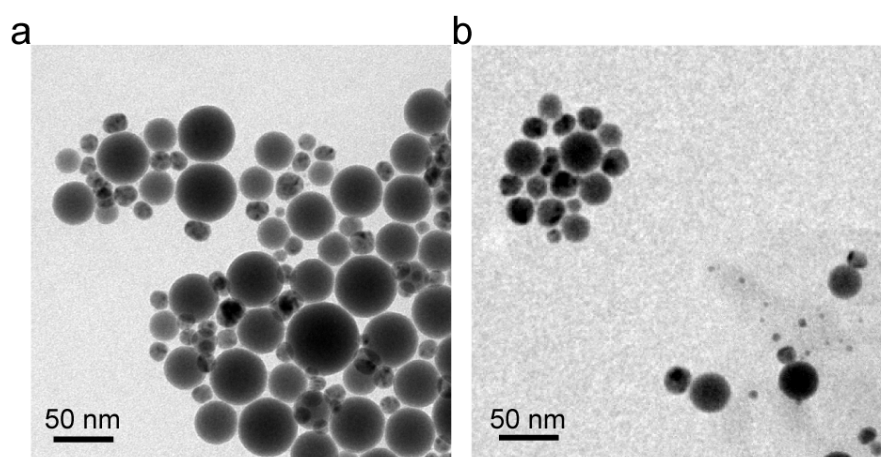


**Figure A2.11.** TEM images of the CuGa nanodimers formed from old DDT-capped Ga NPs after (a) 4 and (b) 6 hours. These DDT-capped Ga NPs had an oxide shell at least as thick as for the fresh OLAM-capped Ga NPs.

**Table A2.1.** Average size for the Cu and Ga domains after GRR and relative ratio between the atomic concentration of Cu and Ga of the GRR product (data from ICP analysis).

<b>Ligand</b>	<b>OLAC</b>	<b>OLAM</b>	<b>DDT</b>	<b>TOP</b>
<b>Cu size (nm)</b>	14.8	17.5	13.5	13.5
<b>Ga size (nm)</b>	22	12	22.3	21.6
<b>[Cu]/[Ga]</b>	0.2	0.8	0.5	0.5

## Appendix 3

### Supporting information to Chapter 5

#### Tailoring morphology and elemental distribution of CuIn nanoparticles via galvanic replacement

##### In:Cu ratio in the Cu-In NPs synthesis:

In the simplest case scenario, the oxidation from In metal to  $\text{In}^{3+}$  is the most thermodynamically favorable and that the copper in the precursor was proven to be  $\text{Cu}^{2+}$  in a previous work.<sup>42</sup> Therefore, calculations were done assuming  $\text{In}^{3+}$  and  $\text{Cu}^{2+}$  ions. The added amount of In NPs was kept constant across all sample, which is 1 mL of a 4 mM In solution. The added volume of the 4 mM  $\text{Cu}(\text{OAc})_2$  solution was varied. The reported Cu:In ratio indicates the targeted ratio in the final NPs if all the added copper ions were to galvanically exchange all the In atoms according to the redox reaction:



To give one example, the Cu millimoles added for Cu:In = 100:0 were expected to fully convert the In NPs into Cu NPs, which was not the case.

**Table S1** reports the actual In and Cu millimoles reacted based on the targeted Cu:In ratio.

**Table S1.** Added millimoles of In and Cu along with the targeted Cu:In ratio in the final NPs calculated based on eq. (A.1)

#	20 Cu : 80 In	50 Cu : 50 In	80 Cu : 20 In	100 Cu : 0 In
In mmol	0.004	0.004	0.004	0.004
$\text{Cu}^{2+}$ mmol	0.0015	0.003	0.0045	0.006



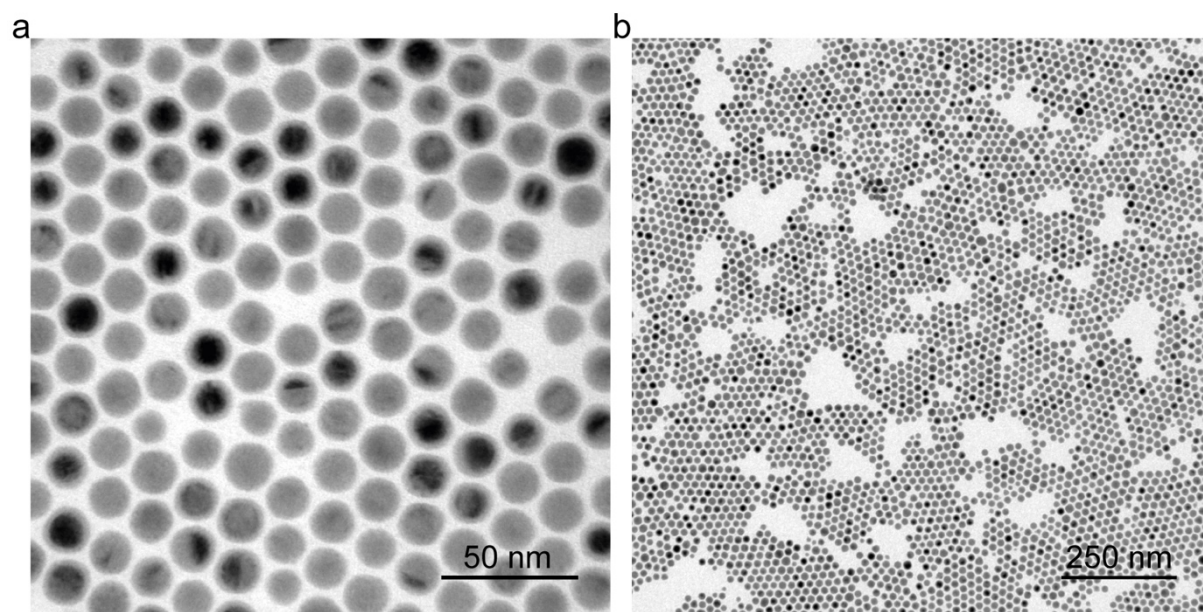


**Figure A3.1.** (a,b) Bright-field TEM images of the as-synthesized In NPs with a mean size of  $15 \pm 1$  nm.

**Table A3.2.** Experimental conditions and mean size for the synthesis of Cu-In NPs using 15 nm In NP templates. Corresponding TEM images are shown in **Figure 5.1**.

#	In NCs / mmol	Cu(OAc) <sub>2</sub> / mmol	OLAM / mL	OLAC / mL	reaction time / min	mean size / nm
c	0.004	0.006	0.5	0.5	30	$13 \pm 1$
d	0.004	0.006	0.5	0.5	60	$13 \pm 1$
e	0.004	0.006	0.5	0.5	120	$16 \pm 2$

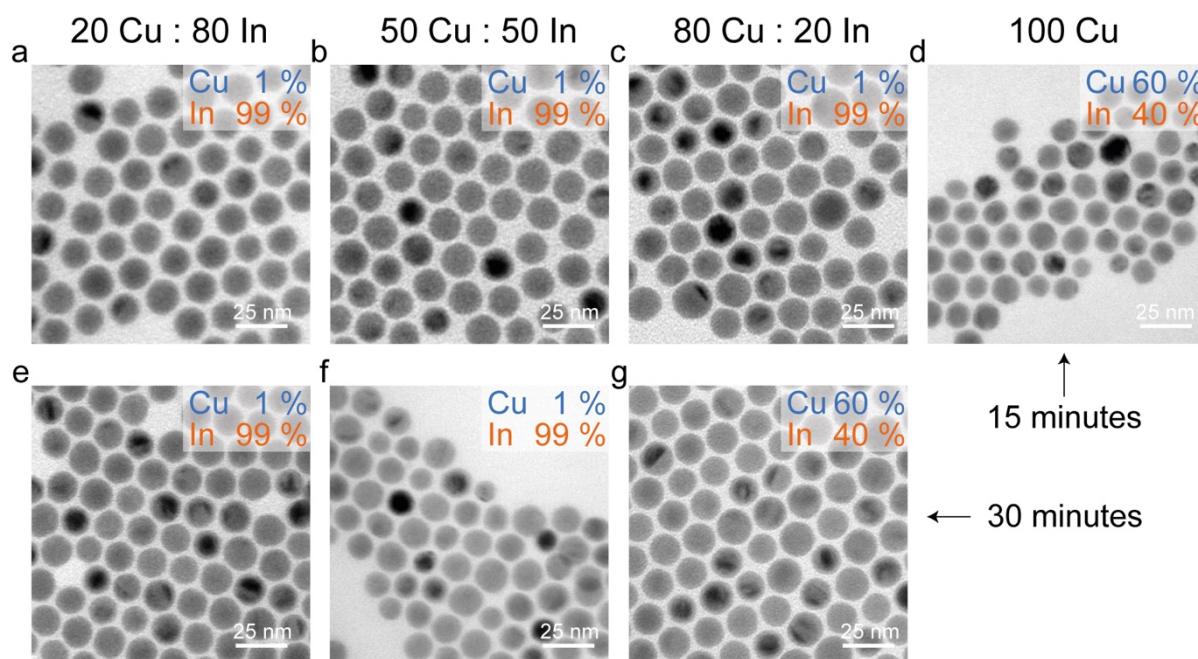


**Figure A3.2.** Bright-field TEM images of the as-synthesized Cu-In NPs after (a-d) 15 and (e-g) 30 minutes using different Cu:In ratios. Atomic percentage (%) content of the two metals in the final NPs as obtained from ICP quantification is reported for each sample.

**Table A3.3.** Experimental conditions and mean size for the synthesis of Cu-In NPs using 15 nm In NP templates with corresponding TEM images in **Figure A3.2**.

#	In NCs / mmol	Cu(OAc) <sub>2</sub> / mmol	OLAM / mL	OLAC / mL	reaction time / min	mean size / nm
a	0.004	0.0015	0.5	0.5	15	15 ± 1
b	0.004	0.003	0.5	0.5	15	15 ± 1
c	0.004	0.0045	0.5	0.5	15	15 ± 1
d	0.004	0.006	0.5	0.5	15	13 ± 1
e	0.004	0.0015	0.5	0.5	30	15 ± 1
f	0.004	0.003	0.5	0.5	30	14 ± 1
g	0.004	0.0045	0.5	0.5	30	14 ± 1

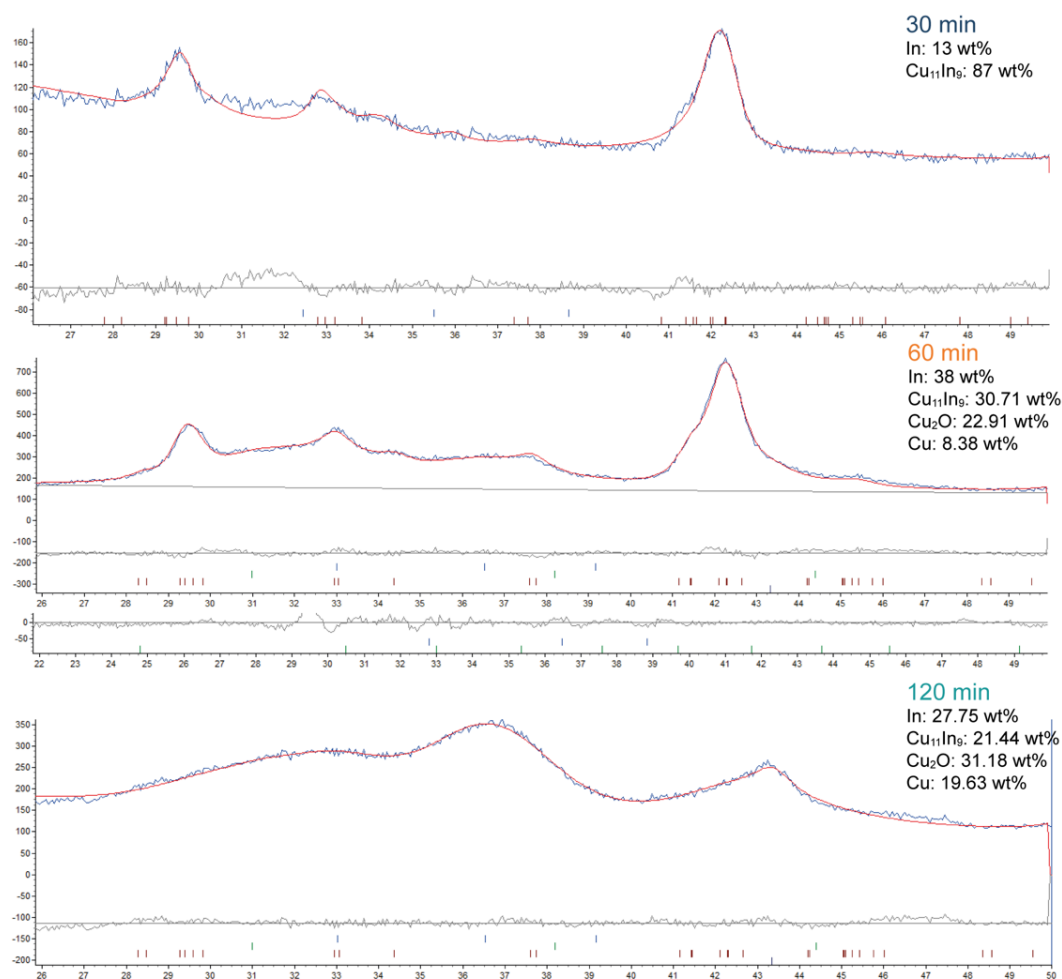


**Figure A3.3.** Rietveld analysis of the XRD patterns presented in **Figure 5.2** of the Cu-In NPs after 0 (initial In NPs), 30, 60 and 120 minutes of reaction. Standards patterns of In (PDF 00-005-0642), In<sub>2</sub>O<sub>3</sub> (PDF 00-006-0416), Cu<sub>11</sub>In<sub>9</sub> (PDF 00-041-0883), Cu (PDF 00-004-0836) and Cu<sub>2</sub>O (PDF 01-078-2076) were used.

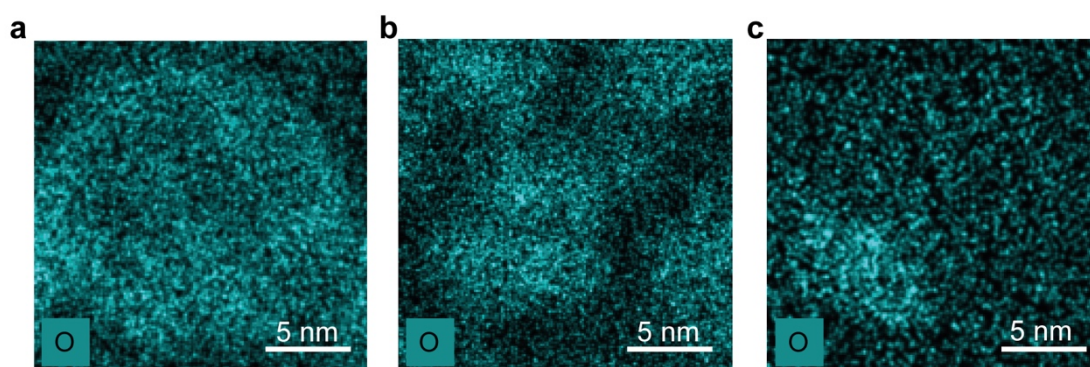


**Figure A3.4.** Oxygen STEM-EDX elemental mapping of (a) **Figure 5.2b**, (b) **Figure 5.2d** and (c) **Figure 5.2f**.

These data evidence higher oxygen content in correspondence of the In domain, which is consistent with the higher oxophilicity of this metal compared to Cu. As the synthesis is performed under inert atmosphere, it is reasonable to assume that such surface oxidation occurs during sample washing and following manipulation.

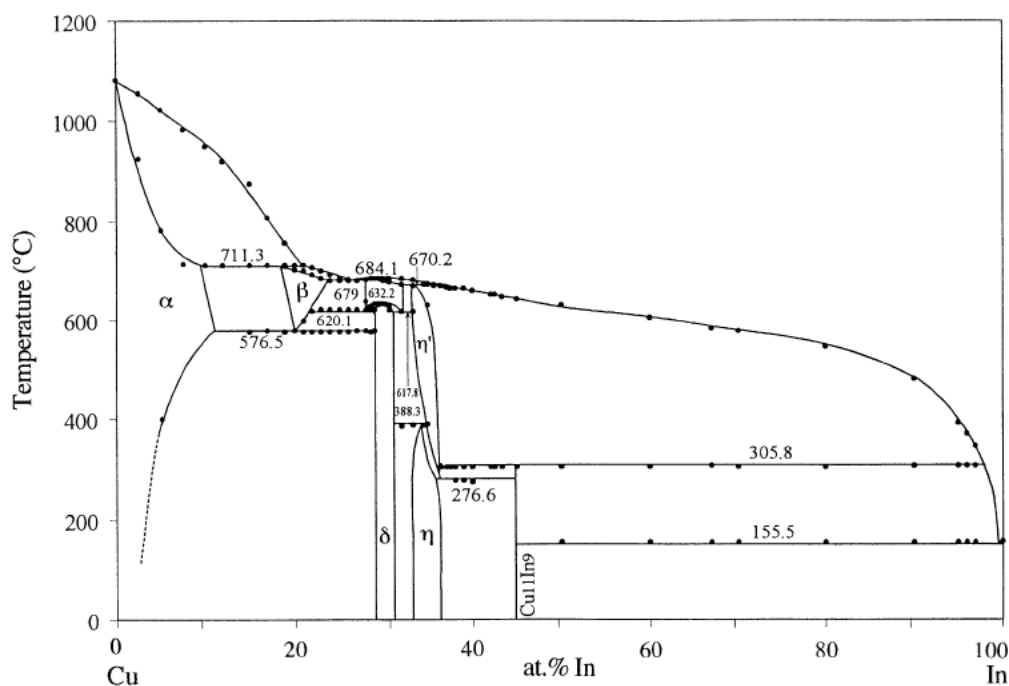


**Figure A3.5.** Phase diagram of the Cu-In system according to Dugué and coworkers.<sup>290</sup>

We note that the bulk phase diagram indicates the existence of other CuIn intermetallic phases for Cu content above 50 at. %, which were never isolated in the GRR between In NPs and the Cu molecular precursor, independently from the In NP size. It can be speculated that the formation energy of these phases is higher compared to that required to form Cu<sub>11</sub>In<sub>9</sub> because of additional structural changes associated with them.<sup>314,315</sup> Probably, higher reaction temperatures might facilitate their formation. However, higher reaction temperatures are not accessible in the present GRR approach (see **Figure A3.10**).

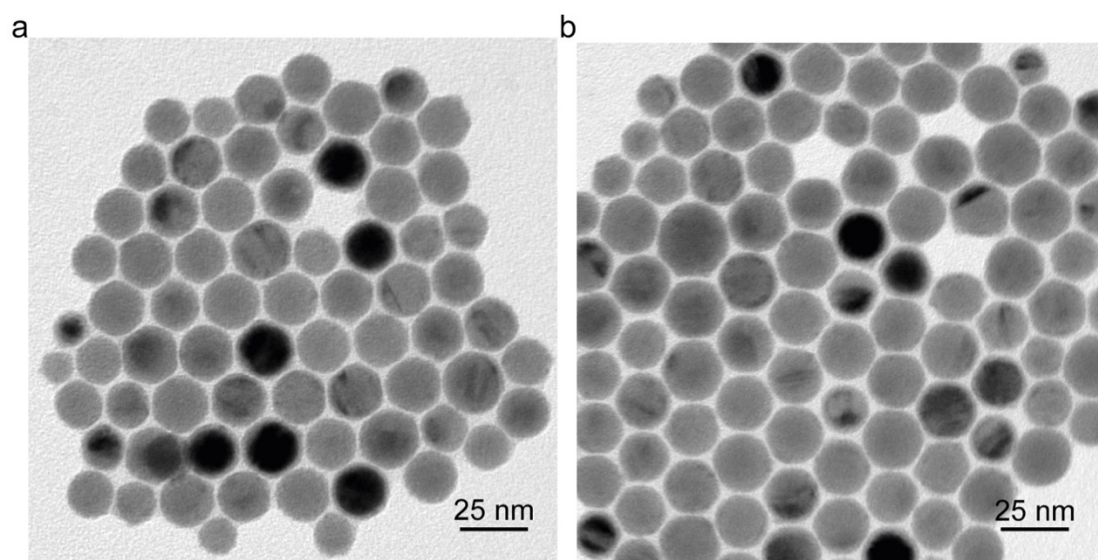


**Figure A3.6.** Bright-field TEM images of the as-synthesized In NPs of (a) 19 and (b) 22 nm, with mean sizes of  $19 \pm 2$  nm and  $22 \pm 3$  nm respectively.

**Table A3.4.** Experimental conditions and mean size for the synthesis of Cu-In NPs using (a-h) 19 nm and (h-p) 22 nm In NP seeds. Corresponding TEM images are shown in **Figure A3.7** below. Rows in bold correspond to the experiments shown in **Figure 5.3** in the same order of apparition.

#	In NCs / mmol	Cu(OAc) <sub>2</sub> / mmol	OLAM / mL	OLAC / mL	reaction time / min	mean size / nm
<b>a</b>	<b>0.004</b>	<b>0.0015</b>	<b>0.5</b>	<b>0.5</b>	<b>30</b>	<b>17 ± 2</b>
<b>b</b>	<b>0.004</b>	<b>0.003</b>	<b>0.5</b>	<b>0.5</b>	<b>30</b>	<b>19 ± 4</b>
c	0.004	0.0045	0.5	0.5	30	19 ± 3
<b>d</b>	<b>0.004</b>	<b>0.006</b>	<b>0.5</b>	<b>0.5</b>	<b>30</b>	<b>19 ± 2</b>
e	0.004	0.0015	0.5	0.5	60	14 ± 2
f	0.004	0.003	0.5	0.5	60	17 ± 3
g	0.004	0.0045	0.5	0.5	60	19 ± 2
h	0.004	0.006	0.5	0.5	60	20 ± 3
<b>i</b>	<b>0.004</b>	<b>0.0015</b>	<b>0.5</b>	<b>0.5</b>	<b>30</b>	<b>20 ± 3</b>
j	0.004	0.003	0.5	0.5	30	19 ± 3
k	0.004	0.0045	0.5	0.5	30	22 ± 4
<b>l</b>	<b>0.004</b>	<b>0.006</b>	<b>0.5</b>	<b>0.5</b>	<b>30</b>	<b>24 ± 3</b>
m	0.004	0.0015	0.5	0.5	60	18 ± 3
n	0.004	0.003	0.5	0.5	60	20 ± 4
o	0.004	0.0045	0.5	0.5	60	21 ± 4
<b>p</b>	<b>0.004</b>	<b>0.006</b>	<b>0.5</b>	<b>0.5</b>	<b>60</b>	<b>24 ± 6</b>



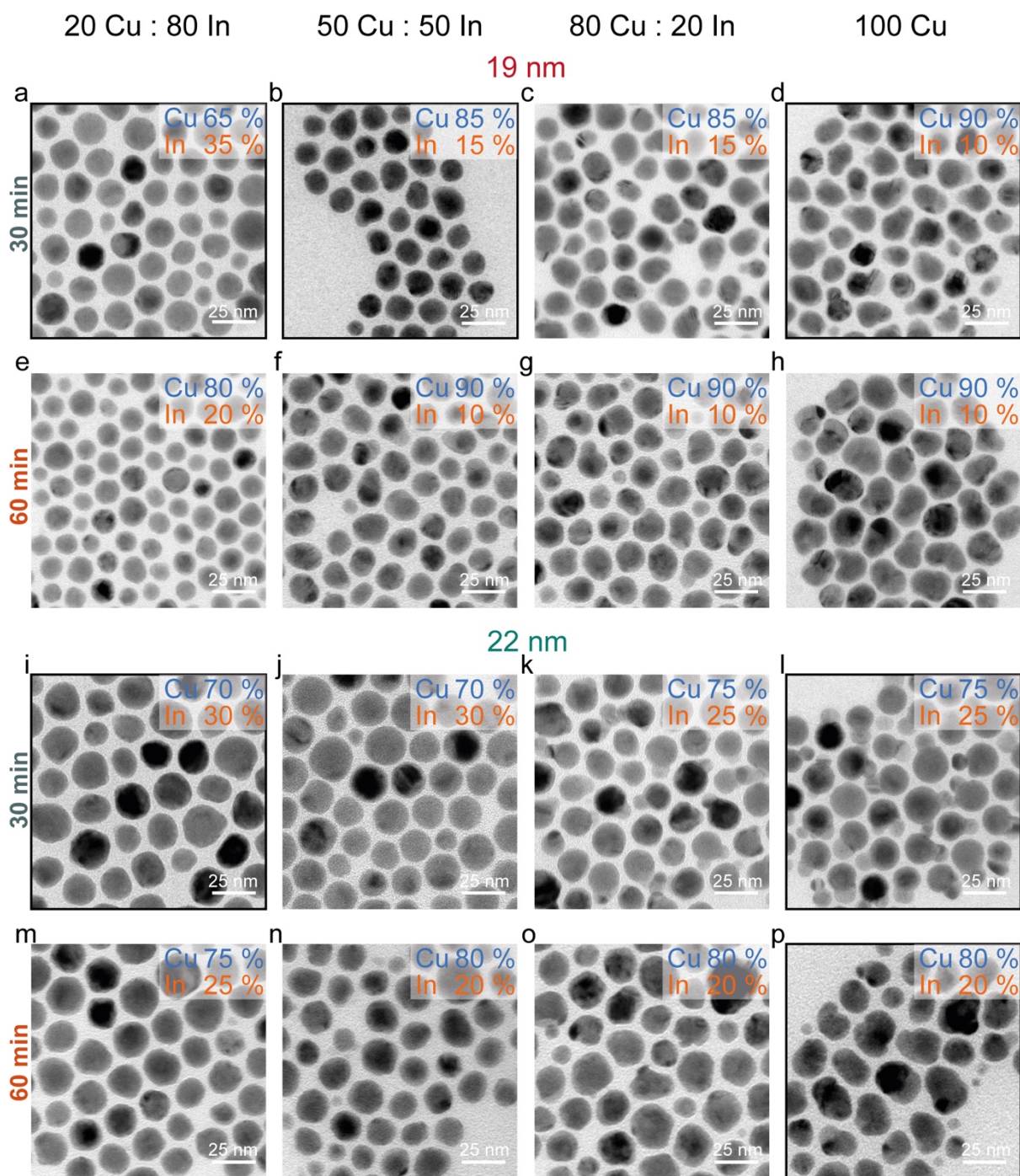


**Figure A3.7.** Bright-field TEM images of the as-synthesized Cu-In19 NPs after (a-d) 30 and (e-h) 60 minutes using different amounts of Cu precursor (i-p) and the equivalent pictures for the Cu-In22 NPs. The corresponding aimed final ratios are on top of the figure, more details in **Table A3.4** above. Images include the elemental quantification for each sample as measured by elemental ICP-OES. Images in bold correspond to the experiments shown in **Figure 5.3** in the same order of apparition.

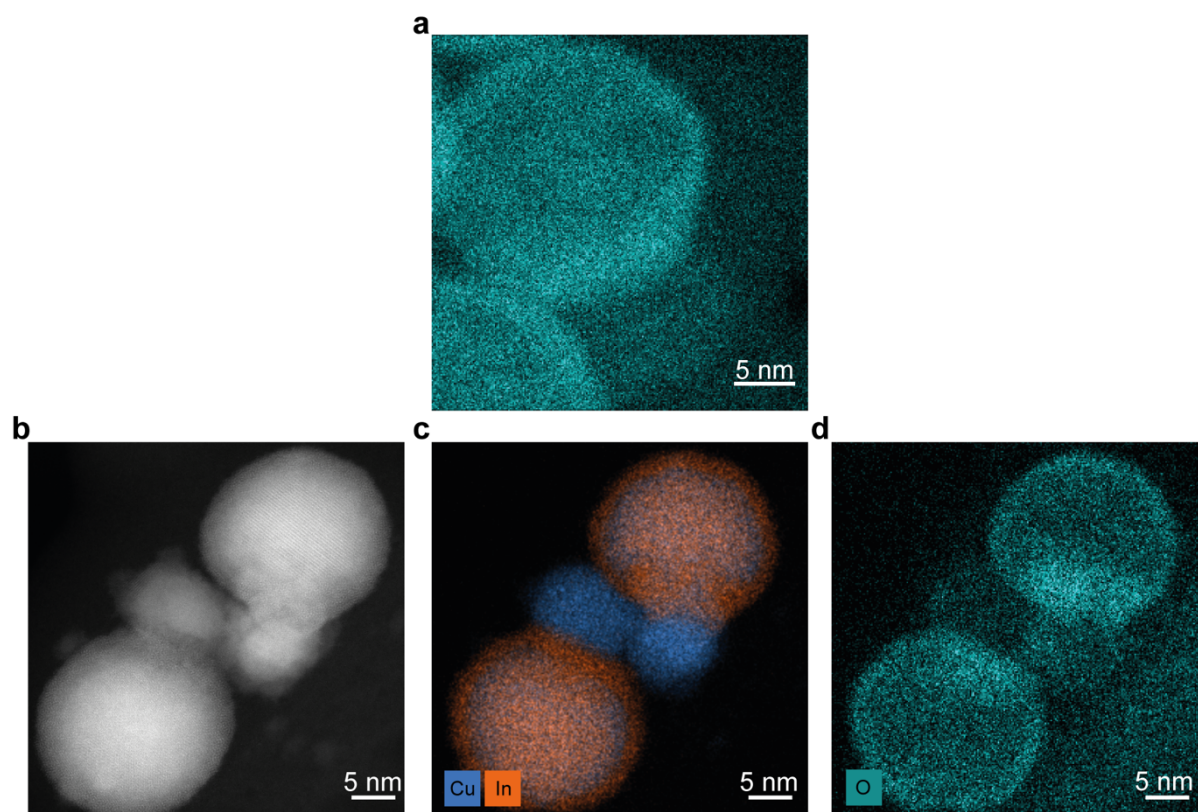


**Figure A3.8.** (a) Oxygen STEM-EDX elemental mapping of the same dimer reported in **Figures 5.4b,c**; (b-d) atomic resolution HAADF-STEM and their corresponding STEM-EDX elemental mapping of two additional dimers.

Similarly to **Figure A3.4**, the oxygen signal is more intense in correspondence of the In domain.

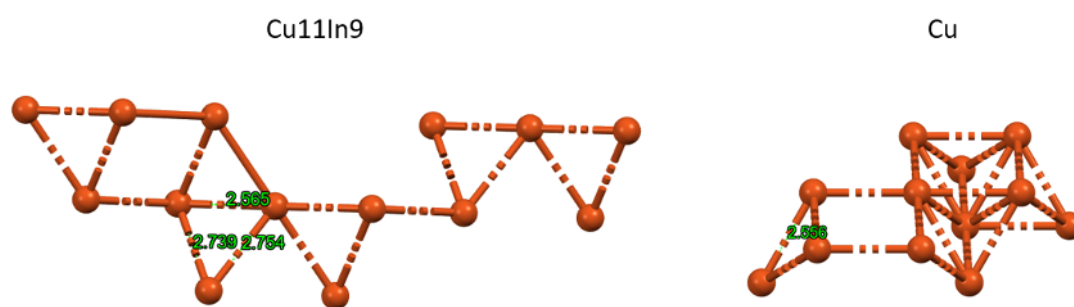


**Figure A3.9.** Images illustrating the Cu substructure of the monoclinic  $\text{Cu}_{11}\text{In}_9$  intermetallic phase (left) and the fcc-Cu structure (right). No real structural relationship can be identified, except the highlighted fragments where the Cu-Cu distance in the fcc-Cu is still 6% larger than the Cu-Cu distance in the intermetallic phase.



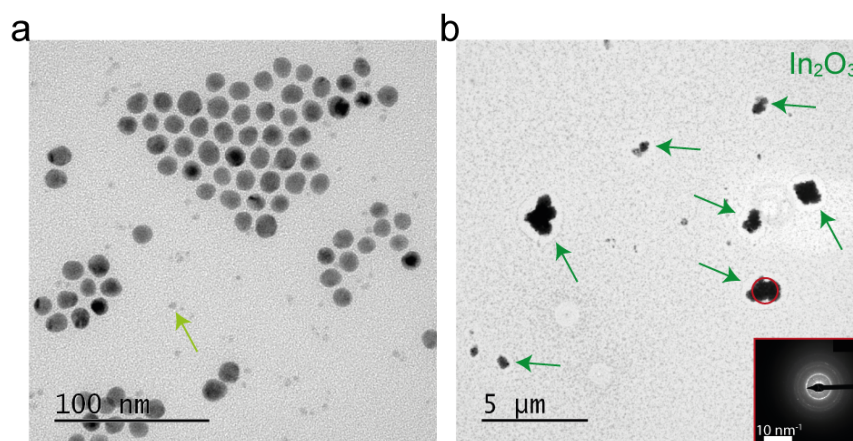


**Figure A3.10.** Bright-field TEM images of the as-synthesized Cu-In15 NPs after 30 min of reaction at 180 °C with precursor ratio set at 0.004 mmol of In and 0.006 mmol of Cu. The composition ratio from ICP elemental analysis was determined to be 70 at.% Cu and 30 at.% In. This composition includes oxide debris (green arrow in (a)) and agglomerates of crystalline  $\text{In}_2\text{O}_3$  NPs (green arrow in (b)). A standard pattern of  $\text{In}_2\text{O}_3$  (PDF 00-006-0416) was used to verify their composition by Selected area electron diffraction (SAED) experiments of the area inside the red circle.

The melting temperature of bulk In is 156.6 °C. Melting point depression at increasing surface-to-volume ratios might cause the particles to be liquid at temperatures below the bulk melting point.<sup>308,316–318</sup> However, capping ligands can counteract this trend as they stabilize the surface.<sup>240,308</sup> One study on In NPs synthesized following the same procedure of this work has shown that, upon ligand stripping, In NPs with diameters between 15 nm and 20 nm, which is the same size regime of those used in this work, possess a melting temperature between 140 °C and 150 °C, thus lower than the 156.6 °C for bulk.<sup>319</sup> The authors also show that the presence of the native ligands raise these values up of at least 10 °C.<sup>308</sup>

As described in the Chapter 2, the GRR reaction temperature is set up at 160 °C on the hot-plate, with the temperature in solution being 128 °C on average. This temperature is below the melting point measured for the un-capped In NPs in a similar size regime.<sup>308</sup> Thus, it is reasonable to assume that the In NPs are in their solid state during the GRR. This assumption might not be valid anymore at 180 °C, which can explain the completely different outcome of the reaction in **Figure A3.10**. Future studies will focus on this intriguing temperature-dependent reactivity of metals with low melting points.

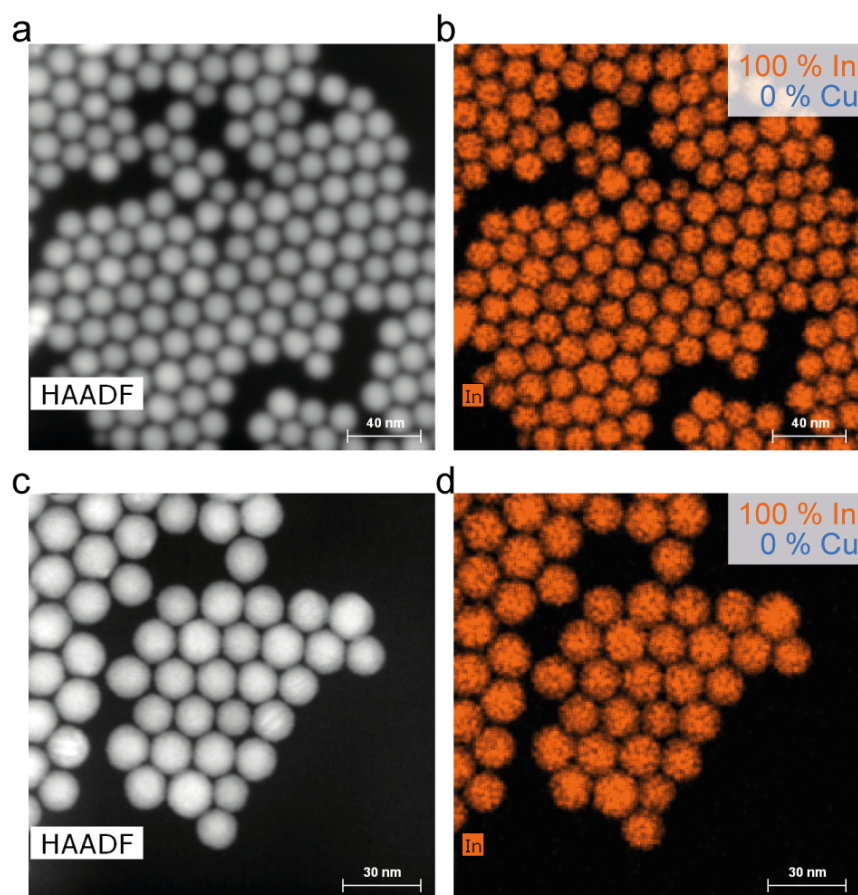


**Figure A3.11.** HAADF-STEM images and corresponding STEM-EDXS mapping of the as-synthesized Cu-In15 NPs after 60 min of reaction at (a,b) 80 °C and (c,d) 140 °C, with precursor ratio set at 0.004 mmol of In and 0.006 mmol of Cu. The STEM EDXS maps include the elemental quantification for each sample as measured by elemental ICP-OES and EDX and was determined to be 0 at. % Cu and 100 at. % In in both cases.

## References

- (1) Hori, Y.; Kikuchi, K.; Suzuki, S. Production of CO and CH<sub>4</sub> in Electrochemical Reduction of CO<sub>2</sub> at Metal Electrodes in Aqueous Hydrogencarbonate Solution. *Chem. Lett.* **1985**, *14*, 1695–1698.
- (2) Götz, M.; Lefebvre, J.; Mörs, F.; McDaniel Koch, A.; Graf, F.; Bajohr, S.; Reimert, R.; Kolb, T. Renewable Power-to-Gas: A Technological and Economic Review. *Renew. Energy* **2016**, *85*, 1371–1390.
- (3) Nitopi, S.; Bertheussen, E.; Scott, S. B.; Liu, X.; Engstfeld, A. K.; Horch, S.; Seger, B.; Stephens, I. E. L.; Chan, K.; Hahn, C.; et al. Progress and Perspectives of Electrochemical CO<sub>2</sub> Reduction on Copper in Aqueous Electrolyte. *Chem. Rev.* **2019**, *119*, 7610–7672.
- (4) Hori, Y.; Wakebe, H.; Tsukamoto, T.; Koga, O. Electrocatalytic Process of CO Selectivity in Electrochemical Reduction of CO<sub>2</sub> at Metal Electrodes in Aqueous Media. *Electrochim. Acta* **1994**, *39*, 1833–1839.
- (5) Hori, Y.; Takahashi, I.; Koga, O.; Hoshi, N. Electrochemical Reduction of Carbon Dioxide at Various Series of Copper Single Crystal Electrodes. *J. Mol. Catal. A Chem.* **2003**, *199*, 39–47.
- (6) Liu, X.; Xiao, J.; Peng, H.; Hong, X.; Chan, K.; Nørskov, J. K. Understanding Trends in Electrochemical Carbon Dioxide Reduction Rates. *Nat. Commun.* **2017**, *8*, 1–7.
- (7) Kuhl, K. P.; Cave, E. R.; Abram, D. N.; Jaramillo, T. F. New Insights into the Electrochemical Reduction of Carbon Dioxide on Metallic Copper Surfaces. *Energy Environ. Sci.* **2012**, *5*, 7050–7059.
- (8) Kim, C.; Dionigi, F.; Beermann, V.; Wang, X.; Möller, T.; Strasser, P. Alloy Nanocatalysts for the Electrochemical Oxygen Reduction (ORR) and the Direct Electrochemical Carbon Dioxide Reduction Reaction (CO<sub>2</sub>RR). *Adv. Mater.* **2019**, *31*, 1805617.
- (9) Zaza, L.; Rossi, K.; Buonsanti, R. Well-Defined Copper-Based Nanocatalysts for Selective Electrochemical Reduction of CO<sub>2</sub> to C<sub>2</sub> Products. *ACS Energy Lett.* **2022**, *7*, 1284–1291.
- (10) Karapinar, D.; Creissen, C. E.; Rivera De La Cruz, J. G.; Schreiber, M. W.; Fontecave, M. Electrochemical CO<sub>2</sub> Reduction to Ethanol with Copper-Based Catalysts. *ACS Energy Lett.* **2021**, *6*, 694–706.

- 
- (11) Ren, D.; Gao, J.; Pan, L.; Wang, Z.; Luo, J.; Zakeeruddin, S. M.; Hagfeldt, A.; Grätzel, M. Atomic Layer Deposition of ZnO on CuO Enables Selective and Efficient Electroreduction of Carbon Dioxide to Liquid Fuels. *Angew. Chemie - Int. Ed.* **2019**, *58*, 15036–15040.
- (12) Jeon, H. S.; Timoshenko, J.; Scholten, F.; Sinev, I.; Herzog, A.; Haase, F. T.; Cuenya, B. R. Operando Insight into the Correlation between the Structure and Composition of CuZn Nanoparticles and Their Selectivity for the Electrochemical CO<sub>2</sub> Reduction. *J. Am. Chem. Soc.* **2019**, *141*, 19879–19887.
- (13) Lum, Y.; Ager, J. W. Sequential Catalysis Controls Selectivity in Electrochemical CO<sub>2</sub> Reduction on Cu. *Energy Environ. Sci.* **2018**, *11*, 2935–2944.
- (14) Clark, E. L.; Hahn, C.; Jaramillo, T. F.; Bell, A. T. Electrochemical CO<sub>2</sub> Reduction over Compressively Strained CuAg Surface Alloys with Enhanced Multi-Carbon Oxygenate Selectivity. *J. Am. Chem. Soc.* **2017**, *139*, 15848–15857.
- (15) Ren, D.; Ang, B. S. H.; Yeo, B. S. Tuning the Selectivity of Carbon Dioxide Electroreduction toward Ethanol on Oxide-Derived Cu<sub>x</sub>Zn Catalysts. *ACS Catal.* **2016**, *6*, 8239–8247.
- (16) Kim, D.; Resasco, J.; Yu, Y.; Asiri, A. M.; Yang, P. Synergistic Geometric and Electronic Effects for Electrochemical Reduction of Carbon Dioxide Using Gold-Copper Bimetallic Nanoparticles. *Nat. Commun.* **2014**, *5*, 1–8.
- (17) Huang, J.; Mensi, M.; Oveisi, E.; Mantella, V.; Buonsanti, R. Structural Sensitivities in Bimetallic Catalysts for Electrochemical CO<sub>2</sub> Reduction Revealed by Ag–Cu Nanodimers. *J. Am. Chem. Soc.* **2019**, *141*, 2490–2499.
- (18) Ma, S.; Sadakiyo, M.; Heim, M.; Luo, R.; Haasch, R. T.; Gold, J. I.; Yamauchi, M.; Kenis, P. J. A. Electroreduction of Carbon Dioxide to Hydrocarbons Using Bimetallic Cu-Pd Catalysts with Different Mixing Patterns. *J. Am. Chem. Soc.* **2017**, *139*, 47–50.
- (19) Huang, J.; Mensi, M.; Oveisi, E.; Mantella, V.; Buonsanti, R. Structural Sensitivities in Bimetallic Catalysts for Electrochemical CO<sub>2</sub> Reduction Revealed by Ag–Cu Nanodimers. *J. Am. Chem. Soc.* **2019**, *141*, 2490–2499.
- (20) Varandili, S. B.; Stoian, D.; Vavra, J.; Rossi, K.; Pankhurst, J. R.; Guntern, Y. T.; López, N.; Buonsanti, R. Elucidating the Structure-Dependent Selectivity of CuZn towards Methane and Ethanol in CO<sub>2</sub> electroreduction Using Tailored Cu/ZnO Precatalysts. *Chem. Sci.* **2021**, *12*, 14484–14493.
- (21) Tran, K.; Ulissi, Z. W. Active Learning across Intermetallics to Guide Discovery of Electrocatalysts for CO<sub>2</sub> Reduction and H<sub>2</sub> Evolution. *Nat. Catal.* **2018**, *1*, 696–703.

- 
- (22) Pedersen, J. K.; Batchelor, T. A. A.; Bagger, A.; Rossmeisl, J. High-Entropy Alloys as Catalysts for the CO<sub>2</sub> and CO Reduction Reactions. *ACS Catal.* **2020**, *10*, 2169–2176.
- (23) Rasul, S.; Anjum, D. H.; Jedidi, A.; Minenkov, Y.; Cavallo, L.; Takanabe, K. A Highly Selective Copper-Indium Bimetallic Electrocatalyst for the Electrochemical Reduction of Aqueous CO<sub>2</sub> to CO. *Angew. Chemie - Int. Ed.* **2015**, *54*, 2146–2150.
- (24) Luo, W.; Xie, W.; Mutschler, R.; Oveisi, E.; De Gregorio, G. L.; Buonsanti, R.; Züttel, A. Selective and Stable Electroreduction of CO<sub>2</sub> to CO at the Copper/Indium Interface. *ACS Catal.* **2018**, *8*, 6571–6581.
- (25) Jang, Y. J.; Lee, J.; Kim, J. H.; Lee, B. J.; Lee, J. S. One-Dimensional CuIn Alloy Nanowires as a Robust and Efficient Electrocatalyst for Selective CO<sub>2</sub>-to-CO Conversion. *J. Power Sources* **2018**, *378*, 412–417.
- (26) Wan, W.-B.; Dai, T.-Y.; Shi, H.; Zeng, S.-P.; Wen, Z.; Zhang, W.; Lang, X.-Y.; Jiang, Q. Intermetallic Cu<sub>11</sub>In<sub>9</sub> in Situ Formed on Hierarchical Nanoporous Cu for Highly Selective CO<sub>2</sub> Electroreduction. *J. Mater. Chem. A* **2022**, *10*, 4333–4343.
- (27) Xiang, H.; Rasul, S.; Hou, B.; Portoles, J.; Cumpson, P.; Yu, E. H. Copper-Indium Binary Catalyst on a Gas Diffusion Electrode for High-Performance CO<sub>2</sub> Electrochemical Reduction with Record CO Production Efficiency. *ACS Appl. Mater. Interfaces* **2020**, *12*, 601–608.
- (28) Xie, Q.; Larrazábal, G. O.; Ma, M.; Chorkendorff, I.; Seger, B.; Luo, J. Copper-Indium Hydroxides Derived Electrocatalysts with Tunable Compositions for Electrochemical CO<sub>2</sub> Reduction. *J. Energy Chem.* **2021**, *63*, 278–284.
- (29) Larrazábal, G. O.; Shinagawa, T.; Martín, A. J.; Pérez-Ramírez, J. Microfabricated Electrodes Unravel the Role of Interfaces in Multicomponent Copper-Based CO<sub>2</sub> Reduction Catalysts. *Nat. Commun.* **2018**, *9*, 1–10.
- (30) Gao, J.; Song, F.; Li, Y.; Cheng, W.; Yuan, H.; Xu, Q. Cu<sub>2</sub>In Nanoalloy Enhanced Performance of Cu/ZrO<sub>2</sub> Catalysts for the CO<sub>2</sub> Hydrogenation to Methanol. *Ind. Eng. Chem. Res.* **2020**, *59*, 12331–12337.
- (31) Shi, Z.; Tan, Q.; Tian, C.; Pan, Y.; Sun, X.; Zhang, J.; Wu, D. CO<sub>2</sub> Hydrogenation to Methanol over Cu-In Intermetallic Catalysts: Effect of Reduction Temperature. *J. Catal.* **2019**, *379*, 78–89.
- (32) Rahaman, M.; Andrei, V.; Pornrungrroj, C.; Wright, D.; Baumberg, J. J.; Reisner, E. Selective CO Production from Aqueous CO<sub>2</sub> using a Cu<sub>96</sub>In<sub>4</sub> catalyst and Its Integration into a Bias-Free Solar Perovskite-BiVO<sub>4</sub> tandem Device. *Energy Environ. Sci.* **2020**, *13*, 3536–3543.

- 
- (33) Larrazábal, G. O.; Martín, A. J.; Mitchell, S.; Hauert, R.; Pérez-Ramírez, J. Enhanced Reduction of CO<sub>2</sub> to CO over Cu-In Electrocatalysts: Catalyst Evolution Is the Key. *ACS Catal.* **2016**, *6*, 6265–6274.
- (34) Yan, Y.; Du, J. S.; Gilroy, K. D.; Yang, D.; Xia, Y.; Zhang, H. Intermetallic Nanocrystals: Syntheses and Catalytic Applications. *Adv. Mater.* **2017**, *29*, 1605997.
- (35) Gilroy, K. D.; Ruditskiy, A.; Peng, H. C.; Qin, D.; Xia, Y. Bimetallic Nanocrystals: Syntheses, Properties, and Applications. *Chem. Rev.* **2016**, *116*, 10414–10472.
- (36) Kahraman, M.; Aydin, Ö.; Çulha, M. Oligonucleotide-Mediated Au-Ag Core-Shell Nanoparticles. *Plasmonics* **2009**, *4*, 293–301.
- (37) Tsao, Y. C.; Rej, S.; Chiu, C. Y.; Huang, M. H. Aqueous Phase Synthesis of Au-Ag Core-Shell Nanocrystals with Tunable Shapes and Their Optical and Catalytic Properties. *J. Am. Chem. Soc.* **2014**, *136*, 396–404.
- (38) Cortie, M. B.; McDonagh, A. M. Synthesis and Optical Properties of Hybrid and Alloy Plasmonic Nanoparticles. *Chem. Rev.* **2011**, *111*, 3713–3735.
- (39) Ma, Y.; Li, W.; Cho, E. C.; Li, Z.; Yu, T.; Zeng, J.; Xie, Z.; Xia, Y. Au@Ag Core-Shell Nanocubes with Finely Tuned and Well-Controlled Sizes, Shell Thicknesses, and Optical Properties. *ACS Nano* **2010**, *4*, 6725–6734.
- (40) Zhou, M.; Li, C.; Fang, J. Noble-Metal Based Random Alloy and Intermetallic Nanocrystals: Syntheses and Applications. *Chem. Rev.* **2021**, *121*, 736–795.
- (41) He, M.; Protesescu, L.; Caputo, R.; Krumeich, F.; Kovalenko, M. V. A General Synthesis Strategy for Monodisperse Metallic and Metalloid Nanoparticles (In, Ga, Bi, Sb, Zn, Cu, Sn, and Their Alloys) via in Situ Formed Metal Long-Chain Amides. *Chem. Mater.* **2015**, *27*, 635–647.
- (42) Castilla-Amorós, L.; Stoian, D.; Pankhurst, J. R.; Varandili, S. B.; Buonsanti, R. Exploring the Chemical Reactivity of Gallium Liquid Metal Nanoparticles in Galvanic Replacement. *J. Am. Chem. Soc.* **2020**, *142*, 19283–19290.
- (43) Clarysse, J.; Moser, A.; Yarema, O.; Wood, V.; Yarema, M. Size- and Composition-Controlled Intermetallic Nanocrystals via Amalgamation Seeded Growth. *Sci. Adv.* **2021**, *7*, eabg1934.
- (44) Kwon, S. G.; Krylova, G.; Phillips, P. J.; Klie, R. F.; Chattopadhyay, S.; Shibata, T.; Bunel, E. E.; Liu, Y.; Prakapenka, V. B.; Lee, B.; et al. Heterogeneous Nucleation and Shape Transformation of Multicomponent Metallic Nanostructures. *Nat. Mater.* **2015**, *14*, 215–223.
- (45) Eikey, E. A.; Gan, X. Y.; Kaseman, D. C.; Murphey, C. G. E.; Crawford, S. E.; Johnston,

- K. A.; Yazdi, S.; Millstone, J. E. Efficient Control of Atom Arrangement in Ternary Metal Chalcogenide Nanoparticles Using Precursor Oxidation State. *Chem. Mater.* **2020**, *32*, 1322–1331.
- (46) Osowiecki, W. T.; Ye, X.; Satish, P.; Bustillo, K. C.; Clark, E. L.; Alivisatos, A. P. Tailoring Morphology of Cu-Ag Nanocrescents and Core-Shell Nanocrystals Guided by a Thermodynamic Model. *J. Am. Chem. Soc.* **2018**, *140*, 8569–8577.
- (47) Hodges, J. M.; Morse, J. R.; Williams, M. E.; Schaak, R. E. Microscopic Investigation of Chemoselectivity in Ag-Pt-Fe<sub>3</sub>O<sub>4</sub> Heterotrimer Formation: Mechanistic Insights and Implications for Controlling High-Order Hybrid Nanoparticle Morphology. *J. Am. Chem. Soc.* **2015**, *137*, 15493–15500.
- (48) Chen, P. C.; Gao, M.; Yu, S.; Jin, J.; Song, C.; Salmeron, M.; Scott, M. C.; Yang, P. Revealing the Phase Separation Behavior of Thermodynamically Immiscible Elements in a Nanoparticle. *Nano Lett.* **2021**, *21*, 6684–6689.
- (49) Vollath, D.; Fischer, F. D.; Holec, D. Surface Energy of Nanoparticles - Influence of Particle Size and Structure. *Beilstein J. Nanotechnol.* **2018**, *9*, 2265–2276.
- (50) Yang, C.; Ko, B. H.; Hwang, S.; Liu, Z.; Yao, Y.; Luc, W.; Cui, M.; Malkani, A. S.; Li, T.; Wang, X.; et al. Overcoming Immiscibility toward Bimetallic Catalyst Library. *Sci. Adv.* **2020**, *6*, eaaz6844.
- (51) Pohl, J.; Stahl, C.; Albe, K. Size-Dependent Phase Diagrams of Metallic Alloys: A Monte Carlo Simulation Study on Order-Disorder Transitions in Pt-Rh Nanoparticles. *Beilstein J. Nanotechnol.* **2012**, *3*, 1–11.
- (52) Feng, J.; Chen, D.; Pikhitsa, P. V.; Jung, Y. ho; Yang, J.; Choi, M. Unconventional Alloys Confined in Nanoparticles: Building Blocks for New Matter. *Matter* **2020**, *3*, 1646–1663.
- (53) Zeng, J.; Zhu, C.; Tao, J.; Jin, M.; Zhang, H.; Li, Z. Y.; Zhu, Y.; Xia, Y. Controlling the Nucleation and Growth of Silver on Palladium Nanocubes by Manipulating the Reaction Kinetics. *Angew. Chemie - Int. Ed.* **2012**, *51*, 2354–2358.
- (54) Castilla-Amorós, L.; Chien, T. C. C.; Pankhurst, J. R.; Buonsanti, R. Modulating the Reactivity of Liquid Ga Nanoparticle Inks by Modifying Their Surface Chemistry. *J. Am. Chem. Soc.* **2022**, *144*, 1993–2001.
- (55) Kunz, M. R.; McClain, S. M.; Chen, D. P.; Koczur, K. M.; Weiner, R. G.; Skrabalak, S. E. Seed-Mediated Co-Reduction in a Large Lattice Mismatch System: Synthesis of Pd-Cu Nanostructures. *Nanoscale* **2017**, *9*, 7570–7576.
- (56) Chen, A. N.; Scanlan, M. M.; Skrabalak, S. E. Surface Passivation and Supersaturation:

- Strategies for Regioselective Deposition in Seeded Syntheses. *ACS Nano* **2017**, *11*, 12624–12631.
- (57) Desantis, C. J.; Skrabalak, S. E. Size-Controlled Synthesis of Au/Pd Octopods with High Refractive Index Sensitivity. *Langmuir* **2012**, *28*, 9055–9062.
- (58) Ortiz, N.; Skrabalak, S. E. Controlling the Growth Kinetics of Nanocrystals via Galvanic Replacement: Synthesis of Au Tetrapods and Star-Shaped Decahedra. *Cryst. Growth Des.* **2011**, *11*, 3545–3550.
- (59) Quintanilla, M.; Kuttner, C.; Smith, J. D.; Seifert, A.; Skrabalak, S. E.; Liz-Marzán, L. M. Heat Generation by Branched Au/Pd Nanocrystals: Influence of Morphology and Composition. *Nanoscale* **2019**, *11*, 19561–19570.
- (60) Mantella, V.; Castilla-Amorós, L.; Buonsanti, R. Shaping Non-Noble Metal Nanocrystals: Via Colloidal Chemistry. *Chem. Sci.* **2020**, *11*, 11394–11403.
- (61) Rodrigues, T. S.; Zhao, M.; Yang, T. H.; Gilroy, K. D.; da Silva, A. G. M.; Camargo, P. H. C.; Xia, Y. Synthesis of Colloidal Metal Nanocrystals: A Comprehensive Review on the Reductants. *Chem. - A Eur. J.* **2018**, *24*, 16944–16963.
- (62) Luo, M.; Ruditskiy, A.; Peng, H. C.; Tao, J.; Figueroa-Cosme, L.; He, Z.; Xia, Y. Penta-Twinned Copper Nanorods: Facile Synthesis via Seed-Mediated Growth and Their Tunable Plasmonic Properties. *Adv. Funct. Mater.* **2016**, *26*, 1209–1216.
- (63) Pastoriza-Santos, I.; Sánchez-Iglesias, A.; Rodríguez-González, B.; Liz-Marzán, L. M. Aerobic Synthesis of Cu Nanoplates with Intense Plasmon Resonances. *Small* **2009**, *5*, 440–443.
- (64) Wang, Z.; Yang, G.; Zhang, Z.; Jin, M.; Yin, Y. Selectivity on Etching: Creation of High-Energy Facets on Copper Nanocrystals for CO<sub>2</sub> Electrochemical Reduction. *ACS Nano* **2016**, *10*, 4559–4564.
- (65) Wang, Z.; Chen, Z.; Zhang, H.; Zhang, Z.; Wu, H.; Jin, M.; Wu, C.; Yang, D.; Yin, Y. Lattice-Mismatch-Induced Twinning for Seeded Growth of Anisotropic Nanostructures. *ACS Nano* **2015**, *9*, 3307–3313.
- (66) Ye, S.; Rathmell, A. R.; Stewart, I. E.; Ha, Y. C.; Wilson, A. R.; Chen, Z.; Wiley, B. J. A Rapid Synthesis of High Aspect Ratio Copper Nanowires for High-Performance Transparent Conducting Films. *Chem. Commun.* **2014**, *50*, 2562–2564.
- (67) Rathmell, A. R.; Bergin, S. M.; Hua, Y. L.; Li, Z. Y.; Wiley, B. J. The Growth Mechanism of Copper Nanowires and Their Properties in Flexible, Transparent Conducting Films. *Adv. Mater.* **2010**, *22*, 3558–3563.
- (68) Chang, Y.; Lye, M. L.; Zeng, H. C. Large-Scale Synthesis of High-Quality Ultralong



- Copper Nanowires. *Langmuir* **2005**, *21*, 3746–3748.
- (69) Jin, M.; He, G.; Zhang, H.; Zeng, J.; Xie, Z.; Xia, Y. Shape-Controlled Synthesis of Copper Nanocrystals in an Aqueous Solution with Glucose as a Reducing Agent and Hexadecylamine as a Capping Agent. *Angew. Chemie - Int. Ed.* **2011**, *50*, 10560–10564.
- (70) Wang, C.; Yin, H.; Chan, R.; Peng, S.; Dai, S.; Sun, S. One-Pot Synthesis of Oleylamine Coated AuAg Alloy NPs and Their Catalysis for CO Oxidation. *Chem. Mater.* **2009**, *21*, 433–435.
- (71) Liu, Y.; Chi, M.; Mazumder, V.; More, K. L.; Soled, S.; Henao, J. D.; Sun, S. Composition-Controlled Synthesis of Bimetallic PdPt Nanoparticles and Their Electro-Oxidation of Methanol. *Chem. Mater.* **2011**, *23*, 4199–4203.
- (72) Sra, A. K.; Schaak, R. E. Synthesis of Atomically Ordered AuCu and AuCu<sub>3</sub> Nanocrystals from Bimetallic Nanoparticle Precursors. *J. Am. Chem. Soc.* **2004**, *126*, 6667–6672.
- (73) Chi, M.; Wang, C.; Lei, Y.; Wang, G.; Li, D.; More, K. L.; Lupini, A.; Allard, L. F.; Markovic, N. M.; Stamenkovic, V. R. Surface Faceting and Elemental Diffusion Behaviour at Atomic Scale for Alloy Nanoparticles during in Situ Annealing. *Nat. Commun.* **2015**, *6*, 1–9.
- (74) Bondi, J. F.; Misra, R.; Ke, X.; Sines, I. T.; Schiffer, P.; Schaak, R. E. Optimized Synthesis and Magnetic Properties of Intermetallic Au<sub>3</sub>Fe<sub>1-x</sub>, Au<sub>3</sub>Co<sub>1-x</sub>, and Au<sub>3</sub>Ni<sub>1-x</sub> Nanoparticles. *Chem. Mater.* **2010**, *22*, 3988–3994.
- (75) Vasquez, Y.; Luo, Z.; Schaak, R. E.; Park, U. V.; Pennsylv, V. Low-Temperature Solution Synthesis of the Non-Equilibrium Ordered Intermetallic Compounds Au<sub>3</sub>Fe, Au<sub>3</sub>Co, and Au<sub>3</sub>Ni as Nanocrystals. **2008**, 11866–11867.
- (76) Yin, A. X.; Min, X. Q.; Zhang, Y. W.; Yan, C. H. Shape-Selective Synthesis and Facet-Dependent Enhanced Electrocatalytic Activity and Durability of Monodisperse Sub-10 Nm Pt-Pd Tetrahedrons and Cubes. *J. Am. Chem. Soc.* **2011**, *133*, 3816–3819.
- (77) Berhault, G.; Bausach, M.; Bisson, L.; Becerra, L.; Thomazeau, C.; Uzio, D. Seed-Mediated Synthesis of Pd Nanocrystals: Factors Influencing a Kinetic- Or Thermodynamic-Controlled Growth Regime. *J. Phys. Chem. C* **2007**, *111*, 5915–5925.
- (78) Lohse, S. E.; Burrows, N. D.; Scarabelli, L.; Liz-Marzán, L. M.; Murphy, C. J. Anisotropic Noble Metal Nanocrystal Growth: The Role of Halides. *Chem. Mater.* **2014**, *26*, 34–43.
- (79) Sun, X.; Qin, D. Co-Titration of AgNO<sub>3</sub> and HAuCl<sub>4</sub>: A New Route to the Synthesis of Ag@Ag-Au Core-Frame Nanocubes with Enhanced Plasmonic and Catalytic Properties.

- J. Mater. Chem. C* **2015**, *3*, 11833–11841.
- (80) Rowland, C. E.; Fedin, I.; Zhang, H.; Gray, S. K.; Govorov, A. O.; Talapin, D. V.; Schaller, R. D. Picosecond Energy Transfer and Multiexciton Transfer Outpaces Auger Recombination in Binary CdSe Nanoplatelet Solids. *Nat. Mater.* **2015**, *14*, 484–489.
- (81) Protesescu, L.; Yakunin, S.; Bodnarchuk, M. I.; Krieg, F.; Caputo, R.; Hendon, C. H.; Yang, R. X.; Walsh, A.; Kovalenko, M. V. Nanocrystals of Cesium Lead Halide Perovskites (CsPbX<sub>3</sub>, X = Cl, Br, and I): Novel Optoelectronic Materials Showing Bright Emission with Wide Color Gamut. *Nano Lett.* **2015**, *15*, 3692–3696.
- (82) Mantella, V.; Ninova, S.; Saris, S.; Loiudice, A.; Aschauer, U.; Buonsanti, R. Synthesis and Size-Dependent Optical Properties of Intermediate Band Gap Cu<sub>3</sub>VS<sub>4</sub> Nanocrystals. *Chem. Mater.* **2019**, *31*, 532–540.
- (83) Puntès, V. F.; Krishnan, K. M.; Alivisatos, A. P. Colloidal Nanocrystal Shape and Size Control: The Case of Cobalt. *Science* **2001**, *291*, 2115–2117.
- (84) Lee, S. S.; Song, W.; Cho, M.; Puppala, H. L.; Nguyen, P.; Zhu, H.; Segatori, L.; Colvin, V. L. Antioxidant Properties of Cerium Oxide Nanocrystals as a Function of Nanocrystal Diameter and Surface Coating. *ACS Nano* **2013**, *7*, 9693–9703.
- (85) Singh, G.; Chan, H.; Baskin, A.; Gelman, E.; Repnin, N.; Král, P.; Klajn, R. Self-Assembly of Magnetite Nanocubes into Helical Superstructures. *Science* **2014**, *345*, 1149–1153.
- (86) Salavati-Niasari, M. Synthesis of Monodisperse Nanocrystals of Manganese Oxides. *Int. J. Nanoparticles* **2009**, *2*, 270–275.
- (87) Kim, D.; Lee, N.; Park, M.; Kim, B. H.; An, K.; Hyeon, T. Synthesis of Uniform Ferrimagnetic Magnetite Nanocubes. *J. Am. Chem. Soc.* **2009**, *131*, 454–455.
- (88) Park, J.; An, K.; Hwang, Y.; Park, J. E. G.; Noh, H. J.; Kim, J. Y.; Park, J. H.; Hwang, N. M.; Hyeon, T. Ultra-Large-Scale Syntheses of Monodisperse Nanocrystals. *Nat. Mater.* **2004**, *3*, 891–895.
- (89) Sun, S.; Zeng, H.; Robinson, D. B.; Raoux, S.; Rice, P. M.; Wang, S. X.; Li, G. Monodisperse MFe<sub>2</sub>O<sub>4</sub> (M= Fe, Co, Mn) Nanoparticles. *J. Am. Chem. Soc.* **2004**, *126*, 273–279.
- (90) Timonen, J. V. I.; Seppälä, E. T.; Ikkala, O.; Ras, R. H. A. From Hot-Injection Synthesis to Heating-up Synthesis of Cobalt Nanoparticles: Observation of Kinetically Controllable Nucleation. *Angew. Chemie - Int. Ed.* **2011**, *50*, 2080–2084.
- (91) Kwon, S. G.; Hyeon, T. Formation Mechanisms of Uniform Nanocrystals via Hot-Injection and Heat-up Methods. *Small* **2011**, *7*, 2685–2702.

- (92) Van Embden, J.; Chesman, A. S. R.; Jasieniak, J. J. The Heat-up Synthesis of Colloidal Nanocrystals. *Chem. Mater.* **2015**, *27*, 2246–2285.
- (93) Bronstein, L. M.; Atkinson, J. E.; Malyutin, A. G.; Kidwai, F.; Stein, B. D.; Morgan, D. G.; Perry, J. M.; Karty, J. A. Nanoparticles by Decomposition of Long Chain Iron Carboxylates: From Spheres to Stars and Cubes. *Langmuir* **2011**, *27*, 3044–3050.
- (94) Bronstein, L. M.; Huang, X.; Retrum, J.; Schmucker, A.; Pink, M.; Stein, B. D.; Dragnea, B. Influence of Iron Oleate Complex Structure on Iron Oxide Nanoparticle Formation. *Chem. Mater.* **2007**, *19*, 3624–3632.
- (95) Hines, M. A.; Guyot-Sionnest, P. Bright UV-Blue Luminescent Colloidal ZnSe Nanocrystals. *J. Phys. Chem. B* **1998**, *102*, 3655–3657.
- (96) Peng, Z. A.; Peng, X. Formation of High-Quality CdTe, CdSe, and CdS Nanocrystals Using CdO as Precursor. *J. Am. Chem. Soc.* **2001**, *123*, 183–184.
- (97) Peng, Z. A.; Peng, X. Nearly Monodisperse and Shape-Controlled CdSe Nanocrystals via Alternative Routes: Nucleation and Growth. *J. Am. Chem. Soc.* **2002**, *124*, 3343–3353.
- (98) Talapin, D. V.; Rogach, A. L.; Kornowski, A.; Haase, M.; Weller, H. Highly Luminescent Monodisperse CdSe and CdSe/ZnS Nanocrystals Synthesized in a Hexadecylamine-Trioctylphosphine Oxide-Trioctylphosphine Mixture. *Nano Lett.* **2001**, *1*, 207–211.
- (99) Murray, C. B.; Norris, D. J.; Bawendi, M. G. Synthesis and Characterization of Nearly Monodisperse CdE (E = S, Se, Te) Semiconductor Nanocrystallites. *J. Am. Chem. Soc.* **1993**, *115*, 8706–8715.
- (100) Yu, W. W.; Peng, X. Formation of High-Quality CdS and Other II ±VI Semiconductor Nanocrystals in Noncoordinating Solvents: Tunable Reactivity of Monomers. *Angew. Chemie - Int. Ed.* **2002**, *114*, 2368–2371.
- (101) Bönnemann, H.; Brand, R. A.; Brijoux, W.; Hofstadt, H. W.; Frerichs, M.; Kempter, V.; Maus-Friedrichs, W.; Matoussevitch, N.; Nagabhushana, K. S.; Voigts, F.; et al. Air Stable Fe and Fe-Co Magnetic Fluids - Synthesis and Characterization. *Appl. Organomet. Chem.* **2005**, *19*, 790–796.
- (102) Strach, M.; Mantella, V.; Pankhurst, J. R.; Iyengar, P.; Loiudice, A.; Das, S.; Corminboeuf, C.; Van Beek, W.; Buonsanti, R. Insights into Reaction Intermediates to Predict Synthetic Pathways for Shape-Controlled Metal Nanocrystals. *J. Am. Chem. Soc.* **2019**, *141*, 16312–16322.
- (103) Son, S. U.; Jang, Y.; Park, J.; Na, H. Bin; Park, H. M.; Yun, H. J.; Lee, J.; Hyeon, T.

- Designed Synthesis of Atom-Economical Pd/Ni Bimetallic Nanoparticle-Based Catalysts for Sonogashira Coupling Reactions. *J. Am. Chem. Soc.* **2004**, *126*, 5026–5027.
- (104) Lee, J.; Yang, J.; Kwon, S. G.; Hyeon, T. Nonclassical Nucleation and Growth of Inorganic Nanoparticles. *Nat. Rev. Mater.* **2016**, *1*, 16034.
- (105) Robinson, I.; Zacchini, S.; Tung, L. D.; Maenosono, S.; Thanh, N. T. K. Synthesis and Characterization of Magnetic Nanoalloys from Bimetallic Carbonyl Clusters. *Chem. Mater.* **2009**, *21*, 3021–3026.
- (106) Rutledge, R. D.; Morris, W. H.; Wellons, M. S.; Gai, Z.; Shen, J.; Bentley, J.; Wittig, J. E.; Lukehart, C. M. Formation of FePt Nanoparticles Having High Coercivity. *J. Am. Chem. Soc.* **2006**, *128*, 14210–14211.
- (107) Chen, M.; Kim, J.; Liu, J. P.; Fan, H.; Sun, S. Synthesis of FePt Nanocubes and Their Oriented Self-Assembly. *J. Am. Chem. Soc.* **2006**, *128*, 7132–7133.
- (108) Sun, S.; Murray, C. B.; Weller, D.; Folks, L.; Moser, A. Monodisperse FePt Nanoparticles and Ferromagnetic FePt Nanocrystal Superlattices. *Science* **2000**, *287*, 1989–1992.
- (109) Shevchenko, E. V; Talapin, D. V; Rogach, A. L.; Kornowski, A.; Haase, M.; Weller, H. Colloidal Synthesis and Self-Assembly of CoPt<sub>3</sub> Nanocrystals. *J. Am. Chem. Soc.* **2002**, *124*, 11480–11485.
- (110) Xia, Y.; Gilroy, K. D.; Peng, H. C.; Xia, X. Seed-Mediated Growth of Colloidal Metal Nanocrystals. *Angew. Chemie - Int. Ed.* **2017**, *56*, 60–95.
- (111) Gao, C.; Goebel, J.; Yin, Y. Seeded Growth Route to Noble Metal Nanostructures. *J. Mater. Chem. C* **2013**, *1*, 3898–3909.
- (112) Niu, W.; Zhang, L.; Xu, G. Seed-Mediated Growth of Noble Metal Nanocrystals: Crystal Growth and Shape Control. *Nanoscale* **2013**, *5*, 3172–3181.
- (113) Scarfiello, R.; Nobile, C.; Cozzoli, P. D. Colloidal Magnetic Heterostructured Nanocrystals with Asymmetric Topologies: Seeded-Growth Synthetic Routes and Formation Mechanisms. *Front. Mater.* **2016**, *3*, 1–29.
- (114) Fan, F. R.; Liu, D. Y.; Wu, Y. F.; Duan, S.; Xie, Z. X.; Jiang, Z. Y.; Tian, Z. Q. Epitaxial Growth of Heterogeneous Metal Nanocrystals: From Gold Nano-Octahedra to Palladium and Silver Nanocubes. *J. Am. Chem. Soc.* **2008**, *130*, 6949–6951.
- (115) Enright, M. J.; Dou, F. Y.; Wu, S.; Rabe, E. J.; Monahan, M.; Friedfeld, M. R.; Schlenker, C. W.; Cossairt, B. M. Seeded Growth of Nanoscale Semiconductor Tetrapods: Generality and the Role of Cation Exchange. *Chem. Mater.* **2020**, *32*, 4774–4784.
- (116) Cozzoli, P. D.; Pellegrino, T.; Manna, L. Synthesis, Properties and Perspectives of

- Hybrid Nanocrystal Structures. *Chem. Soc. Rev.* **2006**, *35*, 1195–1208.
- (117) Carbone, L.; Cozzoli, P. D. Colloidal Heterostructured Nanocrystals: Synthesis and Growth Mechanisms. *Nano Today* **2010**, *5*, 449–493.
- (118) Xia, Y.; Xia, X.; Peng, H. C. Shape-Controlled Synthesis of Colloidal Metal Nanocrystals: Thermodynamic versus Kinetic Products. *J. Am. Chem. Soc.* **2015**, *137*, 7947–7966.
- (119) Xia, X.; Xie, S.; Liu, M.; Peng, H. C.; Lu, N.; Wang, J.; Kim, M. J.; Xia, Y. On the Role of Surface Diffusion in Determining the Shape or Morphology of Noble-Metal Nanocrystals. *Proc. Natl. Acad. Sci. U. S. A.* **2013**, *110*, 6669–6673.
- (120) Xie, S.; Lu, N.; Xie, Z.; Wang, J.; Kim, M. J.; Xia, Y. Synthesis of Pd-Rh Core-Frame Concave Nanocubes and Their Conversion to Rh Cubic Nanoframes by Selective Etching of the Pd Cores. *Angew. Chemie - Int. Ed.* **2012**, *51*, 10266–10270.
- (121) Habas, S. E.; Lee, H.; Radmilovic, V.; Somorjai, G. A.; Yang, P. Shaping Binary Metal Nanocrystals through Epitaxial Seeded Growth. *Nat. Mater.* **2007**, *6*, 692–697.
- (122) Shore, M. S.; Wang, J.; Johnston-Peck, A. C.; Oldenburg, A. L.; Tracy, J. B. Synthesis of Au(Core)/Ag(Shell) Nanoparticles and Their Conversion to AuAg Alloy Nanoparticles. *Small* **2011**, *7*, 230–234.
- (123) Lim, B.; Jiang, M.; Camargo, P. H. C.; Cho, E. C.; Tao, J.; Lu, X.; Zhu, Y.; Xia, Y. Pd-Pt Bimetallic Nanodendrites with High Activity for Oxygen Reduction. *Science* **2009**, *324*, 1302–1305.
- (124) Langille, M. R.; Zhang, J.; Personick, M. L.; Li, S.; Mirkin, C. A. Stepwise Evolution of Spherical Seeds into 20-Fold Twinned Icosahedra. *Science* **2012**, *337*, 954–958.
- (125) Xia, X.; Wang, Y.; Ruditskiy, A.; Xia, Y. 25th Anniversary Article: Galvanic Replacement: A Simple and Versatile Route to Hollow Nanostructures with Tunable and Well-Controlled Properties. *Adv. Mater.* **2013**, *25*, 6313–6332.
- (126) Wang, X.; Chen, S.; Reggiano, G.; Thota, S.; Wang, Y.; Kerns, P.; Suib, S. L.; Zhao, J. Au-Cu-M (M = Pt, Pd, Ag) Nanorods with Enhanced Catalytic Efficiency by Galvanic Replacement Reaction. *Chem. Commun.* **2019**, *55*, 1249–1252.
- (127) Da Silva, A. G. M.; Rodrigues, T. S.; Haigh, S. J.; Camargo, P. H. C. Galvanic Replacement Reaction: Recent Developments for Engineering Metal Nanostructures towards Catalytic Applications. *Chem. Commun.* **2017**, *53*, 7135–7148.
- (128) Kim, M. H.; Lu, X.; Wiley, B.; Lee, E. P.; Xia, Y. Morphological Evolution of Single-Crystal Ag Nanospheres during the Galvanic Replacement Reaction with HAuCl<sub>4</sub>. *J. Phys. Chem. C* **2008**, *112*, 7872–7876.

- (129) Sutter, E. A.; Sutter, P. W. In Situ Liquid Cell Electron Microscopy of Ag-Au Galvanic Replacement Reactions. *Nanoscale* **2017**, *9*, 1271–1278.
- (130) Yavuz, M. S.; Cheng, Y.; Chen, J.; Cobley, C. M.; Zhang, Q.; Rycenga, M.; Xie, J.; Kim, C.; Song, K. H.; Schwartz, A. G.; et al. Gold Nanocages Covered by Smart Polymers for Controlled Release with Near-Infrared Light. *Nat. Mater.* **2009**, *8*, 935–939.
- (131) Anderson, B. D.; Tracy, J. B. Nanoparticle Conversion Chemistry: Kirkendall Effect, Galvanic Exchange, and Anion Exchange. *Nanoscale* **2014**, *6*, 12195–12216.
- (132) Sun, Y.; T. Mayers, B.; Xia, Y. Template-Engaged Replacement Reaction: A One-Step Approach to the Large-Scale Synthesis of Metal Nanostructures with Hollow Interiors. *Nano Lett.* **2002**, *2*, 481–485.
- (133) Zhang, H.; Jin, M.; Xia, Y. Enhancing the Catalytic and Electrocatalytic Properties of Pt-Based Catalysts by Forming Bimetallic Nanocrystals with Pd. *Chem. Soc. Rev.* **2012**, *41*, 8035–8049.
- (134) Chen, A. N.; McClain, S. M.; House, S. D.; Yang, J. C.; Skrabalak, S. E. Mechanistic Study of Galvanic Replacement of Chemically Heterogeneous Templates. *Chem. Mater.* **2019**, *31*, 1344–1351.
- (135) Lu, X.; Tuan, H. Y.; Chen, J.; Li, Z. Y.; Korgel, B. A.; Xia, Y. Mechanistic Studies on the Galvanic Replacement Reaction between Multiply Twinned Particles of Ag and HAuCl<sub>4</sub> in an Organic Medium. *J. Am. Chem. Soc.* **2007**, *129*, 1733–1742.
- (136) Sun, Y.; Xia, Y. Mechanistic Study on the Replacement Reaction between Silver Nanostructures and Chloroauric Acid in Aqueous Medium. *J. Am. Chem. Soc.* **2004**, *126*, 3892–3901.
- (137) Hong, X.; Wang, D.; Cai, S.; Rong, H.; Li, Y. Single-Crystalline Octahedral Au – Ag Nanoframes. *J. Am. Chem. Soc.* **2012**, *134*, 18165–18168.
- (138) Gilroy, K. D.; Farzinpour, P.; Sundar, A.; Hughes, R. A.; Neretina, S. Sacrificial Templates for Galvanic Replacement Reactions: Design Criteria for the Synthesis of Pure Pt Nanoshells with a Smooth Surface Morphology. *Chem. Mater.* **2014**, *26*, 3340–3347.
- (139) Oh, M. H.; Yu, T.; Yu, S.-H.; Lim, B.; Ko, K.-T.; Willinger, M.-G.; Seo, D.-H.; Kim, B. H.; Cho, M. G.; Park, J.-H.; et al. Galvanic Replacement Reactions in Metal Oxide Nanocrystals. *Science* **2013**, *340*, 964–969.
- (140) Chen, J.; Wiley, B.; McLellan, J.; Xiong, Y.; Li, Z. Y.; Xia, Y. Optical Properties of Pd-Ag and Pt-Ag Nanoboxes Synthesized via Galvanic Replacement Reactions. *Nano Lett.* **2005**, *5*, 2058–2062.

- (141) Pasricha, R.; Bala, T.; Biradar, A. V.; Umbarkar, S.; Sastry, M. Synthesis of Catalytically Active Porous Platinum Nanoparticles by Transmetallation Reaction and Proposition of the Mechanism. *Small* **2009**, *5*, 1467–1473.
- (142) Vasquez, Y.; Sra, A. K.; Schaak, R. E. One-Pot Synthesis of Hollow Superparamagnetic CoPt Nanospheres. *J. Am. Chem. Soc.* **2005**, *127*, 12504–12505.
- (143) Sun, Q.; Wang, S.; Wang, R. Well-Aligned CoPt Hollow Nanochains Synthesized in Water at Room Temperature. *J. Phys. Chem. C* **2012**, *116*, 5352–5357.
- (144) Mohl, M.; Dobo, D.; Kukovecz, A.; Konya, Z.; Kordas, K.; Wei, J.; Vajtai, R.; Ajayan, P. M. Formation of CuPd and CuPt Bimetallic Nanotubes by Galvanic Replacement Reaction. *J. Phys. Chem. C* **2011**, *115*, 9403–9409.
- (145) Liang, H. P.; Zhang, H. M.; Hu, J. S.; Guo, Y. G.; Wan, L. J.; Bai, C. L. Pt Hollow Nanospheres: Facile Synthesis and Enhanced Electrocatalysts. *Angew. Chemie - Int. Ed.* **2004**, *43*, 1540–1543.
- (146) Zhou, C.; Jiang, X.; Yang, L.; Yin, Y.; Jin, M. Low-Temperature Carbon Monoxide Oxidation with Au-Cu Meatball-like Cages Prepared by Galvanic Replacement. *ChemSusChem* **2013**, *6*, 1883–1887.
- (147) Mayers, B.; Jiang, X.; Sunderland, D.; Cattle, B.; Xia, Y. Hollow Nanostructures of Platinum with Controllable Dimensions Can Be Synthesized by Templating against Selenium Nanowires and Colloids. *J. Am. Chem. Soc.* **2003**, *125*, 13364–13365.
- (148) Lin, Z. H.; Chang, H. T. Preparation of Gold-Tellurium Hybrid Nanomaterials for Surface-Enhanced Raman Spectroscopy. *Langmuir* **2008**, *24*, 365–367.
- (149) Gao, C.; Lu, Z.; Liu, Y.; Zhang, Q.; Chi, M.; Cheng, Q.; Yin, Y. Highly Stable Silver Nanoplates for Surface Plasmon Resonance Biosensing. *Angew. Chemie - Int. Ed.* **2012**, *51*, 5629–5633.
- (150) Yang, Y.; Liu, J.; Fu, Z. W.; Qin, D. Galvanic Replacement-Free Deposition of Au on Ag for Core-Shell Nanocubes with Enhanced Chemical Stability and SERS Activity. *J. Am. Chem. Soc.* **2014**, *136*, 8153–8156.
- (151) Polavarapu, L.; Zanaga, D.; Altantzis, T.; Rodal-Cedeira, S.; Pastoriza-Santos, I.; Pérez-Juste, J.; Bals, S.; Liz-Marzán, L. M. Galvanic Replacement Coupled to Seeded Growth as a Route for Shape-Controlled Synthesis of Plasmonic Nanorattles. *J. Am. Chem. Soc.* **2016**, *138*, 11453–11456.
- (152) Yang, Y.; Zhang, Q.; Fu, Z. W.; Qin, D. Transformation of Ag Nanocubes into Ag-Au Hollow Nanostructures with Enriched Ag Contents to Improve SERS Activity and Chemical Stability. *ACS Appl. Mater. Interfaces* **2014**, *6*, 3750–3757.

- (153) Jing, H.; Wang, H. Structural Evolution of Ag-Pd Bimetallic Nanoparticles through Controlled Galvanic Replacement: Effects of Mild Reducing Agents. *Chem. Mater.* **2015**, *27*, 2172–2180.
- (154) Da Silva, A. G. M.; Rodrigues, T. S.; Slater, T. J. A.; Lewis, E. A.; Alves, R. S.; Fajardo, H. V.; Balzer, R.; Da Silva, A. H. M.; De Freitas, I. C.; Oliveira, D. C.; et al. Controlling Size, Morphology, and Surface Composition of AgAu Nanodendrites in 15 s for Improved Environmental Catalysis under Low Metal Loadings. *ACS Appl. Mater. Interfaces* **2015**, *7*, 25624–25632.
- (155) Rodrigues, T. S.; da Silva, A. G. M.; Gonçalves, M. C.; Fajardo, H. V.; Balzer, R.; Probst, L. F. D.; Camargo, P. H. C. AgPt Hollow Nanodendrites: Synthesis and Uniform Dispersion over SiO<sub>2</sub> Support for Catalytic Applications. *ChemNanoMat* **2015**, *1*, 46–51.
- (156) da Silva, A. G. M.; Rodrigues, T. S.; Taguchi, L. S. K.; Fajardo, H. V.; Balzer, R.; Probst, L. F. D.; Camargo, P. H. C. Pd-Based Nanoflowers Catalysts: Controlling Size, Composition, and Structures for the 4-Nitrophenol Reduction and BTX Oxidation Reactions. *J. Mater. Sci.* **2015**, *51*, 603–614.
- (157) Da Silva, A. G. M.; De Souza, M. L.; Rodrigues, T. S.; Alves, R. S.; Temperini, M. L. A.; Camargo, P. H. C. Rapid Synthesis of Hollow Ag-Au Nanodendrites in 15 Seconds by Combining Galvanic Replacement and Precursor Reduction Reactions. *Chem. - A Eur. J.* **2014**, *20*, 15040–15046.
- (158) Hong, J. W.; Kang, S. W.; Choi, B. S.; Kim, D.; Lee, S. B.; Han, S. W. Controlled Synthesis of Pd-Pt Alloy Hollow Nanostructures with Enhanced Catalytic Activities for Oxygen Reduction. *ACS Nano* **2012**, *6*, 2410–2419.
- (159) Kang, Y.; Murray, C. B. Synthesis and Electrocatalytic Properties of Cubic Mn-Pt Nanocrystals (Nanocubes). *J. Am. Chem. Soc.* **2010**, *132*, 7568–7569.
- (160) Greeley, J.; Stephens, I. E. L.; Bondarenko, A. S.; Johansson, T. P.; Hansen, H. A.; Jaramillo, T. F.; Rossmeisl, J.; Chorkendorff, I.; Nørskov, J. K. Alloys of Platinum and Early Transition Metals as Oxygen Reduction Electrocatalysts. *Nat. Chem.* **2009**, *1*, 552–556.
- (161) Yen, C. W.; Mahmoud, M. A.; El-Sayed, M. A. Photocatalysis in Gold Nanocage Nanoreactors. *J. Phys. Chem. A* **2009**, *113*, 4340–4345.
- (162) Zhang, W.; Yang, J.; Lu, X. Tailoring Galvanic Replacement Reaction for the Preparation of Pt/Ag Bimetallic Hollow Nanostructures with Controlled Number of Voids. *ACS Nano* **2012**, *6*, 7397–7405.



- (163) Stamenkovic, V. R.; Mun, B. S.; Arenz, M.; Mayrhofer, K. J. J.; Lucas, C. A.; Wang, G.; Ross, P. N.; Markovic, N. M. Trends in Electrocatalysis on Extended and Nanoscale Pt-Bimetallic Alloy Surfaces. *Nat. Mater.* **2007**, *6*, 241–247.
- (164) Oloye, O.; Tang, C.; Du, A.; Will, G.; O'Mullane, A. P. Galvanic Replacement of Liquid Metal Galinstan with Pt for the Synthesis of Electrocatalytically Active Nanomaterials. *Nanoscale* **2019**, *11*, 9705–9715.
- (165) Gao, J.; Zhang, H.; Guo, X.; Luo, J.; Zakeeruddin, S. M.; Ren, D.; Grätzel, M. Selective C-C Coupling in Carbon Dioxide Electroreduction via Efficient Spillover of Intermediates As Supported by Operando Raman Spectroscopy. *J. Am. Chem. Soc.* **2019**, *141*, 18704–18714.
- (166) Zhu, Y.; Zhang, X.; Koh, K.; Kovarik, L.; Fulton, J. L.; Rosso, K. M.; Gutiérrez, O. Y. Inverse Iron Oxide/Metal Catalysts from Galvanic Replacement. *Nat. Commun.* **2020**, *11*, 1–7.
- (167) Wang, Y.; Arandiyan, H.; Bartlett, S. A.; Trunschke, A.; Sun, H.; Scott, J.; Lee, A. F.; Wilson, K.; Maschmeyer, T.; Schlögl, R.; et al. Inducing Synergy in Bimetallic RhNi Catalysts for CO<sub>2</sub> Methanation by Galvanic Replacement. *Appl. Catal. B Environ.* **2020**, *277*, 119029.
- (168) Zhang, X.; Liu, C.; Zhao, Y.; Li, L.; Chen, Y.; Raziq, F.; Qiao, L.; Guo, S. X.; Wang, C.; Wallace, G. G.; et al. Atomic Nickel Cluster Decorated Defect-Rich Copper for Enhanced C<sub>2</sub> Product Selectivity in Electrocatalytic CO<sub>2</sub> Reduction. *Appl. Catal. B Environ.* **2021**, *291*, 120030.
- (169) Mosali, V. S. S.; Zhang, X.; Zhang, Y.; Gengenbach, T.; Guo, S. X.; Puxty, G.; Horne, M. D.; Bond, A. M.; Zhang, J. Electrocatalytic CO<sub>2</sub> Reduction to Formate on Cu Based Surface Alloys with Enhanced Selectivity. *ACS Sustain. Chem. Eng.* **2019**, *7*, 19453–19462.
- (170) Zhou, J. H.; Lan, D. W.; Yang, S. S.; Guo, Y.; Yuan, K.; Dai, L. X.; Zhang, Y. W. Thin-Walled Hollow Au-Cu Nanostructures with High Efficiency in Electrochemical Reduction of CO<sub>2</sub> to CO. *Inorg. Chem. Front.* **2018**, *5*, 1524–1532.
- (171) Zhang, L.; Zhang, Y.; Wang, H.; Chen, J.; Cao, Z. Preparation of Hollow Au<sub>x</sub>-Cu<sub>2</sub>O Nanospheres by Galvanic Replacement to Enhance the Selective Electrocatalytic CO<sub>2</sub> Reduction to Ethanol. *J. Exp. Nanosci.* **2022**, *17*, 173–186.
- (172) Choi, C.; Cai, J.; Lee, C.; Lee, H. M.; Xu, M.; Huang, Y. Intimate Atomic Cu-Ag Interfaces for High CO<sub>2</sub>RR Selectivity towards CH<sub>4</sub> at Low over Potential. *Nano Res.* **2021**, *14*, 3497–3501.

- (173) Zoski, C. G. *Handbook of Electrochemistry*, Elsevier.; Amsterdam, 2007.
- (174) Hoshyargar, F.; Crawford, J.; O'Mullane, A. P. Galvanic Replacement of the Liquid Metal Galinstan. *J. Am. Chem. Soc.* **2017**, *139*, 1464–1471.
- (175) Kepp, K. P. A Quantitative Scale of Oxophilicity and Thiophilicity. *Inorg. Chem.* **2016**, *55*, 9461–9470.
- (176) Kalantar-Zadeh, K.; Tang, J.; Daeneke, T.; O'Mullane, A. P.; Stewart, L. A.; Liu, J.; Majidi, C.; Ruoff, R. S.; Weiss, P. S.; Dickey, M. D. Emergence of Liquid Metals in Nanotechnology. *ACS Nano* **2019**, *13*, 7388–7395.
- (177) Daeneke, T.; Khoshmanesh, K.; Mahmood, N.; De Castro, I. A.; Esrafilzadeh, D.; Barrow, S. J.; Dickey, M. D.; Kalantar-Zadeh, K. Liquid Metals: Fundamentals and Applications in Chemistry. *Chem. Soc. Rev.* **2018**, *47*, 4073–4111.
- (178) Zhang, W.; Ou, J. Z.; Tang, S. Y.; Sivan, V.; Yao, D. D.; Latham, K.; Khoshmanesh, K.; Mitchell, A.; O'Mullane, A. P.; Kalantar-Zadeh, K. Liquid Metal/Metal Oxide Frameworks. *Adv. Funct. Mater.* **2014**, *24*, 3799–3807.
- (179) Song, H.; Kim, T.; Kang, S.; Jin, H.; Lee, K.; Yoon, H. J. Ga-Based Liquid Metal Micro/Nanoparticles: Recent Advances and Applications. *Small* **2019**, *16*, 1903391.
- (180) Wan, A.; Suchand Sangeeth, C. S.; Wang, L.; Yuan, L.; Jiang, L.; Nijhuis, C. A. Arrays of High Quality SAM-Based Junctions and Their Application in Molecular Diode Based Logic. *Nanoscale* **2015**, *7*, 19547–19556.
- (181) Tang, S. Y.; Tabor, C.; Kalantar-Zadeh, K.; Dickey, M. D. Gallium Liquid Metal: The Devil's Elixir. *Annu. Rev. Mater. Res.* **2021**, *51*, 381–408.
- (182) Lu, Y.; Hu, Q.; Lin, Y.; Pacardo, D. B.; Wang, C.; Sun, W.; Ligler, F. S.; Dickey, M. D.; Gu, Z. Transformable Liquid-Metal Nanomedicine. *Nat. Commun.* **2015**, *6*, 1–10.
- (183) Chechetka, S. A.; Yu, Y.; Zhen, X.; Pramanik, M.; Pu, K.; Miyako, E. Light-Driven Liquid Metal Nanotransformers for Biomedical Theranostics. *Nat. Commun.* **2017**, *8*, 1–19.
- (184) Sun, X.; Sun, M.; Liu, M.; Yuan, B.; Gao, W.; Rao, W.; Liu, J. Shape Tunable Gallium Nanorods Mediated Tumor Enhanced Ablation through Near-Infrared Photothermal Therapy. *Nanoscale* **2019**, *11*, 2655–2667.
- (185) Esrafilzadeh, D.; Zavabeti, A.; Jalili, R.; Atkin, P.; Choi, J.; Carey, B. J.; Brkljača, R.; O'Mullane, A. P.; Dickey, M. D.; Officer, D. L.; et al. Room Temperature CO<sub>2</sub> Reduction to Solid Carbon Species on Liquid Metals Featuring Atomically Thin Ceria Interfaces. *Nat. Commun.* **2019**, *10*, 865.
- (186) Taccardi, N.; Grabau, M.; Debuschewitz, J.; Distaso, M.; Brandl, M.; Hock, R.; Maier,

- F.; Papp, C.; Erhard, J.; Neiss, C.; et al. Gallium-Rich Pd-Ga Phases as Supported Liquid Metal Catalysts. *Nat. Chem.* **2017**, *9*, 862–867.
- (187) Zuraiqi, K.; Zavabeti, A.; Allieux, F. M.; Tang, J.; Nguyen, C. K.; Tafazolymotie, P.; Mayyas, M.; Ramarao, A. V.; Spencer, M.; Shah, K.; et al. Liquid Metals in Catalysis for Energy Applications. *Joule* **2020**, *4*, 2290–2321.
- (188) Yarema, M.; Wörle, M.; D. Rossell, M.; Erni, R.; Caputo, R.; Protesescu, L.; V. Kravchyk, K.; N. Dirin, D.; Lienau, K.; von Rohr, F.; et al. Monodisperse Colloidal Gallium Nanoparticles: Synthesis, Low Temperature Crystallization, Surface Plasmon Resonance and Li-Ion Storage. *J. Am. Chem. Soc.* **2014**, *136*, 12422–12430.
- (189) Lin, Y.; Genzer, J.; Dickey, M. D. Attributes, Fabrication, and Applications of Gallium-Based Liquid Metal Particles. *Adv. Sci.* **2020**, *7*, 2000192.
- (190) Okatenko, V.; Castilla-Amorós, L.; Stoian, D. C.; Vavra, J.; Loiudice, A. The Native Oxide Skin of Liquid Metal Ga Nanoparticles Prevents Their Rapid Coalescence during Electrocatalysis. *J. Am. Chem. Soc.* **2022**, *144*, 10053–10063.
- (191) Liu, H.; Xia, J.; Zhang, N.; Cheng, H.; Bi, W.; Zu, X.; Chu, W.; Wu, H.; Wu, C.; Xie, Y. Solid–Liquid Phase Transition Induced Electrocatalytic Switching from Hydrogen Evolution to Highly Selective CO<sub>2</sub> Reduction. *Nat. Catal.* **2021**, *4*, 202–211.
- (192) Kim, D.; Thissen, P.; Viner, G.; Lee, D. W.; Choi, W.; Chabal, Y. J.; Lee, J. B. Recovery of Nonwetting Characteristics by Surface Modification of Gallium-Based Liquid Metal Droplets Using Hydrochloric Acid Vapor. *ACS Appl. Mater. Interfaces* **2013**, *5*, 179–185.
- (193) Khan, M. R.; Eaker, C. B.; Bowden, E. F.; Dickey, M. D. Giant and Switchable Surface Activity of Liquid Metal via Surface Oxidation. *Proc. Natl. Acad. Sci. U. S. A.* **2014**, *111*, 14047–14051.
- (194) Ermoline, A.; Dreizin, E. L. Equations for the Cabrera-Mott Kinetics of Oxidation for Spherical Nanoparticles. *Chem. Phys. Lett.* **2011**, *505*, 47–50.
- (195) Sutter, E.; Sutter, P. Size-Dependent Room Temperature Oxidation of in Nanoparticles. *J. Phys. Chem. C* **2012**, *116*, 20574–20578.
- (196) Wang, T.; Farvid, S. S.; Abulikemu, M.; Radovanovic, P. V. Size-Tunable Phosphorescence in Colloidal Metastable  $\gamma$ -Ga<sub>2</sub>O<sub>3</sub> Nanocrystals. *J. Am. Chem. Soc.* **2010**, *132*, 9250–9252.
- (197) Housecroft, C. E.; Sharpe, A. G. *Inorganic Chemistry*, 4th editio.; Pearson Education Limited, 2012.
- (198) Boyanov, B. Farrel Lytle Database

- [http://ixs.iit.edu/database/data/Farrel\\_Lytle\\_data/index.html](http://ixs.iit.edu/database/data/Farrel_Lytle_data/index.html).
- (199) Clark, A. H.; Imbao, J.; Frahm, R.; Nachtegaal, M. ProQEXAFS: A Highly Optimized Parallelized Rapid Processing Software for QEXAFS Data. *J. Synchrotron Radiat.* **2020**, *27*, 551–557.
- (200) Knight, M. W.; Coenen, T.; Yang, Y.; Brenny, B. J. M.; Losurdo, M.; Brown, A. S.; Everitt, H. O.; Polman, A. Gallium Plasmonics: Deep Subwavelength Spectroscopic Imaging of Single and Interacting Gallium Nanoparticles. *ACS Nano* **2015**, *9*, 2049–2060.
- (201) Reineck, P.; Lin, Y.; Gibson, B. C.; Dickey, M. D.; Greentree, A. D.; Maksymov, I. S. UV Plasmonic Properties of Colloidal Liquid-Metal Eutectic Gallium-Indium Alloy Nanoparticles. *Sci. Rep.* **2019**, *9*, 1–7.
- (202) Armbrüster, M.; Wowsnick, G.; Friedrich, M.; Heggen, M.; Cardoso-Gil, R. Synthesis and Catalytic Properties of Nanoparticulate Intermetallic Ga-Pd Compounds. *J. Am. Chem. Soc.* **2011**, *133*, 9112–9118.
- (203) Torelli, D. A.; Francis, S. A.; Crompton, J. C.; Javier, A.; Thompson, J. R.; Brunschwig, B. S.; Soriaga, M. P.; Lewis, N. S. Nickel-Gallium-Catalyzed Electrochemical Reduction of CO<sub>2</sub> to Highly Reduced Products at Low Overpotentials. *ACS Catal.* **2016**, *6*, 2100–2104.
- (204) Li, C.; Chen, Y.; Zhang, S.; Zhou, J.; Wang, F.; He, S.; Wei, M.; Evans, D. G.; Duan, X. Nickel-Gallium Intermetallic Nanocrystal Catalysts in the Semihydrogenation of Phenylacetylene. *ChemCatChem* **2014**, *6*, 824–831.
- (205) Schütte, K.; Doddi, A.; Kroll, C.; Meyer, H.; Wiktor, C.; Gemel, C.; Van Tendeloo, G.; Fischer, R. A.; Janiak, C. Colloidal Nickel/Gallium Nanoalloys Obtained from Organometallic Precursors in Conventional Organic Solvents and in Ionic Liquids: Noble-Metal-Free Alkyne Semihydrogenation Catalysts. *Nanoscale* **2014**, *6*, 5532–5544.
- (206) Xia, Y.; Xiong, Y.; Lim, B.; Skrabalak, S. E. Shape-Controlled Synthesis of Metal Nanocrystals: Simple Chemistry Meets Complex Physics? *Angew. Chemie - Int. Ed.* **2009**, *48*, 60–103.
- (207) Zhang, H.; Jin, M.; Xiong, Y.; Lim, B.; Xia, Y. Shape-Controlled Synthesis of Pd Nanocrystals and Their Catalytic Applications. *Acc. Chem. Res.* **2013**, *46*, 1783–1794.
- (208) O'Brien, M. N.; Jones, M. R.; Brown, K. A.; Mirkin, C. A. Universal Noble Metal Nanoparticle Seeds Realized through Iterative Reductive Growth and Oxidative Dissolution Reactions. *J. Am. Chem. Soc.* **2014**, *136*, 7603–7606.

- (209) Li, C.; Sato, R.; Kanehara, M.; Zeng, H.; Bando, Y.; Teranishi, T. Controllable Polyol Synthesis of Uniform Palladium Icosahedra: Effect of Twinned Structure on Deformation of Crystalline Lattices. *Angew. Chemie - Int. Ed.* **2009**, *48*, 6883–6887.
- (210) Li, C.; Shuford, K. L.; Park, Q. H.; Cai, W.; Li, Y.; Lee, E. J.; Cho, S. O. High-Yield Synthesis of Single-Crystalline Gold Nano-Octahedra. *Angew. Chemie - Int. Ed.* **2007**, *46*, 3264–3268.
- (211) Huang, H.; Wang, Y.; Ruditskiy, A.; Peng, H. C.; Zhao, X.; Zhang, L.; Liu, J.; Ye, Z.; Xia, Y. Polyol Syntheses of Palladium Decahedra and Icosahedra as Pure Samples by Maneuvering the Reaction Kinetics with Additives. *ACS Nano* **2014**, *8*, 7041–7050.
- (212) Wiley, B.; Herricks, T.; Sun, Y.; Xia, Y. Polyol Synthesis of Silver Nanoparticles: Use of Chloride and Oxygen to Promote the Formation of Single-Crystal, Truncated Cubes and Tetrahedrons. *Nano Lett.* **2004**, *4*, 1733–1739.
- (213) Sun, Y.; Xia, Y. Shape-Controlled Synthesis of Gold and Silver Nanoparticles. *Science* **2002**, *298*, 2176–2179.
- (214) Liu, S.; Sweatman, K.; McDonald, S.; Nogita, K. Ga-Based Alloys in Microelectronic Interconnects: A Review. *Materials (Basel)*. **2018**, *11*, 1384.
- (215) Yunusa, M.; Amador, G. J.; Drotlef, D. M.; Sitti, M. Wrinkling Instability and Adhesion of a Highly Bendable Gallium Oxide Nanofilm Encapsulating a Liquid-Gallium Droplet. *Nano Lett.* **2018**, *18*, 2498–2504.
- (216) Mourdikoudis, S.; Liz-Marzán, L. M. Oleylamine in Nanoparticle Synthesis. *Chem. Mater.* **2013**, *25*, 1465–1476.
- (217) Rana, M. S.; Rahman, M. A.; Alam, A. M. S. A CV Study of Copper Complexation with Guanine Using Glassy Carbon Electrode in Aqueous Medium. *ISRN Electrochem.* **2014**, *2014*, 1–7.
- (218) Sandoval-Rojas, A. P.; Ibarra, L.; Cortés, M. T.; Macías, M. A.; Suescun, L.; Hurtado, J. Synthesis and Characterization of Copper(II) Complexes Containing Acetate and N,N-Donor Ligands, and Their Electrochemical Behavior in Dopamine Detection. *J. Electroanal. Chem.* **2017**, *805*, 60–67.
- (219) Elgrishi, N.; Rountree, K. J.; McCarthy, B. D.; Rountree, E. S.; Eisenhart, T. T.; Dempsey, J. L. A Practical Beginner's Guide to Cyclic Voltammetry. *J. Chem. Educ.* **2018**, *95*, 197–206.
- (220) Ravel, B.; Newville, M. ATHENA, ARTEMIS, HEPHAESTUS: Data Analysis for X-Ray Absorption Spectroscopy Using IFEFFIT. *J. Synchrotron Radiat.* **2005**, *12*, 537–541.

- 
- (221) Cabrera, N. .; Mott, N. F. Theory of the Oxidation of Metals. *Reports Prog. Phys.* **1949**, *12*, 163.
- (222) Tabor, C.; Holcomb, S.; Heikenfeld, J. Reliable and Reversible Contact of Eutectic Gallium Indium and Copper Electrodes. *Adv. Mater. Interfaces* **2020**, *7*, 1–8.
- (223) Moffitt, S. L.; Zhu, Q.; Ma, Q.; Falduto, A. F.; Buchholz, D. B.; Chang, R. P. H.; Mason, T. O.; Medvedeva, J. E.; Marks, T. J.; Bedzyk, M. J. Probing the Unique Role of Gallium in Amorphous Oxide Semiconductors through Structure–Property Relationships. *Adv. Electron. Mater.* **2017**, *3*, 1–12.
- (224) Chen, S.; Jenkins, S. V.; Tao, J.; Zhu, Y.; Chen, J. Anisotropic Seeded Growth of Cu-M (M = Au, Pt, or Pd) Bimetallic Nanorods with Tunable Optical and Catalytic Properties. *J. Phys. Chem. C* **2013**, *117*, 8924–8932.
- (225) Larsen, R. J.; Dickey, M. D.; Whitesides, G. M.; Weitz, D. A. Viscoelastic Properties of Oxide-Coated Liquid Metals. *J. Rheol. (N. Y. N. Y.)* **2009**, *53*, 1305–1326.
- (226) Ladd, C.; So, J. H.; Muth, J.; Dickey, M. D. 3D Printing of Free Standing Liquid Metal Microstructures. *Adv. Mater.* **2013**, *25*, 5081–5085.
- (227) Dickey, M. D. Emerging Applications of Liquid Metals Featuring Surface Oxides. *ACS Appl. Mater. Interfaces* **2014**, *6*, 18369–18379.
- (228) Khondoker, M. A. H.; Sameoto, D. Fabrication Methods and Applications of Microstructured Gallium Based Liquid Metal Alloys. *Smart Mater. Struct.* **2016**, *25*, 093001.
- (229) Xu, Q.; Oudalov, N.; Guo, Q.; Jaeger, H. M.; Brown, E. Effect of Oxidation on the Mechanical Properties of Liquid Gallium and Eutectic Gallium-Indium. *Phys. Fluids* **2012**, *24*, 063101.
- (230) Buonsanti, R.; Grillo, V.; Carlino, E.; Giannini, C.; Curri, M. L.; Innocenti, C.; Sangregorio, C.; Achterhold, K.; Parak, F. G.; Agostiano, A.; et al. Seeded Growth of Asymmetric Binary Nanocrystals Made of a Semiconductor TiO<sub>2</sub> Rodlike Section and a Magnetic  $\gamma$ -Fe<sub>2</sub>O<sub>3</sub> Spherical Domain. *J. Am. Chem. Soc.* **2006**, *128*, 16953–16970.
- (231) Kumar, S. S.; Rubio, E. J.; Noor-A-Alam, M.; Martinez, G.; Manandhar, S.; Shutthanandan, V.; Thevuthasan, S.; Ramana, C. V. Structure, Morphology, and Optical Properties of Amorphous and Nanocrystalline Gallium Oxide Thin Films. *J. Phys. Chem. C* **2013**, *117*, 4194–4200.
- (232) Chatterji, D.; West, R. W. Thermodynamic Properties of the System Indium-Oxygen. *J. Am. Ceram. Soc.* **1972**, *55*, 575–578.
- (233) Subramanlan, B. P. R.; Laughlin, D. E. The Cu-Ln ( Copper-Indium ) System. *Bull.*

- Alloy Phase Diagrams* **1989**, *10*, 554–568.
- (234) Bo, G.; Yu, H.; Ren, L.; Cheng, N.; Feng, H.; Xu, X.; Xue Dou, S.; Wang, H.; Du, Y. Gallium–Indium–Tin Liquid Metal Nanodroplet-Based Anisotropic Conductive Adhesives for Flexible Integrated Electronics. *ACS Appl. Nano Mater.* **2021**, *4*, 550–557.
- (235) Sun, X.; Yuan, B.; Sheng, L.; Rao, W.; Liu, J. Liquid Metal Enabled Injectable Biomedical Technologies and Applications. *Appl. Mater. Today* **2020**, *20*, 100722.
- (236) Martin, A.; Du, C.; Chang, B.; Thuo, M. Complexity and Opportunities in Liquid Metal Surface Oxides. *Chem. Mater.* **2020**, *32*, 9045–9055.
- (237) Doudrick, K.; Liu, S.; Mutunga, E. M.; Klein, K. L.; Damle, V.; Varanasi, K. K.; Rykaczewski, K. Different Shades of Oxide: From Nanoscale Wetting Mechanisms to Contact Printing of Gallium-Based Liquid Metals. *Langmuir* **2014**, *30*, 6867–6877.
- (238) Kramer, R. K.; Boley, J. W.; Stone, H. A.; Weaver, J. C.; Wood, R. J. Effect of Microtextured Surface Topography on the Wetting Behavior of Eutectic Gallium–Indium Alloys. *Langmuir* **2014**, *30*, 533–539.
- (239) Wissman, J.; Dickey, M. D.; Majidi, C. Field-Controlled Electrical Switch with Liquid Metal. *Adv. Sci.* **2017**, *4*, 1700169.
- (240) Martin, A.; Chang, B. S.; Pauls, A. M.; Du, C.; Thuo, M. Stabilization of Undercooled Metals via Passivating Oxide Layers. *Angew. Chemie* **2021**, *133*, 5993–6000.
- (241) Yang, Y.; Callahan, J. M.; Kim, T. H.; Brown, A. S.; Everitt, H. O. Ultraviolet Nanoplasmonics: A Demonstration of Surface-Enhanced Raman Spectroscopy, Fluorescence, and Photodegradation Using Gallium Nanoparticles. *Nano Lett.* **2013**, *13*, 2837–2841.
- (242) Ghigna, P.; Spinolo, G.; Parravicini, G. B.; Stella, A.; Migliori, A.; Kofman, R. Metallic versus Covalent Bonding: Ga Nanoparticles as a Case Study. *J. Am. Chem. Soc.* **2007**, *129*, 8026–8033.
- (243) Farrell, Z. J.; Tabor, C. Control of Gallium Oxide Growth on Liquid Metal Eutectic Gallium/Indium Nanoparticles via Thiolation. *Langmuir* **2018**, *34*, 234–240.
- (244) Morris, N. J.; Farrell, Z. J.; Tabor, C. E. Chemically Modifying the Mechanical Properties of Core-Shell Liquid Metal Nanoparticles. *Nanoscale* **2019**, *11*, 17308–17318.
- (245) Hohman, J. N.; Kim, M.; Wadsworth, G. A.; Bednar, H. R.; Jiang, J.; Lethai, M. A.; Weiss, P. S. Directing Substrate Morphology via Self-Assembly: Ligand-Mediated Scission of Gallium–Indium Microspheres to the Nanoscale. *Nano Lett.* **2011**, *11*, 5104–5110.

- (246) Tevis, I. D.; Newcomb, L. B.; Thuo, M. Synthesis of Liquid Core-Shell Particles and Solid Patchy Multicomponent Particles by Shearing Liquids into Complex Particles (SLICE). *Langmuir* **2014**, *30*, 14308–14313.
- (247) Han, J.; Tang, J.; Idrus-Saidi, S. A.; Christoe, M. J.; O'Mullane, A. P.; Kalantar-Zadeh, K. Exploring Electrochemical Extrusion of Wires from Liquid Metals. *ACS Appl. Mater. Interfaces* **2020**, *12*, 31010–31020.
- (248) Oliva-Puigdomènech, A.; De Roo, J.; Kuhs, J.; Detavernier, C.; Martins, J. C.; Hens, Z. Ligand Binding to Copper Nanocrystals: Amines and Carboxylic Acids and the Role of Surface Oxides. *Chem. Mater.* **2019**, *31*, 2058–2067.
- (249) Dabera, G. Di. M. R.; Walker, M.; Sanchez, A. M.; Pereira, H. J.; Beanland, R.; Hatton, R. A. Retarding Oxidation of Copper Nanoparticles without Electrical Isolation and the Size Dependence of Work Function. *Nat. Commun.* **2017**, *8*, 1894.
- (250) Pearson, R. G. Hard and Soft Acids and Bases. *J. Am. Chem. Soc.* **1963**, *85*, 3533–3539.
- (251) Heuer-Jungemann, A.; Feliu, N.; Bakaimi, I.; Hamaly, M.; Alkilany, A.; Chakraborty, I.; Masood, A.; Casula, M. F.; Kostopoulou, A.; Oh, E.; et al. The Role of Ligands in the Chemical Synthesis and Applications of Inorganic Nanoparticles. *Chem. Rev.* **2019**, *119*, 4819–4880.
- (252) Cademartiri, L.; Thuo, M. M.; Nijhuis, C. A.; Reus, W. F.; Tricard, S.; Barber, J. R.; Sodhi, R. N. S.; Brodersen, P.; Kim, C.; Chiechi, R. C.; et al. Electrical Resistance of Ag ... Tunnerling Junctions. *J. Phys. Chem. C* **2012**, *116*, 10848–10860.
- (253) Zhdanov, V. P.; Kasemo, B. Cabrera-Mott Kinetics of Oxidation of Nm-Sized Metal Particles. *Chem. Phys. Lett.* **2008**, *452*, 285–288.
- (254) Kirkendall, E. O. Diffusion Of Zinc in Alpha Brass. *Trans. AIME* **1942**, *171*, 104–110.
- (255) Zhdanov, V. P. Kinetic Model of Oxidation of Metal Nanoparticles: Cabrera-Mott and Kirkendall Effects. *Surf. Sci.* **2019**, *684*, 24–27.
- (256) Regan, M.; Tostmann, H.; Pershan, P.; Magnussen, O.; DiMasi, E.; Ocko, B. X-Ray Study of the Oxidation of Liquid-Gallium Surfaces. *Phys. Rev. B - Condens. Matter Mater. Phys.* **1997**, *55*, 10786–10790.
- (257) Pearson, R. G. Acids and Bases. *Science* **1966**, *151*, 172–177.
- (258) Schmidt, C.; Witt, A.; Witte, G. Tailoring the Cu(100) Work Function by Substituted Benzenethiolate Self-Assembled Monolayers. *J. Phys. Chem. A* **2011**, *115*, 7234–7241.
- (259) Otálvaro, D.; Veening, T.; Brocks, G. Self-Assembled Monolayer Induced Au(111) and Ag(111) Reconstructions: Work Functions and Interface Dipole Formation. *J. Phys. Chem. C* **2012**, *116*, 7826–7837.



- (260) Wu, K. Y.; Yu, S. Y.; Tao, Y. T. Continuous Modulation of Electrode Work Function with Mixed Self-Assembled Monolayers and Its Effect in Charge Injection. *Langmuir* **2009**, *25*, 6232–6238.
- (261) Rusu, P. C.; Brocks, G. Surface Dipoles and Work Functions of Alkylthiolates and Fluorinated Alkylthiolates on Au(111). *J. Phys. Chem. B* **2006**, *110*, 22628–22634.
- (262) Zhdanov, V. P.; Norton, P. R. Kinetics of Thin Oxide Film Growth on Metal Crystals. *Surf. Rev. Lett.* **2000**, *7*, 135–139.
- (263) Itoh, M.; Nishihara, H.; Aramaki, K. The Protection Ability of 11-Mercapto-1-undecanol Self-Assembled Monolayer Modified with Alkyltrichlorosilanes Against Corrosion of Copper. *J. Electrochem. Soc.* **1995**, *142*, 1839–1846.
- (264) Kanninen, P.; Johans, C.; Merta, J.; Kontturi, K. Influence of Ligand Structure on the Stability and Oxidation of Copper Nanoparticles. *J. Colloid Interface Sci.* **2008**, *318*, 88–95.
- (265) Inkpen, M. S.; Liu, Z. -F; Li, H.; Campos, L. M.; Neaton, J. B.; Venkataraman, L. Non-Chemisorbed Gold–Sulfur Binding Prevails in Self-Assembled Monolayers. *Nat. Chem.* **2019**, *11*, 351–358.
- (266) Zavabeti, A.; Ou, J. Z.; Carey, B. J.; Syed, N.; Orrell-Trigg, R.; Mayes, E. L. H.; Xu, C.; Kavehei, O.; O’Mullane, A. P.; Kaner, R. B.; et al. A Liquid Metal Reaction Environment for the Room-Temperature Synthesis of Atomically Thin Metal Oxides. *Science* **2017**, *358*, 332–335.
- (267) Коршунов, В. Поведение Вращающегося Дискowego Ga-Анода в Щелочной Среде. *Электрохимия* **1995**, *31*, 1122.
- (268) Lan, S.; Zhu, L.; Wu, Z.; Gu, L.; Zhang, Q.; Kong, H.; Liu, J.; Song, R.; Liu, S.; Sha, G.; et al. A Medium-Range Structure Motif Linking Amorphous and Crystalline States. *Nat. Mater.* **2021**, *20*, 1347–1352.
- (269) Elliott, S. R. Medium-Range Structural Order in Covalent Amorphous Solids. *Nature* **1991**, *354*, 445–452.
- (270) Regan, M. J.; Kawamoto, E. H.; Lee, S.; Pershan, P. S.; Maskil, N.; Deutsch, M.; Magnussen, O. M.; Ocko, B. M.; Berman, L. E. Surface Layering in Liquid Gallium: An x-Ray Reflectivity Study. *Phys. Rev. Lett.* **1995**, *75*, 2498–2501.
- (271) Yagafarov, O. F.; Katayama, Y.; Brazhkin, V. V.; Lyapin, A. G.; Saitoh, H. Energy Dispersive X-Ray Diffraction and Reverse Monte Carlo Structural Study of Liquid Gallium under Pressure. *Phys. Rev. B - Condens. Matter Mater. Phys.* **2012**, *86*, 1–9.
- (272) Dickey, M. D. Liquid Metals at Room Temperature. *Phys. Today* **2021**, *74*, 30–36.

- (273) Ren, X.; Lv, Q.; Liu, L.; Liu, B.; Wang, Y.; Liu, A.; Wu, G. Current Progress of Pt and Pt-Based Electrocatalysts Used for Fuel Cells. *Sustain. Energy Fuels* **2019**, *4*, 15–30.
- (274) Peng, Y.; Cui, M.; Zhang, Z.; Shu, S.; Shi, X.; Brosnahan, J. T.; Liu, C.; Zhang, Y.; Godbold, P.; Zhang, X.; et al. Bimetallic Composition-Promoted Electrocatalytic Hydrodechlorination Reaction on Silver-Palladium Alloy Nanoparticles. *ACS Catal.* **2019**, 10803–10811.
- (275) Wang, M.; Wang, L.; Li, H.; Du, W.; Khan, M. U.; Zhao, S.; Ma, C.; Li, Z.; Zeng, J. Ratio-Controlled Synthesis of CuNi Octahedra and Nanocubes with Enhanced Catalytic Activity. *J. Am. Chem. Soc.* **2015**, *137*, 14027–14030.
- (276) Wang, S. B.; Zhu, W.; Ke, J.; Lin, M.; Zhang, Y. W. Pd-Rh Nanocrystals with Tunable Morphologies and Compositions as Efficient Catalysts toward Suzuki Cross-Coupling Reactions. *ACS Catal.* **2014**, *4*, 2298–2306.
- (277) Cui, C.; Gan, L.; Li, H. H.; Yu, S. H.; Heggen, M.; Strasser, P. Octahedral PtNi Nanoparticle Catalysts: Exceptional Oxygen Reduction Activity by Tuning the Alloy Particle Surface Composition. *Nano Lett.* **2012**, *12*, 5885–5889.
- (278) Bu, L.; Shao, Q.; Pi, Y.; Yao, J.; Luo, M.; Lang, J.; Hwang, S.; Xin, H.; Huang, B.; Guo, J.; et al. Coupled S-p-d Exchange in Facet-Controlled Pd<sub>3</sub>Pb Tripods Enhances Oxygen Reduction Catalysis. *Chem* **2018**, *4*, 359–371.
- (279) Liu, Y.; Hight Walker, A. R. Monodisperse Gold-Copper Bimetallic Nanocubes: Facile One-Step Synthesis with Controllable Size and Composition. *Angew. Chemie - Int. Ed.* **2010**, *49*, 6781–6785.
- (280) Xie, Y.; Cai, J.; Wu, Y.; Zang, Y.; Zheng, X.; Ye, J.; Cui, P.; Niu, S.; Liu, Y.; Zhu, J.; et al. Boosting Water Dissociation Kinetics on Pt–Ni Nanowires by N-Induced Orbital Tuning. *Adv. Mater.* **2019**, *31*, 1–7.
- (281) Kim, D.; Resasco, J.; Yu, Y.; Asiri, A. M.; Yang, P. Synergistic Geometric and Electronic Effects for Electrochemical Reduction of Carbon Dioxide Using Gold-Copper Bimetallic Nanoparticles. *Nat. Commun.* **2014**, *5*, 1–8.
- (282) Goulas, K. A.; Sreekumar, S.; Song, Y.; Kharidehal, P.; Gunbas, G.; Dietrich, P. J.; Johnson, G. R.; Wang, Y. C.; Grippo, A. M.; Grabow, L. C.; et al. Synergistic Effects in Bimetallic Palladium-Copper Catalysts Improve Selectivity in Oxygenate Coupling Reactions. *J. Am. Chem. Soc.* **2016**, *138*, 6805–6812.
- (283) Wang, Y.; Cao, L.; Libretto, N. J.; Li, X.; Li, C.; Wan, Y.; He, C.; Lee, J.; Gregg, J.; Zong, H.; et al. Ensemble Effect in Bimetallic Electrocatalysts for CO<sub>2</sub> Reduction. *J. Am. Chem. Soc.* **2019**, *141*, 16635–16642.

- (284) Ye, H.; Crooks, R. M. Effect of Elemental Composition of PtPd Bimetallic Nanoparticles Containing an Average of 180 Atoms on the Kinetics of the Electrochemical Oxygen Reduction Reaction. *J. Am. Chem. Soc.* **2007**, *129*, 3627–3633.
- (285) Kim, D.; Nam, H.; Cho, Y. H.; Yeo, B. C.; Cho, S. H.; Ahn, J. P.; Lee, K. Y.; Lee, S. Y.; Han, S. S. Unlocking the Potential of Nanoparticles Composed of Immiscible Elements for Direct H<sub>2</sub>O<sub>2</sub> Synthesis. *ACS Catal.* **2019**, *9*, 8702–8711.
- (286) Xie, C.; Chen, C.; Yu, Y.; Su, J.; Li, Y.; Somorjai, G. A.; Yang, P. Tandem Catalysis for CO<sub>2</sub> Hydrogenation to C<sub>2</sub>-C<sub>4</sub> Hydrocarbons. *Nano Lett.* **2017**, *17*, 3798–3802.
- (287) Lin, M.; Kim, G. H.; Kim, J. H.; Oh, J. W.; Nam, J. M. Transformative Heterointerface Evolution and Plasmonic Tuning of Anisotropic Trimetallic Nanoparticles. *J. Am. Chem. Soc.* **2017**, *139*, 10180–10183.
- (288) Zhang, R. F.; Kong, X. F.; Wang, H. T.; Zhang, S. H.; Legut, D.; Sheng, S. H.; Srinivasan, S.; Rajan, K.; Germann, T. C. An Informatics Guided Classification of Miscible and Immiscible Binary Alloy Systems. *Sci. Rep.* **2017**, *7*, 1–12.
- (289) Asselin, J.; Boukouvala, C.; Wu, Y.; Hopper, E. R.; Collins, S. M.; Biggins, J. S.; Ringe, E. Decoration of Plasmonic Mg Nanoparticles by Partial Galvanic Replacement. *J. Chem. Phys.* **2019**, *151*, 244708.
- (290) Bahari, Z.; Dichi, E.; Legendre, B.; Dugué, J. The Equilibrium Phase Diagram of the Copper-Indium System: A New Investigation. *Thermochim. Acta* **2003**, *401*, 131–138.
- (291) Nakagawa, T.; Mitsushima, S.; Okuyama, H.; Nishijima, M.; Aruga, T. Evolution of Geometric and Electronic Structure in Ultrathin In Films on Cu(001). *Phys. Rev. B* **2002**, *66*, 1–18.
- (292) Kermali, N. A.; Gabe, D. R. Diffusion Coating of Indium on Copper. *Surf. Technol.* **1982**, *15*, 1–10.
- (293) Kim, D. gon; Lee, C. youl; Jung, S. B. Interfacial Reactions and Intermetallic Compound Growth between Indium and Copper. *J. Mater. Sci. Mater. Electron.* **2004**, *15*, 95–98.
- (294) Buonsanti, R.; Grillo, V.; Carlino, E.; Giannini, C.; Kipp, T.; Cingolani, R.; Cozzoli, P. D. Nonhydrolytic Synthesis of High-Quality Anisotropically Shaped Brookite TiO<sub>2</sub> Nanocrystals. *J. Am. Chem. Soc.* **2008**, *130*, 11223–11233.
- (295) Ranade, M. R.; Navrotsky, A.; Zhang, H. Z.; Banfield, J. F.; Elder, S. H.; Zaban, A.; Borse, P. H.; Kulkarni, S. K.; Doran, G. S.; Whitfield, H. J. Energetics of Nanocrystalline TiO<sub>2</sub>. *Proc. Natl. Acad. Sci. U. S. A.* **2002**, *99*, 6476–6481.
- (296) Li, X.; Chen, Q.; McCue, I.; Snyder, J.; Crozier, P.; Erlebacher, J.; Sieradzki, K. Dealloying of Noble-Metal Alloy Nanoparticles. *Nano Lett.* **2014**, *14*, 2569–2577.

- (297) Liu, P.; Chen, Q.; Ito, Y.; Han, J.; Chu, S.; Wang, X.; Reddy, K. M.; Song, S.; Hirata, A.; Chen, M. Dealloying Kinetics of AgAu Nanoparticles by in Situ Liquid-Cell Scanning Transmission Electron Microscopy. *Nano Lett.* **2020**, *20*, 1944–1951.
- (298) Cha, W.; Liu, Y.; You, H.; Stephenson, G. B.; Ulvestad, A. Dealloying in Individual Nanoparticles and Thin Film Grains: A Bragg Coherent Diffractive Imaging Study. *Adv. Funct. Mater.* **2017**, *27*, 1–8.
- (299) Mondal, S.; Raj, C. R. Electrochemical Dealloying-Assisted Surface-Engineered Pd-Based Bifunctional Electrocatalyst for Formic Acid Oxidation and Oxygen Reduction. *ACS Appl. Mater. Interfaces* **2019**, *11*, 14110–14119.
- (300) Oezaslan, M.; Heggen, M.; Strasser, P. Size-Dependent Morphology of Dealloyed Bimetallic Catalysts: Linking the Nano to the Macro Scale. *J. Am. Chem. Soc.* **2012**, *134*, 514–524.
- (301) Sun, Y.; Xia, Y. Alloying and Dealloying Processes Involved in the Preparation of Metal Nanoshells through a Galvanic Replacement Reaction. *Nano Lett.* **2003**, *3*, 1569–1572.
- (302) Karvianto; Chow, G. M. Size-Dependent Transformation from Ag Templates to Au-Ag Nanoshells via Galvanic Replacement Reaction in Organic Medium. *J. Nanoparticle Res.* **2012**, *14*, 1186.
- (303) Ma, H.; Gao, P.; Qian, P.; Su, Y. Size-Dependent Electrochemical Properties of Pure Metallic Nanoparticles. *J. Phys. Chem. C* **2020**, *124*, 3403–3409.
- (304) Shibata, T.; Bunker, B. A.; Zhang, Z.; Meisel, D.; Vardeman, C. F.; Gezelter, J. D. Size-Dependent Spontaneous Alloying of Au-Ag Nanoparticles. *J. Am. Chem. Soc.* **2002**, *124*, 11989–11996.
- (305) Cojocaru, B.; Avram, D.; Kessler, V.; Parvulescu, V.; Seisenbaeva, G.; Tiseanu, C. Nanoscale Insights into Doping Behavior, Particle Size and Surface Effects in Trivalent Metal Doped. *Sci. Rep.* **2017**, *7*, 4–12.
- (306) Müller, C. J.; Lidin, S. Cu<sub>11</sub>In<sub>9</sub> - Revised Crystal Structure and Its (Physicochemical) Relation to Cu<sub>10</sub>In<sub>7</sub>. *J. Alloys Compd.* **2015**, *638*, 393–397.
- (307) Cunningham, P. D.; Coropceanu, I.; Mulloy, K.; Cho, W.; Talapin, D. V. Quantized Reaction Pathways for Solution Synthesis of Colloidal ZnSe Nanostructures: A Connection between Clusters, Nanowires, and Two-Dimensional Nanoplatelets. *ACS Nano* **2020**, *14*, 3847–3857.
- (308) Liu, M.; Wang, R. Y. Size-Dependent Melting Behavior of Colloidal In, Sn, and Bi Nanocrystals. *Sci. Rep.* **2015**, *5*, 1–9.
- (309) Kind, C.; Feldmann, C.; Quintilla, A.; Ahlswede, E. Citrate-Capped Cu<sub>11</sub>In<sub>9</sub>

- Nanoparticles and Its Use for Thin-Film Manufacturing of Cis Solar Cells. *Chem. Mater.* **2011**, *23*, 5269–5274.
- (310) Lim, Y. S.; Jeong, J.; Kim, J. Y.; Ko, M. J.; Kim, H.; Kim, B.; Jeong, U.; Lee, D. K. Binder-Free Cu-in Alloy Nanoparticles Precursor and Their Phase Transformation to Chalcogenides for Solar Cell Applications. *J. Phys. Chem. C* **2013**, *117*, 11930–11940.
- (311) Varandili, S. B.; Huang, J.; Oveisi, E.; De Gregorio, G. L.; Mensi, M.; Strach, M.; Vavra, J.; Gadiyar, C.; Bhowmik, A.; Buonsanti, R. Synthesis of Cu/CeO<sub>2</sub>-x Nanocrystalline Heterodimers with Interfacial Active Sites to Promote CO<sub>2</sub> Electroreduction. *ACS Catal.* **2019**, *9*, 5035–5046.
- (312) Varandili, S. B.; Stoian, D.; Vavra, J.; Pankhurst, J.; Buonsanti, R. Ligand-Mediated Formation of Cu/Metal Oxide Hybrid Nanocrystals with Tunable Number of Interfaces. *Chem. Sci.* **2020**, *11*, 13094–13101.
- (313) Carvalho, H. W. P.; Pulcinelli, S. H.; Santilli, C. V.; Leroux, F.; Meneau, F.; Briois, V. XAS/WAXS Time-Resolved Phase Speciation of Chlorine LDH Thermal Transformation: Emerging Roles of Isovalent Metal Substitution. *Chem. Mater.* **2013**, *25*, 2855–2867.
- (314) Elding-Pontén, M.; Stenberg, L.; Lidin, S. The  $\eta$ -Phase Field of the Cu-In System. *J. Alloys Compd.* **1997**, *261*, 162–171.
- (315) Lidin, S.; Stenberg, L.; Elding-Pontén, M. The B8 Type Structure of Cu<sub>7</sub>In<sub>3</sub>. *J. Alloys Compd.* **1997**, *255*, 221–226.
- (316) Zhang, M.; Efremov, M. Y.; Schiettekatte, F.; Olson, E. A.; Kwan, A. T.; Lai, S. L.; Wisleder, T.; Greene, J. E.; Allen, L. H. Size-Dependent Melting Point Depression of Nanostructures: Nanocalorimetric Measurements. *Phys. Rev. B - Condens. Matter Mater. Phys.* **2000**, *62*, 10548–10557.
- (317) Couchman, P. R.; Jesser, W. Thermodynamic Theory of Size Dependence of Melting Temperatures in Metals. *Nature* **1977**, *269*, 481–483.
- (318) Zhang, J.; Zheng, Y.; Zhao, D.; Yang, S.; Yang, L.; Liu, Z.; Zhang, R.; Wang, S.; Zhang, D.; Chen, L. Ellipsometric Study on Size-Dependent Melting Point of Nanometer-Sized Indium Particles. *J. Phys. Chem. C* **2016**, *120*, 10686–10690.
- (319) Gao, F.; Gu, Z. Melting Temperature of Metallic Nanoparticles. In *Handbook of Nanoparticles*; Aliofkhazraei, M., Ed.; Springer, Cham, 2016; pp 661–690.

# Curriculum vitae

**Laia Castilla i Amorós**

**Date of birth:** 12/05/1995  
lcastillaiamoros@gmail.com

## EDUCATION

---

- Sept. 2018- **ÉCOLE POLYTECHNIQUE FÉDÉRALE DE LAUSANNE**, EPFL, Sion, Switzerland  
Aug. 2022 *Doctoral Assistant (PhD)*, Supervisor: *Professor Raffaella Buonsanti*
- UNIVERSITY OF BARCELONA**, FACULTY OF CHEMISTRY, Barcelona, Spain  
Sept. 2015- *Bachelor's Degree in Chemistry*, Supervisor: *Professor Eva Carolina Sañudo*  
July. 2018 **ERASMUS PROGRAM** at EPFL, Sion, Switzerland  
*Bachelor's Thesis*, Supervisor: *Professor Raffaella Buonsanti*
- Sept. 2013- **UNIVERSITY OF BARCELONA**, FACULTY OF PHARMACY, Barcelona, Spain  
July. 2015 120 ects. (4 semesters) accomplished of *Bachelor's Degree in Pharmacy*.

## LIST OF PUBLICATIONS

---

+ Indicate equal contribution

1. **Castilla-Amorós, L.**, Schouwink, P.+ , Oveisi, E.+ and Buonsanti, R., *Tailoring Morphology and Elemental Distribution of CuIn Nanoparticles via Galvanic Replacement*, **2022**, *under revision*.
2. **Castilla-Amorós, L.**, Chang Chien, T-C., Pankhurst, R. J. and Buonsanti, R., *Modulating the Reactivity of Liquid Ga Nanoparticle Inks by Modifying Their Surface Chemistry*, **2022**, *J. Am. Chem. Soc.*, 144, 4, 1993–2001.
3. **Castilla-Amorós, L.**, Stoian, D. C., Pankhurst, R. J., Varandili, S. B. and Buonsanti, R., *Exploring the Chemical Reactivity of Gallium Liquid Metal Nanoparticles in Galvanic Replacement*, **2020**, *J. Am. Chem. Soc.*, 142, 45, 19283–19290.

4. Pankhurst, J. R, **Castilla-Amorós, L.**, Stoian, D. C., Vavra, J., Mantella, V., Albertini, P. and Buonsanti, R., *Copper-Phosphonate Lamella Intermediates Control the Shape of Colloidal Copper Nanocrystals*, **2022**, *J. Am. Chem. Soc.*, 144, 27, 12261-12271.
5. Okatenko, V., **Castilla-Amorós, L.**, Stoian, D. C., Vavra, J., Loiudice, A. and Buonsanti, R., *The Native Oxide Skin of Liquid Metal Ga Nanoparticles Prevents Their Rapid Coalescence during Electrocatalysis*, **2022**, *J. Am. Chem. Soc.*, 144, 22, 10053-10063.
6. Mantella, V., **Castilla-Amorós, L.** and Buonsanti, R., *Shaping Non-Noble Metal Nanocrystals via Colloidal Chemistry*, **2020**, *Chem. Sci.*, 11, 11394-11403.
7. Gadiyar, C., Loiudice, A., D'Ambra, F., Oveisi, E., Stoian, D. C., Iyengar, P., **Castilla-Amorós, L.**, Mantella, V. and Buonsanti, R., *Nanocrystals as Precursors in Solid-State Reactions for Size- and Shape-Controlled Polyelemental Nanomaterials*, **2020**, *J. Am. Chem. Soc.*, 142, 37, 15931–15940.
8. Rosado Piquer, L., Dey, S., **Castilla-Amorós, L.**, Teat, S. J., Cirera, J., Rajaramaran, G. and Sañudo, E. C., *Microwave assisted synthesis of heterometallic 3d–4f M<sub>4</sub>Ln complexes*, **2019**, *Dalton Trans.*, 48, 12440

## CONFERENCE CONTRIBUTIONS

---

1. **ACS Spring 2022** (March 2022). Oral presentation: “Exploring the Chemistry of Liquid Metal Ga Nanoparticles”.
2. **ACS Fall 2021. Virtual Meeting** (August 2021). Oral presentation: “Exploring the Chemical Reactivity of Gallium Liquid Metal Nanoparticles in Galvanic Replacement”.
3. **MRS Spring 2021. Virtual Meeting** (April 2021). Oral presentation: “Galvanic Replacement Reactions on Liquid Metal Nanoparticles”.
4. **NanoGe Fall Meeting** (November 2019). Poster presentation: “Colloidal Synthesis of CuGa Nanodimers: Towards Multimetallic Catalysts for Electrochemical CO<sub>2</sub> Conversion”. Symposium Poster Prize.
5. **Winter School – Challenges and Opportunities in Energy Research** (March 2018). Attendee.